Spring 3-16-2021

Indolizine Donor-Based Dyes for Applications in Fluorescence Biological Imaging

William Meador

Indolizine Donor-Based Dyes for Applications in Fluorescence Biological Imaging

by
William E. Meador

A thesis submitted to the faculty of The University of Mississippi in partial fulfillment of the requirements of the Sally McDonnell Barksdale Honors College

Oxford
May 2021

Approved by:

_____
Advisor: Dr. Jared Delcamp

_____
Reader: Dr. Nathaniel Hammer

_____
Reader: Dr. Gerald Rowland

DEDICATION

To Rex and Jane

Thank you for teaching me the importance of enjoying life alongside the ones you love. I know you both would have been proud.

ACKNOWLEDGEMENTS

I would like to start off by thanking my mother and father, Deborah and Miles Meador. Your unconditional support has been a blessing throughout my life and without your encouragement I do not think I would have had the confidence to get to where I am today. To my sister, Audrey, it has been a pleasure to watch you blossom into a beautiful young woman. At times it was just me and you and your reverence of me has always inspired me to do better. I only hope that you can say the same of me.

Next, I would like to thank Lindsey. You have been a constant source of joy throughout this undergraduate journey and I really believe that this document would double in size if I tried to recount the memories we have shared together. From raising two beautiful kittens (what would an acknowledgment section be if I did not mention Queen Aurora and Princess Jasmine) to staying up late watching movies, I would not have wanted anyone else by my side on this journey. You have been such a good sport entertaining my chemistry rants, so there is really no use in you reading anything past this point since you probably know the content like the back of hand by now.

To my friends, Lucas, Morgan, Elisa, Ivy, Hunter, Madison, Jackie, and the gentlemen of Chi Psi (in no particular order), I would like to thank all of you for sharing your time with me throughout our collegiate journeys. In particular, I feel I need to personally thank Jackie and Hunter. Jackie, you helped to plant a seed that has flourished in unexpected ways. You introduced me to something that I look forward to doing every day, and we had one hell of a time setting up reactions and doing tai chi at Coulter hood 421. Hunter, you have been my best friend these past few years and I do not know what I am going to do without you here in Oxford. You have inspired me to grow professionally

as a chemist, and personally as a human being. I cannot thank you enough for the life lessons you have taught me and the good (and particularly wild) times we have shared.

I would also like to thank my fellow Delcamp group members as everyone on this team has positively impacted my undergraduate experience. From the original three undergraduate members of my freshman year to my “lab sister” Ivy, you guys have created an incredible research environment that has only deepened my love for chemistry. Whatever paths you find yourselves on in life, I know that you all will find success.

To all of my professors who have taken the time to make this department feel more like a home than a university, I thank all of you and hope that one day I can return the favor to the next generation of aspiring chemists. In particular, I would like to thank Prof. Hammer as a professor, advisor, and collaborator for reminding me that you can work hard and enjoy life at the same time. I would also like to thank the infamous Rowlands for the friendly faces they bring to the department each and every day, and the constant laughter they provide me with on my way to and from the NMR room.

I would like to thank the Sally McDonnell Barksdale Honors College for their efforts to craft citizen scholars across campus and their willingness to fund undergraduate research. In particular, I would like to thank Dr. Ibrahim from the Office of National Scholarship Advisement (ONSA). As the ONSA Director, Dr. Ibrahim is heavily involved in nearly every national scholarship that an Ole Miss student receives, and yet she receives none of the credit for it. In our few but impactful interactions, she has been critical, inspiring, and overwhelmingly friendly. I applaud her for her altruistic work behind the scenes, and personally thank her for helping me receive The Barry Goldwater Scholarship.

Lastly, I am eternally grateful for Dr. Delcamp and how he has shaped the trajectory of my life. Jared, you gave an eighteen-year-old kid who did not know a beaker from a pipette the chance to work in a cutting-edge synthetic research lab. I never envisioned myself going to graduate school, but now I cannot see myself doing anything else. Your synthetic knowledge and creativity are the reason I chose to remain here to pursue my doctoral studies as there is still so much I have to learn from you. When I envision myself having my own research group one day, I model the bulk of my vision off of your leadership. You exert more patience in a day than I feel as though I allot for an entire year, and your ability to advise students through complex synthetic problems is unparalleled. While I am immensely thankful for the past four years though, I am equally as excited for the next four and all that they have in store.

ABSTRACT

WILLIAM E. MEADOR: Indolizine Donor-Based Dyes for Applications in Fluorescence Biological Imaging

(Under the direction of Dr. Jared Delcamp)

NIR emissive fluorophores are intensely researched due to their potential to replace modern imaging procedures. Many molecular strategies have been employed in the literature to optimize fluorophores for deeper NIR absorption and emission, biocompatibility, and higher fluorescence quantum yields. Amongst the fluorophores studied to date, proaromatic indolizine donors are attractive alternatives to traditional alkyl amine and indoline based donors due to their 1) lower energy absorption and emission facilitated by proaromaticity, 2) large Stokes shifts due to increased dihedral angles about the π-system, 3) ease of functionalization and capacity for bioconjugation at the phenyl ring, and 4) potential for further red shifting via the placement of additional donors on the indolizine heterocycle. Herein, indolizine donors are incorporated into multiple common fluorophore moieties including squaraine-, cyanine-, and xanthene-based systems, and their photophysical properties studied. The indolizine donor allows for a diverse array of synthetic schemes, acting as both a nucleophile and CH activation coupling partner. Key results from indolizine donor-based fluorophores discussed herein include further red shifted cyanine absorbances compared to the ubiquitous benzindole cyanine, ICG, deep NIR-I absorption and NIR-II emission when incorporated into xanthene-based moieties, and low toxicity, high aqueous photostability, and record setting quantum yields in a biologically relevant medium.

TABLE OF CONTENTS

DEDICATION ii

ACKNOWLEDGEMENTS iii

ABSTRACT vi

LIST OF FIGURES viii

LIST OF SCHEMES x

CHAPTER I. INTRODUCTION 1

CHAPTER II. INDOLIZINE-CYANINE DYES: NEAR INFRARED EMISSIVE CYANINE DYES WITH INCREASED STOKES SHIFTS 4

CHAPTER III. DONOR-ACCEPTOR-DONOR NIR II EMISSIVE RHODINDOLIZINE DYE SYNTHESIZED BY C-H BOND FUNCTIONALIZATION 32

CHAPTER IV. WATER SOLUBLE NIR ABSORBING AND EMITTING INDOLIZINE CYANINE AND INDOLIZINE SQUARAINE DYES FOR BIOLOGICAL IMAGING 50

CHAPTER V. CONCLUSION 68

REFERENCES 70

APPENDIX 76

APPENDIX A. CHAPTER 2 SUPPLEMENTAL INFORMATION 77

APPENDIX B. CHAPTER 3 SUPPLEMENTAL INFORMATION 104

APPENDIX C. CHAPTER 4 SUPPLEMENTAL INFORMATION 115

APPENDIX D. JOURNAL PERMISSIONS 131

LIST OF FIGURES

Figure 1. Comparison of indoline cyanines to novel indolizine cyanines 7
Figure 2. Target indolizine cyanine dye structures 9
Figure 3. Synthesis of target indolizine cyanines 10
Figure 4. Crystal structures of indolizine cyanines 11
Figure 5. Molar absorptivities of indolizine cyanines 14
Figure 6. Absorption and emission of C1 16
Figure 7. Absorption and emission of C3 16
Figure 8. Absorption and emission of C5 17
Figure 9. HOMO and LUMO orbital diagrams of indolizine cyanines 21
Figure 10. Electron density differential maps of indolizine cyanines 23
Figure 11. Geometry illustration of indolizine cyanine electronic states 25
Figure 12. Rhodindolizine structure 35
Figure 13. Absorption and emission of rhodindolizine ethyl ester 42
Figure 14. Water soluble functionality of sulfonate indolizine dyes 53
Figure 15. Absorption and emission of sulfonate indolizine dyes 55
Figure 16. Photostability of sulfonate indolizine dyes in water 59
Figure 17. Cytotoxicity and Pearson's overlap coefficient of sulfonate dyes 61

LIST OF TABLES

Table 1. Indolizine cyanine crystal structure geometry measurements 11
Table 2. Indolizine cyanine photophysical data 17
Table 3. TD-DFT values for indolizine cyanines 21
Table 4. Computed geometries for indolizine cyanines 24
Table 5. Reaction optimization for xanthene ditriflate 37
Table 6. Reaction optimization for xanthene dibromide 39
Table 7. Reaction yields with substituted indolizines 40
Table 8. Photophysical data of sulfonate indolizine dyes 56

LIST OF SCHEMES

Scheme 1. Synthesis of rhodindolizine ethyl ester…….…..…….41

Scheme 2. Synthesis of sulfonate indolizine dyes…….....54

CHAPTER I.

INTRODUCTION

Small molecule emissive fluorophores have a wide array of applications including secure displays, telecommunications, and *in vivo* biological imaging. In particular, near infrared (NIR) fluorescence based biological imaging has been receiving a lot of attention recently as a powerful, practical tool with both medical and research-based applications. Fluorescence imaging involves the use of a small molecule fluorophore that absorbs and emits low energy photons to allow for the visualization of an *in vivo* biological environment. Fluorescence imaging presents an attractive option relative to other classic forms of biological imaging. As an example, magnetic resonance imaging (MRI) is a common technique used in medical practice that serves to aid in the diagnosis and monitoring of diseases by generating images of internal biological structures via the use of powerful magnetic fields. Although MRI instruments are highly effective, they are expensive, immobile, and require significant time delays in image generation. These limitations can be overcome through the use of suitable fluorescent materials as biological fluorescence imaging is relatively inexpensive due to its simple laser-based setup as opposed to the large cryogenically cooled magnets of MRIs. The use of a laser-based imaging system thus allows for facile mobility of the imaging setup due to decreased equipment demands and the potential for near instantaneous image response. Additionally, biological fluorescence imaging is non-invasive compared to endoscopy, and relatively non-toxic compared to radio-isotope mapping. Thus, fluorescence biological imaging is an attractive option to pursue as an option for widespread use in both research and professional medical settings.

There are a variety of options for NIR fluorophores including quantum dots, gold nanoparticles, upconverting phosphors, carbon nanotubes, and organic small molecules. Amongst these, organic small molecules are attractive due to their broad tunability, low toxicity, and precedent in imaging with the ubiquitous indocyanine green (ICG) having received FDA approval over 60 years ago. Organic fluorophores encompass a diverse array of molecular classes (defined primarily by the π-bridge connecting the donors) including cyanines, squaraines, BODIPYs, xanthenes, phthalocyanines, porphyrins, croconates, and bisthiadiazoles. However, many of these fluorophores to date still operate within the visible and NIR-I (700 – 1,000 nm) regions of the electromagnetic spectrum, and thus suffer from low tissue penetration and sub par imaging resolution due to the high scattering coefficient of biological tissues associated with these higher energy regions. For practical *in vivo* fluorescence imaging, fluorophores that operate in the short-wave infrared (SWIR, 1,000 – 2,500 nm) need to be accessed to avoid these inherent drawbacks of the higher energy visible and NIR-I regions. If these regions can be efficiently accessed, real time *in vivo* fluorescence biological imaging becomes a viable possibility. An attractive option to further extend into the SWIR region is too incorporate proaromatic (locally stabilized aromatic rings generated by electron donation into a π-system) donors, such as indolizine, into existing fluorophore designs. While alkyl amine, aryl amine, indole, quinoline, pyridinium, pyrylium, and thiopyrylium donors have all been extensively explored, little research has been done regarding the incorporation of indolizines donors into common fluorophore motifs. Indolizine is an attractive donor to pursue due to its facile synthesis, diverse tunability, and access to palladium catalyzed C-H activation coupling reactions for incorporation into previously inaccessible scaffolds.

For this reason, the development of indolizine donor-based deep red emissive fluorophores that maintain high molecular brightness is of focus herein.

CHAPTER II.

Indolizine-Cyanine Dyes: Near Infrared Emissive Cyanine Dyes with Increased Stokes Shifts

Adapted with permission from Jacqueline Gayton, Shane A. Autry, **William Meador**, Sean R. Parkin, Glake Alton Hill, Jr., Nathan I. Hammer, and Jared H. Delcamp.

J. Org. Chem. 2019, 84, 687. (Copyright (2019) ACS Online Library).

(See Appendix D. for permission license)

William Meador synthesized and characterized the methoxy- and cyano-indolizine donors and cyanine dyes, performed UV-Vis-NIR absorption spectroscopy, and aided in the solubility studies. Jacqueline Gayton synthesized and characterized the rest of the materials, performed UV-Vis-NIR absorption spectroscopy, grew the crystals of the cyanine dyes, and wrote the manuscript. Shane A. Autry performed fluorescence emission spectroscopy and calculated quantum yields of the cyanine dyes. Sean R. Parkin performed XRD crystallography on the dyes. Glake Alton Hill Jr. conducted the computational analyses of the dyes. All remaining PIs contributed experimental design and academic merit.

All Supplemental Information Items are provided in Appendix A.

ABSTRACT:

Molecular engineering strategies designed to red-shift cyanine dye absorptions and emissions further into the near-infrared (NIR) spectral region are explored. Through the use of a novel donor group, indolizine, with varying cyanine bridge lengths, dye absorptions and emissions, were shifted deeper into the NIR region than common indoline-cyanines. Stokes shifts resulting from intramolecular steric interactions of up to ~60 nm in many cases were observed and explained computationally. Molecular brightnesses of up to 5,800 deep into the NIR region were observed. Structure−property relationships are explored for the six indolizine cyanine dyes with varying cyanine bridge length and indolizine substituents showing broad absorption and emission tunability. The dyes are characterized by crystallography, and the photophysical properties are probed by varying solvent for absorption and emission studies. Computational data show involvement of the entire indolizine π-system during light absorption, which suggests these systems can be tunable even further into the NIR region through select derivatizations.

INTRODUCTION

Near infrared (NIR) emissive materials are a widely researched class of compounds with applications in an array of areas[1] including biological imaging, communications, and secure displays.[2-7] Dye designs based on cyanine structures are ubiquitous because of the intense molar absorptivity of these structures in the NIR region.[1] Additionally, the cyanine dye absorption wavelength is highly tunable based on methine chain length selection.[8] The tunability, rapid synthesis, facile bioconjugation, intense molar absorptivities (ε), strong NIR emissions, and high molecular brightness

(MB) values make this class of dyes attractive for further exploration as NIR emissive materials.[8-9] In addition to deeper NIR absorption and emission, dyes with large Stokes shifts and high quantum yields are in high demand.[9-12] For many applications, longer wavelength absorptions allow for access to differential dye properties relative to currently available dyes, and a larger Stokes shift provides dramatically higher resolution images in biological applications by reducing background signals.[5, 13-14] Importantly, a significant MB is needed to give high resolution images with smaller amounts of emissive material.[15] A balance between long wavelength use, Stokes shifts, and quantum yield must be struck for many functional materials in the NIR region, since the energy gap rule dictates diminished quantum yields as wavelengths increase.[16-19] Stokes shifts, which arise from molecular reorganizations, also tend to diminish quantum yields as the Stokes shift increases in magnitude. Introduction of molecular design elements which can increase Stokes shifts and the wavelength of both absorption and emission, while retaining a reasonable molecular brightness, can address a fundamental need in NIR emissive dye design.[20] Both the Stokes shift and lower energy absorption/emission challenges can be addressed by replacing the indoline donor of typical indoline cyanine dyes (such as FDA approved, commercially available, and widely used indocyanine green **ICG**) with a fully conjugated indolizine donor to delocalize the frontier molecular orbitals further (Figure 1). **ICG** serves as a good benchmarking cyanine dye since it is one of the most widely used cyanines over the past six decades with multiple reviews concerning the utility of this compound.[21-22] In the specific case of our study, the single nitrogen heteroatom donor groups of indoline-cyanines can be directly compared to the single nitrogen heteroatom donor groups of novel indolizine-cyanine dyes since the donor

heteroatom remains constant and a similar number of π-bonds are present in both donor groups. Additionally, the polycyclic indolizine donor provides a steric presence near the cyanine bridge, which requires either a deviation from planarity of the π-system or nonideal bond angles. Strain such as this in the ground state often affects excited state geometries differently, leading to increased reorganizations upon photoexcitation and thus enhanced Stokes shifts.[23-24]

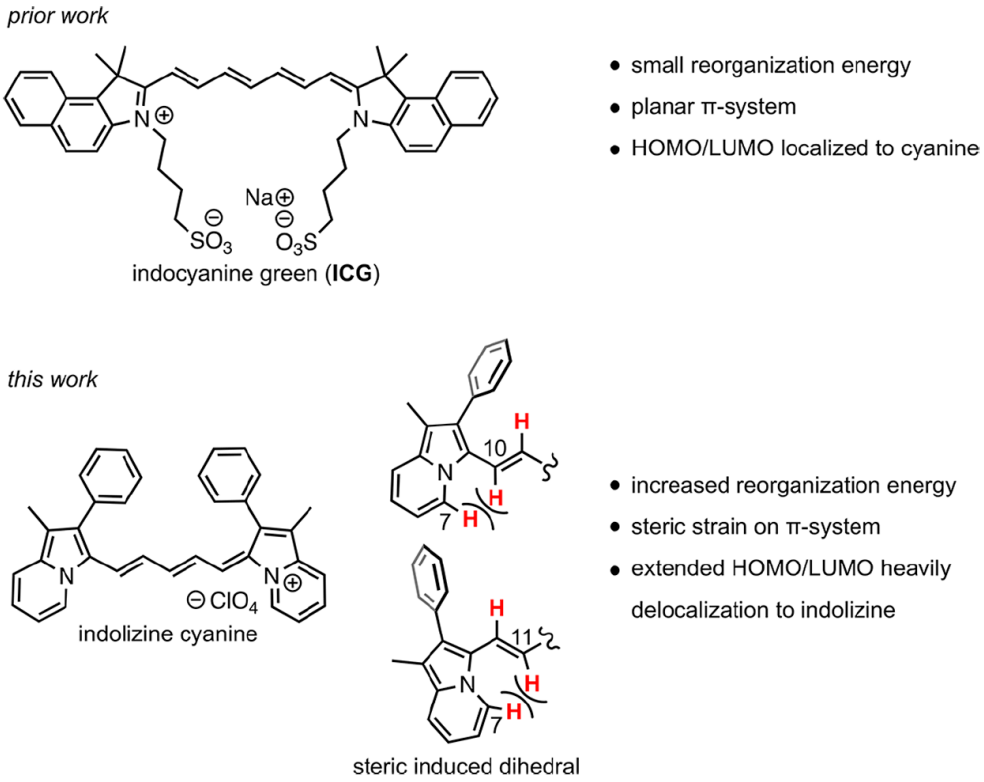

Figure 1. Comparison of an indoline cyanine dye and an indolizine cyanine dye. Hydrogens are drawn in for a portion of the indolizine cyanine on the right to show steric interactions. The indolizines are drawn in a cis conformation with a C7−C10 closest interaction as observed by crystallography for this specific compound. A second conformation exists for a C7−C11 close interaction which is also observed via crystallography in an example (see below).

Recently, our group published a series of squaraine dyes using an indolizine heterocycle as a donor in place of an indoline donor.[25] The indolizine donor allows for

red shifts farther into the NIR region due to the proaromatic nature of the indolizine, which generates an aromatic stabilized pyridinium ring after electron donation.[26] Additionally, an increased Stokes shift was observed, due in part to the planarization of aryl substituents on the indolizine ring in the excited state. This is significant, as indoline-squaraine dyes are known for very narrow energy gaps between the absorption and emission spectrum. Importantly, the molar absorptivities and quantum yields (and by default the MB, where MB = $\varepsilon \times \Phi$) remained high despite these changes. We reasoned that a similar strategy could be employed with cyanine bridges in place of the squaraine bridge. The cyanine-bridged dyes are attractive targets due to the simplistic tunability of the absorption wavelength by methine-bridge length selection. This type of straightforward absorption spectrum tuning is attractive, but is challenging to achieve with squaraine bridges. In this work, a series of dyes utilizing a constant indolizine donor structure with cyanine bridges between the donors of varying lengths with one, three, and five carbons (**C1**, **C3**, and **C5**) were prepared to probe the effects of methine bridge length on optical properties (Figure 2). Additionally, the electronic activity of positions on the indolizine donors are evaluated ranging from electron donating to electron withdrawing (**PhOMeIndz-C5**, **PhCNIndz-C5**, and **PhIndzOMe-C5**) in order to probe structure−property relationships on the dye optical properties.

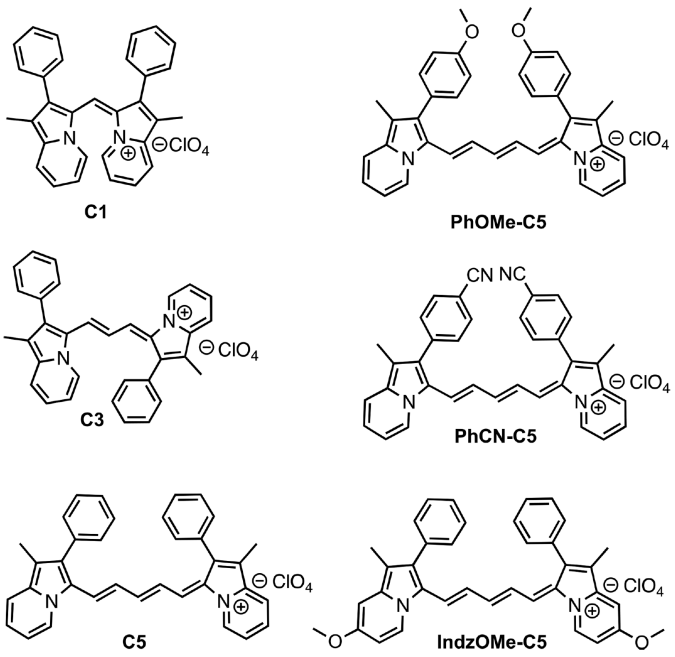

Figure 2. Target indolizine cyanine dyes.

RESULTS AND DISCUSSION

Target dyes **C1**, **C3**, and **C5** were synthesized from a known phenyl indolizine (**PhIndz**), which is available in two steps from commercially available 2-ethylpyridine (**1** when R′ = H) and 2-bromoacetophenone (**2** when R = H) via an *N*-alkylation reaction followed by a base catalyzed condensation reaction sequence (Figure 3).[23] **PhIndz** was then reacted with methine bridge precursors **4**, **5**, and **6** in the presence of perchloric acid to give **C1**, **C3**, and **C5**, respectively, in moderate to high yield (38−85%). **PhOMe-C5** and **PhCN-C5** follow the same synthetic route as **C5** beginning with known indolizine building blocks **PhOMeIndz** (**3** when R = OMe and R′ = H) and PhCNIndz (3 when R = CN and R′ = H), respectively. The synthesis of **IndzOMe-C5** began with the alkylation of commercially available 2-ethyl-4-methoxypyridine (**1** when R′ = OMe) with 2-bromoacetophenone, followed by cyclization to give **PhIndzOMe**. Reaction of

PhIndzOMe with iminium salt **6** afforded **IndzOMe-C5** in low isolated yield, presumably due to the low stability of the indolizine precursor in the reaction mixture, as the starting indolizine was consumed during the reaction. In general, the starting indolizines were handled with care due to limited stability, as they were found to decompose in solution under air and on silica gel; however, once the indolizine was incorporated into a cyanine dye the motif became stable to prolonged ambient exposure.

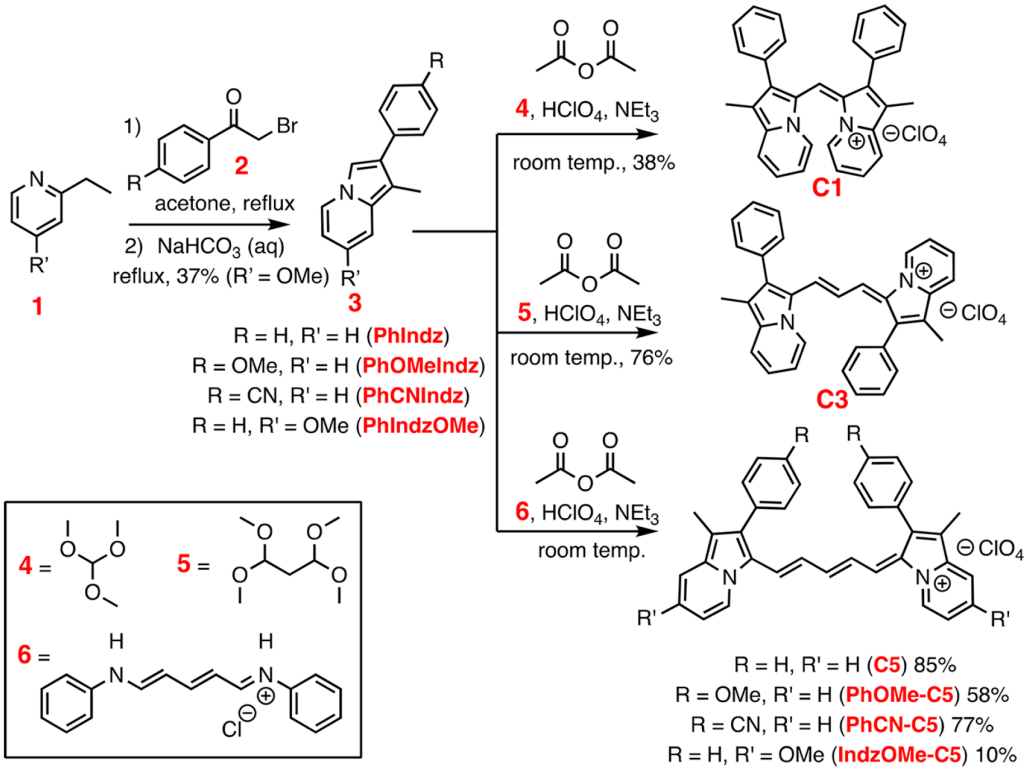

Figure 3. Synthetic route to the target indolizine cyanine dyes. The product conformations are drawn to match those obtained by crystal structure analysis of **C1**, **C3**, and **C5** (see below).

With the target dyes in hand, single-crystal X-ray diffraction studies were undertaken to probe the planarity of the dye π-system and to analyze the cyanine bridge bond lengths. We hypothesized the following: (1) **C1** potentially cannot adopt a

conformation with both indolizine heterocycles coplanar due to steric interactions between the indolizine groups with the short single carbon bridge, and (2) both **C3** and **C5** require some deviation from ideal bond angles or π-system planarity due to steric interactions between the indolizine and cyanine bridge. To probe these predictions, crystals suitable for crystallographic studies were grown by slow evaporation of MeCN from **C1**, or via vapor diffusion techniques in the cases of **C3** and **C5**. The crystals grew as thin needles or granules with a metallic like orange luster, as is common for very high molar absorptivity organic materials. The resolved structures are shown below (Figure 4) with select properties reported in Table 1.

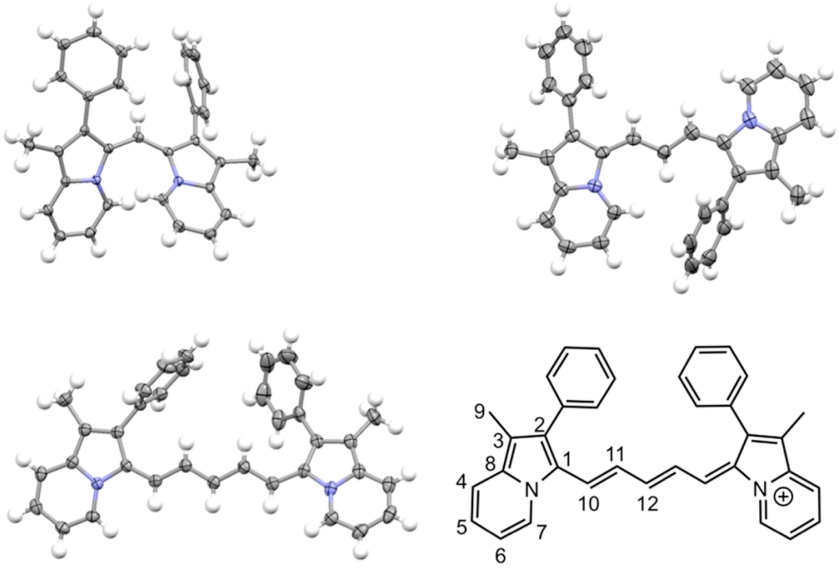

Figure 4. Crystal structures of **C1**, **C3**, and **C5** with cocrystallized solvents and counterions omitted. Hydrogens are included in order to emphasize potential steric interactions.

Table 1. Select Crystal Structure Geometry Measurements

dye	indz.-indz. dihedral (deg)	C1–C10 (Å)	C10–C11 (Å)	C11–C12 (Å)
C1	43	1.37 (1)	–	–
C3	175	1.38 (7)	1.39 (2)	–
C5	30	1.38 (3)	1.40 (2)	1.37 (5)

First, the planarity of each derivative was analyzed. As expected, the indolizine groups of **C1** are not coplanar and have π-systems perturbed by a 43° dihedral angle (Table 1). As a result, **C1** adopts a propeller type molecular shape, which significantly affects the molar absorptivity of this derivative (discussion below). **C3** and **C5** have lengthened methine chains that can allow for more coplanar conformations. The indolizine groups can adopt two different *cis* conformations or a *trans* type conformation with the phenyl groups either on the same side of the methine bridge or on opposite sides, respectively (see Table S4 for an illustration of the *cis* conformations). The *trans* conformer is the observed conformation of **C3** in the crystal structure, with a 175° dihedral angle (5° from coplanarity). Upon extending the methine chain to a five-carbon segment, the cis conformer was observed via crystallography, with a deviation of indolizine-indolizine π-faces from planarity by a 30° dihedral angle. The presence of both the *cis* and *trans* isomers of the indolizine cyanine dyes as crystals and the ^{1}H NMR appearing as a single set of peaks suggests that both isomers are accessible and interconversion between *cis* and *trans* isomers is likely possible as was observed for prior squaraine derivatives.[25] Bond length analysis reveals a reasonably uniform bond length (weak alternation) when the indolizine-cyanine bond is compared to the bonds of the cyanine bridge. This bond uniformity is indicative of cyanine type structures and extends from the attachment point of the cyanine bridge to the indolizine across the π-bridge with lengths varying by less than 0.03 Å for all derivatives. The observed bond lengths (1.37−1.40 Å) are between that of an average single C−C bond (1.54 Å) and a double C−C bond (1.34 Å, Table 1). This bond length uniformity suggests these systems are more likely to exhibit π−π* optical transitions than n−π* optical transition and that the

nonbonding electron lone pairs, which are often formally drawn on the nitrogens of the indolizine groups, are delocalized.

Absorption and emission studies were undertaken to analyze the optical properties of the dyes. First, the molar absorptivity and absorption curve features were analyzed for **C1**, **C3**, and **C5** to compare the effect of added methine spacers in several solvents (DCM, DMSO, 1:1 MeCN/H2O, and MeCN) differing in polarity and protic nature (Figure 5, Tables 2, S1 and S2). The absorption maxima were found to shift to longer wavelength with increasing number of methine groups (e.g., in DMSO λ_{max} values 652, 705, and 819 nm are observed for **C1**, **C3**, and **C5**, respectively). These maxima are likely from π–π* transitions based on bond length alternations observed from crystallography, DFT, and the high molar absorptivity values observed (see discussion below). This is a 23−26 nm red-shift for the **C5** derivative relative to the common indoline cyanine dye, **ICG**. Additionally, the molar absorptivity increased dramatically as the cyanine bridge length increased from 1 to 3 or more carbons. The twisted π-system of **C1** prevents a strong low-energy transition, limiting molar absorptivities from 11,000 to 27,000 M^{-1} cm^{-1} for **C1** depending on solvent selection. **C3** and **C5** molar absorptivities are in stark contrast to this at up to 204,000 and 188,000 M^{-1} cm^{-1}, respectively. These values are similar to **ICG**, which has a maximum measured molar absorptivity of 238,000 M^{-1} cm^{-1}. A characteristic cyanine high-energy shoulder is observed for each of the dyes, and this is attributed to vibronic transitions.[27] Both **C3** and **C5** exhibit similar molar absorptivity trends with solvents in the following order: DCM > DMSO > MeCN/ H2O > MeCN. These trends do not correlate to dielectric constants or dipole of solvent, which indicates a subtler solvent−dye interaction is occurring to vary molar absorptivities

(Table S1). **C1** follows a different molar absorptivity trend, and this deviation away from the pattern observed for **C3** and **C5** may originate from lack of planarity of the π-system of **C1**.

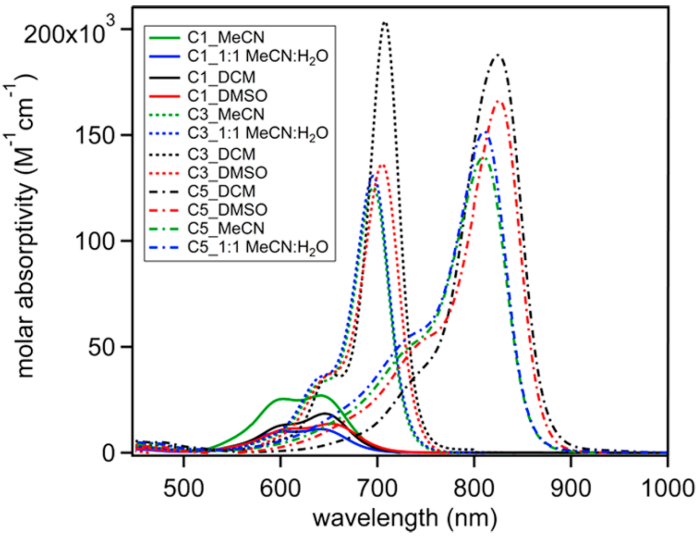

Figure 5. Molar absorptivities of **C1**, **C3**, and **C5** dyes in DCM, DMSO, MeCN, and 1:1 MeCN/H2O measured at 1×10^{-5} M concentrations. See Figure S1 for the full visible range. Individual plots of the absorption and emission of **C1**, **C3**, and **C5** dyes in the four solvents are in the SI (Figures S2−S4).

A host of additional solvents were analyzed for the **C1**, **C3**, and **C5** dyes to show solvent effects on absorption wavelength (see Figures 6−8). For each solvent analyzed via absorption spectroscopy, an emission spectrum in the same solvent was analyzed. For **C1**, the solvent had a significant effect on the absorption curve shape, with the shoulder at 600 nm changing intensity relative to the lower energy peak at 650 nm (Figure 6). THF shows the closest ratio of high-energy to lower-energy features nearing equal heights, while DCM shows the high energy feature at about a 75% of the height of the low-energy feature. All the dyes were found to have a linear absorbance versus concentration dependence following the Beer−Lambert Law from low concentrations ($<1 \times 10^{-6}$ M) to

high concentrations (>1 × 10^{-5} M), which suggests the solvent dependent features in the **C1** absorption spectrum are not due to aggregation. These results show that **C1** has significantly different ground-state solution conformations depending on solvent selection. The emission curve shape variation with solvent was even more dramatic. The emission maxima could be tuned over an ~200 nm range by solvent selection. THF and DMF represent the highest energy emission peaks near 650 nm, while DMSO, methanol, and ethanol all show peaks at wavelengths >800 nm, with DMSO being the most red-shifted at 850 nm. This is a 194 nm Stokes shift and represents a very large reorganization energy (0.43 eV) from the ground state to the excited state. All three of the solvents with the lowest energy emission spectrum peaks show dual emission behavior with an emission peak near 700 nm. This type of dichromic behavior has been observed previously with nonsymmetric cyanine dyes.[28] The low-energy emission is the dominant feature in MeOH, while the high-energy emission is dominant in DMSO. The remaining solvents all show a peak near 700 nm and typically show a shoulder at 750 nm, which mirrors the absorption spectrum, suggesting the higher energy absorption feature is vibronic in nature. The vast range of emission curve shapes and peak energies suggests a wide range of geometries are accessible in the excited state and the excited-state geometry is exceptionally solvent dependent. The quantum yield for **C1** was measured to be less than 1% in the same four solvents as the molar absorptivity studies (Table 2). This leads to a low molecular brightness upper limit of ≤300, as is expected from a molecule with a very large reorganization energy.

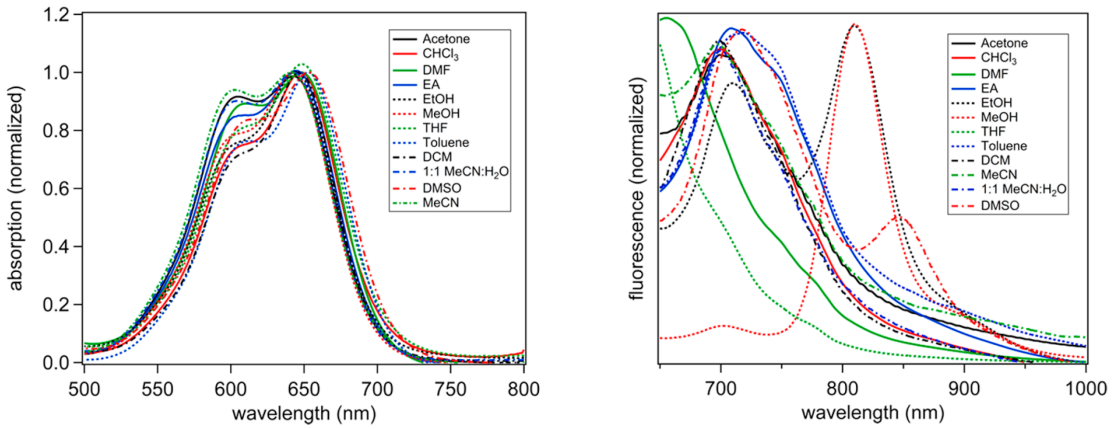

Figure 6. Absorption (left) and emission (right, fit with 0.1 LOESS function) spectra of **C1** in various solvents. Absorption spectra were collected at 1×10^{-5} M. Emission spectra were collected with excitation at 633 nm.

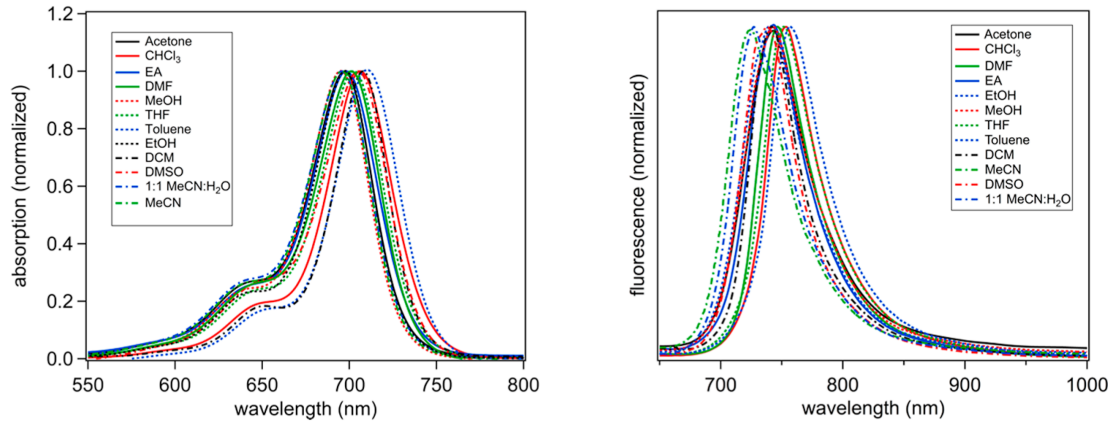

Figure 7. Absorption (left) and emission (right, fit with 0.1 LOESS function) spectra of **C3** in various solvents. Absorption spectra were collected at 1×10^{-5} M. Emission spectra were collected with excitation at 633 nm.

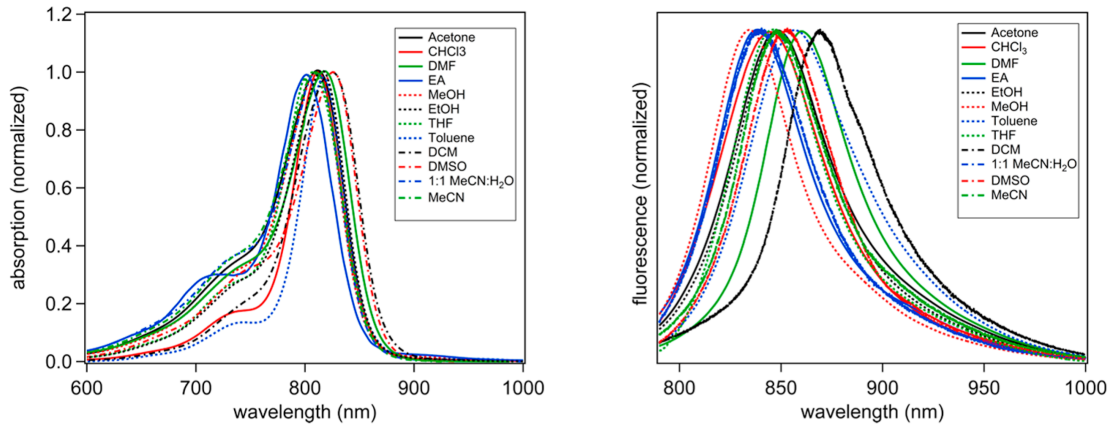

Figure 8. Absorption (left) and emission (right, fit with 0.1 LOESS function) spectra of **C5** in various solvents. Absorption spectra were collected at 1×10^{-5} M. Emission spectra were collected with excitation at 785 nm.

Table 2. Molar Absorptivity, Absorption Maximum, Emission Maximum, Quantum Yield, and Stokes Shift for Each Dye in Four Solvents[a]

dye	solvent	ε (M^{-1} cm^{-1})	λ_{max}^{abs} (nm)	λ_{max}^{emis} (nm)	Φ (%)	MB ($\varepsilon \times \Phi$)	Stokes shift (nm | eV | cm^{-1})
C1	MeCN	27 000	642	698	<1	≤300	56 | 0.15 | 1250
	1:1 MeCN/H_2O	11 000	641	698	<1	≤100	57 | 0.16 | 1270
	DMSO	14 000	652	846	<1	≤100	194 | 0.43 | 3517[b]
	DCM	18 000	646	693	<1	≤200	47 | 0.13 | 1050
C3	MeCN	126 000	695	725	<1	≤1300	30 | 0.07 | 595
	1:1 MeCN/H_2O	133 000	696	727	<1	≤1300	31 | 0.08 | 613
	DMSO	135 000	705	737	1.6	2200	32 | 0.08 | 616
	DCM	204 000	708	741	<1	≤2000	33 | 0.08 | 629
C5	MeCN	140 000	810	848	1.2	1700	38 | 0.07 | 553
	1:1 MeCN/H_2O	151 000	811	840	<1	≤1500	29 | 0.05 | 426
	DMSO	166 000	819	852	3.5	5800	33 | 0.06 | 473
	DCM	188 000	825	868	2.2	4100	43 | 0.07 | 600
PhOMe-C5	MeCN	94 000	799	845	1.3	1200	46 | 0.08 | 681
	1:1 MeCN/H_2O	146 000	799	831	<1	≤1500	32 | 0.06 | 482
	DMSO	162 000	816	840	2.7	4400	24 | 0.04 | 350
	DCM	207 000	813	863	1.9	3900	50 | 0.09 | 713
PhCN-C5	MeCN	122 000	799	854	<1	≤1200	55 | 0.10 | 806
	1:1 MeCN/H_2O	100 000	805	851	<1	≤1000	46 | 0.08 | 671
	DMSO	84 000	820	860	2.3	1900	40 | 0.07 | 567
	DCM	151 000	812	870	2.0	3000	58 | 0.10 | 821
IndzOMe-C5	MeCN	124 000	819	849	1.3	1600	30 | 0.05 | 431
	1:1 MeCN/H_2O	138 000	821	859	<1	≤1400	38 | 0.07 | 539
	DMSO	141 000	838	868	3.6	5100	30 | 0.05 | 412
	DCM	151 000	823	876	<1	<1500	53 | 0.09 | 735
ICG	1:1 MeCN/H_2O	238 000	785	816	9.1	21 700	31 | 0.06 | 484
	DMSO	211 000	797	835	17.1	36 100	38 | 0.07 | 571
$PhIn_2SQ$	DCM	181 000	716	766	2.1	3800	50 | 0.11 | 912
bis-t-buPhIn$_2$SQ	DCM	216 000	716	736	9.5	20 500	20 | 0.05 | 380
$TTD(T)_2$	Toluene	12 000	624	765	16.8	2000	141 | 0.37 | 2954
TPA-BBTD-TPA	Toluene	24 000	763	1065	7.1	1700	302 | 0.46 | 3716
CH1055-PEG	H_2O	–	750	1055	0.3	–	305 | 0.48 | 3855

[a]Absorption and emission curves for **PhOMe-C5**, **PhCN-C5**, and **PhIndzOMe-C5** are in the SI (Figures S5−S7). Data for **ICG** were collected under identical conditions as a benchmark. Data for $PhIn_2SQ$,[25] *bis-t*-buPhIn$_2$SQ,[25] $TTD(T)_2$,[24] TPA-BBTD-TPA,[29] and

CH1055-PEG[10] are from literature reports. ε is molar absorptivity. λ_{max}^{abs} is the absorption curve low energy peak value. λ_{max}^{emis} is the emission curve peak value. Φ is the quantum yield. MB is molecular brightness. [b]This value is based on the smaller lower energy emission peak. A higher energy emission peak (715 nm) is also observed which would correspond to a Stokes shift of 63 nm, 0.17 eV.

For the absorption curve profiles of **C3** and **C5**, solvent effects are not as dramatic as with **C1** (Figures 7 and 8). **C3** and **C5** show typical cyanine curve shapes with little energetic variation in the absorption curve maxima based on solvent choice (<20 nm change observed in the 12 solvents examined). The emission curves show a slight increase in solvent effect changes with a range of about 35 nm observed for **C3** and **C5**. Notably, the most red-shifted and most blue-shifted solvents change between these two derivatives, suggesting subtle differences in solvent interactions between these two dyes. Stokes shifts between 30 and 50 nm were observed for these dyes, which allows for use in some biological imaging applications.[30] Both **C3** and **C5** show >1% quantum yields with the highest values (1.6% and 3.5%, respectively) observed in DMSO. A high MB value of 5,800 is observed for **C5**. While the MB values for the indolizine-cyanine dyes were not as high as those reported for the **ICG** benchmark, it should be noted that these values can be improved dramatically through enhancing the emission quantum yield by selection of nonconjugated substituents, as was recently shown for CH1055-PEG.[15] Compared to other benchmark materials such as D−A−D dyes based on squaraine ($PhIn_2SQ$ and *bis*-*t*-$buPhIn_2SQ$) and thienothiadiazole ($TTD(T)_2$), **C5** is significantly more red-shifted by >100 nm in absorption and emission spectrum maxima. The reorganization energy of **C5** is similar to that of the squaraine derivatives, which have large Stokes shifts for that class of materials (0.07 eV versus 0.05−0.11 eV). Despite

being red-shifted significantly with a larger Stokes shift, the MB of **C5** is higher than these comparison dyes even with the very high quantum yield of $TTD(T)_2$. Compared to one of the most red-shifted imaging materials, TPA-BBTD-TPA (and derivative CH1055-PEG), a significantly higher MB is observed for **C5** with a more red-shifted absorption maximum. Notably, a significantly more red-shifted emission is present with TPA-BBTD-TPA. Overall, compared to the benchmark materials analyzed, **C5** is a promising dye scaffold for future applications.

The remaining indolizine-cyanine dyes synthesized are analogues of **C5** and show comparable absorption maxima, emission maxima, quantum yields, and MB to the parent compound in most solvents (Figures S4−S6). These derivatives (**PhOMe-C5**, **PhCN-C5**, and **IndzOMe-C5**) are dramatically different in substituent electronic nature with **PhOMe-C5** and **IndzOMe-C5** having a strong electron donating OMe group and **PhCN-C5** having a strong electron withdrawing group. The lack of change in the absorption and emission spectrum suggests these derivatives do not have a strong effect on the π-conjugated system (see computational discussion below). These positions on the indolizine heterocycle and phenyl group of the indolizine have little effect on the optical properties of these dyes and are attractive positions for functionalization to introduce components such as water solubilizing groups or bioconjugation functionality. The **C5** derivatives show up to a 41 nm red shift relative to **ICG** in DMSO, indicating a deeper NIR light absorption as is desired for many applications (Figures S8 and S9). This red shift occurs despite a two methine shorter bridge for the **C5** indolizine cyanine derivatives.

To better understand the role of the indolizine group and the optical properties of these dyes, calculations were performed using density functional theory (DFT) at the M06-2X/6-311G(d,p) level with the Gaussian 16 software package.[31-32] The SMD solvation model was used during geometry optimizations to better approximate the presence of MeCN.[33] Both the *cis* and *trans* isomers were analyzed since crystallography revealed the presence of cis isomers for **C1** and **C5** but the trans isomer of **C3**. A small energy difference was found between the ground state geometries of 1.0−4.4 kcal/mol with the *trans* isomer slightly lower in energy for **C1** and one of the *cis* isomers slightly lower in energy for **C3** and **C5** (see Supporting Information). For all derivatives studied the highest occupied molecular orbital (HOMO) and lowest unoccupied molecular orbital (LUMO) were delocalized across the entire π-system, with significant orbital presence on both the methine bridge and on the indolizine donors (Figures 9 and S16). It is noteworthy that the HOMO and LUMO are extended onto the conjugated indolizine heterocycle to a greater extent than is observed in the case of indoline cyanines.[34] This suggests the indolizine cyanine dyes may be electronically tuned more effectively than with indoline cyanines by careful substitution on the indolizine donor group.

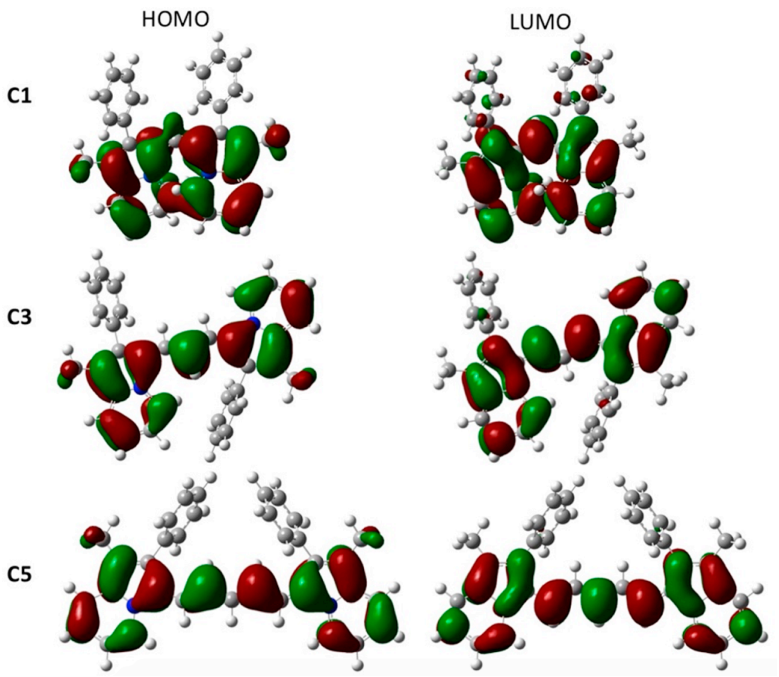

Figure 9. HOMO and LUMO images for **C1**, **C3**, and **C5** with an isovalue of 0.02.

Table 3. TD-DFT Values for the Ground- and Excited-State Optimized Geometries

dye	vertical trans. (eV, nm)	oscillator strength	dye* vertical trans. (eV, nm)	osc. str. dye*	Stokes shift (eV, nm)
C1 ***cis***[a]	2.20, 561	0.79	1.78, 697	0.47	0.42, 136
C3 ***trans***[a]	2.33, 533	1.11	2.18, 569	0.97	0.15, 36
C3 ***cis***[b]	1.91, 648	1.49	1.74, 712	1.27	0.17, 64
C5 ***cis***[b]	1.65, 752	2.06	1.51, 822	1.84	0.14, 70
C5 ***cis***[a,c]	2.08, 596	1.52	2.03, 611	1.75	0.05, 15

[a]Conformation observed by crystallography. [b]C7−C11 interaction in Figure 1. [c]C7−C10 interaction in Figure 1.

For comparison to experimental trends, time dependent (TD)-DFT calculations were carried out at the same level of theory as the geometry optimizations (Table 3). TD-DFT shows a similar trend to the observed experimental data for the *cis* isomer with a close C7−C11 interaction for both λ_{max} and ε when compared with the vertical transition energies and oscillator strengths in MeCN: **C1** < **C3** < **C5** (Table 3, Figure 1). When the different conformers obtained from the crystal structure analysis are compared

computationally, **C1** is redshifted relative to **C3**, and the energy of the vertical transition is significantly different than the experimental absorption spectrum maximum. As an example comparison, **C5** with the C7−C11 close interaction cis conformer shows theory and solution experiments within 0.12 eV. When the conformer observed via crystallography is computationally analyzed, the comparison with solution experimentation shows a larger variation of 0.55 eV. We note that the energy difference between these geometries is small at 2 kcal/mol, and since ^{1}H NMR shows only a single isomer, rapid interconversion is likely possible. These transitions were found to be HOMO to LUMO π–π* transitions. To analyze the experimental emission spectrum data computationally, the excited-state geometry for each derivative was optimized. Similar to experimental data, **C5** was found to have the most red-shifted excited-state geometry vertical transition (labeled dye* vertical trans. in Table 3) and strongest oscillator strength (brightest emission). **C1** was computationally shown to have the largest Stokes shift, which is in good agreement with experimental data. Electron density difference mapping of the three dyes was used to show where electrons are traveling from (red) and to (blue) upon photoexcitation (Figures 10 and S17). Green areas represent minimal electron movement. The maps show a delocalization of electron density across the cyanine π-bridge extending onto the full indolizine π-system in red, and a similar delocalization of areas accepting electron density on alternating atoms. No significant contribution from the phenyl group is observed on the electron density difference maps.

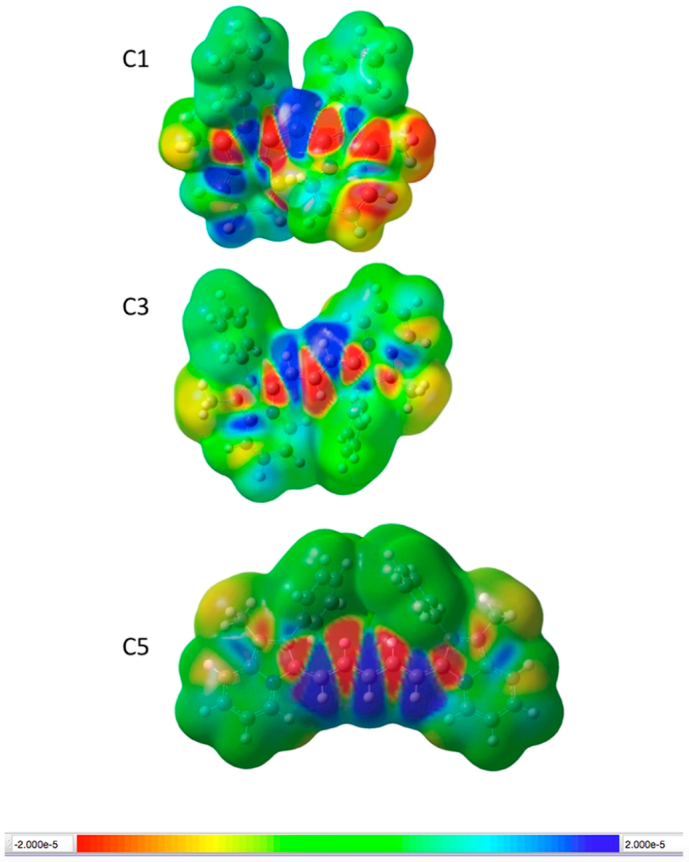

Figure 10. Electron density difference map. Red is where electrons originate from, blue is where they travel to upon photoexcitation, and green is neutral.

The predicted geometry changes from the ground state to the excited state were analyzed to determine the origin of the Stokes shift in these dyes. The ground state geometry shows a deviation of bond angles from ideal 120° sp^2 hybridized bond angles to wider values for all isomers (122°−134° for the first two angles measured, Tables 4 and S3). This deviation is presumably to lower steric interactions between hydrogen atoms on the indolizine and cyanine bridge (or between the two indolizines for the case of **C1**). Despite the bond angle distortion, the nearest hydrogens are still well within a typical hydrogen bond distance (1.5−2.5 Å). Upon photoexcitation, the bond angles adopt a closer to ideal geometry at 122°−130°. These angles favor increased steric interactions

between hydrogen atoms on indolizine and the cyanine bridge if the π-system were to remain planar. To relieve this increased strain, the indolizine−cyanine dihedral angle increases in the excited state by 4°−18° for all the conformers of **C3** and **C5** derivatives from nearer to planar in the ground state. This results in a less planar π-system, but does release steric strain, as evidenced by an increase in distance between nearest neighboring hydrogens of about 0.1 Å (Table S4). Thus, the ground state geometry favors bond angle distortion with a more ideal dihedral angle across the π-system, while the excited state geometry favors a distorted dihedral angle across the π-system but gains more ideal bond angles (Figure 11). This change in geometry explains the increased Stokes shift for these indolizine cyanine derivatives relative to well-established indoline cyanines.

Table 4. Select Computed Bond Angles, Dihedral Angles, and Atom−Atom Distances[a]

dye	angle 1 (deg) GS | ES	angle 2 (deg) GS | ES	angle 3 (deg) GS | ES	angle 4 (deg) GS | ES	dihedral (deg) indz-cyanine GS | ES	dihedral (deg) indz−indz GS | ES	H−H bond distance (Å) GS | ES
C1	128 | 123	134 | 125	N/A	N/A	15 | 27	35 | 50	2.7 | 3.6[b]
C3	128, 123 | 127, 122	131, 126 | 129, 123	120 | 123	N/A	2, 10 | 11, 22	15 | 32	1.8, 2.1 | 1.9, 2.1
C5	122 | 122	127 | 126	122 | 124	123 | 121	7 | 11	22 | 33	2.1 | 2.0

[a]GS is ground state. ES is excited state. [b]Indicates H−H bond distance is between the two closest hydrogens of the indolizines. The structure below illustrates the bond angles being analyzed.

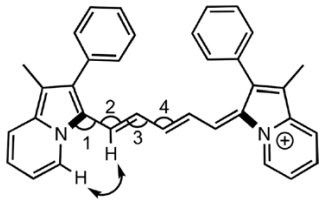

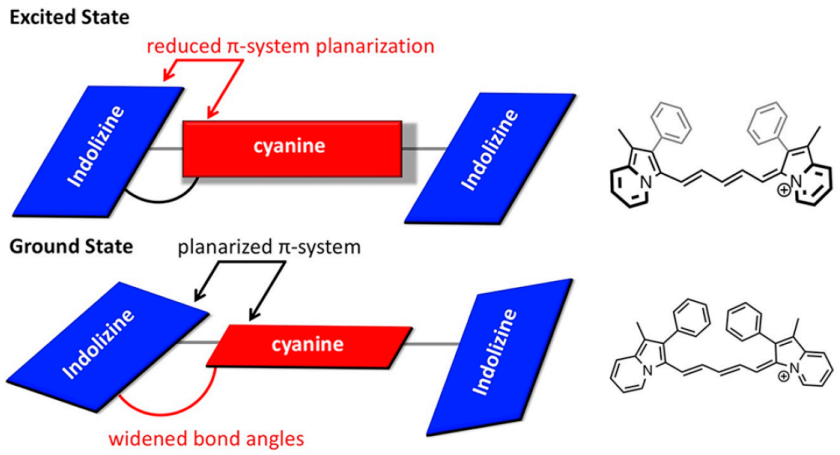

Figure 11. Illustration of geometry changes from the ground state to the excited state.

CONCLUSION

Six NIR indolizine-cyanine dyes were designed, synthesized, and characterized. UV−vis−NIR absorption measurements show that increasing the methine bridge lengths leads to redshifted absorptions. The indolizine-cyanine dyes show a redshifted absorption relative to benchmark **ICG** despite two fewer methines. This shows the critical role the indolizine groups can play in shifting absorption spectra as a conjugated donor group. The dyes were found to emit in the NIR region with the sterically congested dye **C1** showing the largest solvent effects and reorganization energies. The five methine group bridge of **C5** was found to lead to the largest quantum yields and a high MB value for a dye emitting near 900 nm. Computational studies reveal that the ground state favors a planarized π-system with distorted bond angles while the excited state favors the opposite geometry. Importantly, the use of molecularly engineered steric interactions shows that significant Stokes shifts can be designed into a class of molecules known for minimal Stokes shifts while keeping a good quantum yield and red shifting the absorption and emission curves.

EXPERIMENTAL SECTION

General Information. All commercially obtained reagents and solvents were used as received without further purification. *Caution*: It should be noted that the dyes were isolated as perchlorate salts, and perchlorate salts in general have been found to be explosive in some cases. Care is advised while handling all perchlorate salts. Thin-layer chromatography (TLC) was conducted with Sorbtech silica XHL TLC glass backed plates and visualized with UV. Flash column chromatography was performed using a CombiFlash Rf+ system. RediSep cartridges were charged with silica gel from Sorbent Tech P60, 40−63 μm (230−400 mesh). ^{1}H and ^{13}C NMR spectra were recorded on a Bruker Avance-300 (300 MHz) spectrometer and a Bruker Avance-500 (500 MHz) spectrometer and are reported in ppm using solvent as an internal standard (DMSO at 2.50 ppm). Data are reported as s = singlet, d = doublet, t = triplet, q = quartet, p = pentet, m = multiplet, b = broad, ap = apparent, dd = doublet of doublets; coupling constant(s) are in Hz; integration. UV−vis-NIR spectra were measured with a Cary 5000 UV−vis−NIR spectrometer. HRMS spectra were obtained with a QTOF HRMS utilizing nanospray ionization. The mass analyzer was set to the 200−2000 Da range. Infrared spectra were recorded with an Agilent Cary 660 ATR-FTIR. For all derivatives, the excited-state lifetimes were found to be shorter than the response function of the instrument. The emission of the **C1** and **C3** derivatives were measured using a Horiba LabRam spectrometer with a 600 grooves/mm grating, CCD camera detection, and an excitation laser of 633 nm. All other dyes were measured using the same instrument and a 785 nm excitation laser. The quantum efficiency of the detector was accounted for when

measuring emission profiles. The relative quantum yields were obtained using this equation:

$$\Phi_{\text{Sample}} = \Phi_{\text{Standard}} \cdot \frac{E_{\text{Sample}}}{E_{\text{Standard}}} \cdot \frac{A_{\text{Standard}}}{A_{\text{Sample}}} \cdot \frac{\eta^2_{\text{Sample}}}{\eta^2_{\text{Standard}}}$$

For the equation above, E is the sum of emission intensities and A is maximum absorbance. η is the refractive index of the solvent used, and Φ denotes the quantum yield.[35] The standard used to obtain the relative quantum yields was Indocyanine Green (ICG) with a quantum yield of 14% in H_2O.[36] Diffraction data were collected at 90 K on a Bruker D8 Venture dual microsource diffractometer using Mo Kα X-rays. Data scaling, merging, and absorption correction used well-established procedures.[37-38] Crystal structures were solved and refined using the Shelx programs.[39-40] Crystals of **C3** included some poorly defined solvent that was accounted for using SQUEEZE.[41]

(Z)-1-Methyl-3-((1-methyl-2-phenylindolizin-3-yl)methylene)-2-phenyl-3H-indolizin-4-ium Perchlorate (**C1**). To a round-bottom flask equipped with a stir bar, **PhIndz** (1.00 g, 4.80 mmol) was added to acetic anhydride (48 mL) followed by perchloric acid (0.48 g, 4.80 mmol). The mixture was allowed to stir at room temperature for 5 min. Triethylorthoformate (**4**) (0.36 g, 2.40 mmol) was added along with triethylamine (0.58 g, 5.76 mmol). The reaction mixture was allowed to stir at room temperature for 24 h before being subjected to a silica gel column with a solvent gradient beginning with 40:60 dichloromethane/hexane and ending with 100% dichloromethane. The product was isolated as a red solid (0.48 g, 38%). ^{1}H NMR (300 MHz, DMSO-d6) δ 8.50 (s, 2H), 8.08−7.97 (m, 4H), 7.90−7.80 (m, 4H), 7.44−7.37 (m, 8H), 7.3 (t, J = 6.8 Hz, 1H), 2.38 (s, 6H). ^{13}C NMR was not obtained due to low solubility. IR (neat, cm^{-1}):

3598, 3534, 2916, 2665, 2329, 2092, 1777, 1621, 1586, 1464. HRMS *m/z* calculated for $C_{31}H_{25}N_2$ $[M - ClO4]^+$: 425.2018, found 425.2019. Melting point: 157−162 °C.

(Z)-1-Methyl-3-((E)-3-(1-methyl-2-phenylindolizin-3-yl)- allylidene)-2-phenyl-3H-indolizin-4-ium Perchlorate (**C3**). To a round-bottom flask equipped with a stir bar, **PhIndz** (0.35 g, 1.69 mmol) was added to acetic anhydride (17.0 mL) followed by perchloric acid (0.169 g, 1.69 mmol). The mixture was allowed to stir at room temperature for 5 min. Malonaldehyde bis(dimethyl acetal) (**5**) (0.139 g, 0.845 mmol) was added along with triethylamine (0.205 g, 2.03 mmol). The reaction mixture was allowed to stir at room temperature for 24 h before being subjected to a silica gel column with a solvent gradient beginning with a 50:50 dichloromethane/ hexane solvent mixture and ending with 100% dichloromethane. The product was isolated as a gold solid (0.35 g, 76%). ^{1}H NMR (300 MHz, DMSO-d6) δ 7.99 (d, J = 8.5 Hz, 2H), 7.76−7.68 (m, 9H), 7.46−7.31 (m, 9H), 6.69 (t, J = 13.2 Hz, 1H), 2.19 (s, 6H). ^{13}C NMR was not obtained due to sparing solubility. IR (neat, cm^{-1}): 3109, 2993, 2817, 2669, 2582, 2330, 2116, 1618, 1555, 1533, 1454. HRMS *m/z* calculated for $C_{33}H_{27}N_2$ $[M + H]^+$: 451.2174, found 451.2197. Melting point (dec.): 252−253 °C.

(Z)-1-Methyl-3-((2E,4E)-5-(1-methyl-2-phenylindolizin-3-yl)- penta-2,4-dien-1-ylidene)-2-phenyl-3H-indolizin-4-ium Perchlorate (**C5**). To a round-bottom flask equipped with a stir bar, **PhIndz** (1.00 g, 4.80 mmol) was added to acetic anhydride (48.0 mL) followed by perchloric acid (0.48 g, 4.80 mmol). The mixture was allowed to stir at room temperature for 5 min. (Phenylamino)pentadienylidene aniline HCl (**6**) (0.68 g, 2.40 mmol) was added along with triethylamine (0.58 g, 5.76 mmol). The reaction mixture was allowed to stir at room temperature for 24 h before being subjected to a

silica gel column with a solvent gradient beginning at 50:50 dichloromethane/hexane and ending with 100% dichloromethane. The product was isolated as a gold solid (1.1 g, 82%). ^{1}H NMR (300 MHz, DMSO-d6) δ 9.18 (d, J = 6.9 Hz, 2H), 8.03 (d, J = 13.6 Hz, 2H), 7.91 (d, J = 8.6 Hz, 2H), 7.70−7.54 (m, 8H), 7.37−7.25 (m, 8H), 5.91 (t, J = 12.5 Hz, 1H), 2.14 (s, 6H). ^{13}C NMR was not obtained due to sparing solubility. IR (neat, cm^{-1}): 3652, 2670, 2564, 2329, 2116, 1925, 1806, 1671, 1617, 1516, 1458. HRMS *m/z* calculated for $C_{35}H_{29}N_2$ $[M]^+$: 477.2331, found 477.2315. Melting point (dec.): 176−179 °C.

(Z)-2-(4-Methoxyphenyl)-3-((2E,4E)-5-(2-(4-methoxyphenyl)-1- methylindolizin-3-yl)penta-2,4-dien-1-ylidene)-1-methyl-3H-indolizin- 4-ium Perchlorate (**PhOMe-C5**). To a round-bottom flask equipped with a stir bar, **PhOMeIndz** (1.08 g, 4.54 mmol) was added to acetic anhydride (45.0 mL) followed by perchloric acid (0.46 g, 4.54 mmol). The mixture was allowed to stir at room temperature for 5 min. (Phenylamino)pentadienylidene aniline HCl (**6**) (0.65 g, 2.27 mmol) was added along with triethylamine (0.55 g, 5.45 mmol). The reaction mixture was allowed to stir at room temperature for 24 h before being poured into ether (200 mL). The pure product was insoluble in ether and was isolated by vacuum filtration as a red solid (0.81 g, 58%). ^{1}H NMR (300 MHz, DMSOd6) δ 9.16 (d, J = 6.9 Hz, 2H), 7.90−7.85 (m, 2H), 7.70 (t, J = 15.6 Hz, 2H), 7.45−7.29 (m, 8H), 7.13 (d, J = 8.3 Hz, 6H), 6.42 (t, J = 11.5 Hz, 1H), 3.91 (s, 6H), 2.14 (s, 6H). ^{13}C NMR was not obtained due to sparing solubility. IR (neat, cm^{-1}): 3656, 3581, 3333, 2831, 2656, 2463, 2329, 2116, 1919, 1804, 1754, 1706, 1658, 1607, 1555, 1516, 1465. HRMS *m/z* calculated for $C_{37}H_{33}N_2O_2$ $[M]^+$: 537.2542, found 537.2516. Melting point (dec.): 158−161 °C.

(Z)-2-(4-Cyanophenyl)-3-((2E,4E)-5-(2-(4-cyanophenyl)-1- methylindolizin-3-yl)penta-2,4-dien-1-ylidene)-1-methyl-3H-indolizin- 4-ium Perchlorate (**PhCN-C5**). To a round-bottom flask equipped with a stir bar, **PhCNIndz** (1.00 g, 4.31 mmol) was added to acetic anhydride (45.0 mL) followed by perchloric acid (0.432 g, 4.31 mmol). The mixture was allowed to stir at room temperature for 5 min. (Phenylamino)pentadienylidene aniline HCl (**6**) (0.613 g, 2.15 mmol) was added along with triethylamine (0.523 g, 5.17 mmol). The reaction mixture was allowed to stir at room temperature for 24 h before being poured into ether (200 mL). The pure product was insoluble in ether and was isolated by vacuum filtration as a red solid (1.0 g, 77%). ^{1}H NMR (300 MHz, DMSO-d6) δ 9.19 (d, J = 6.8 Hz, 2H), 8.05 (d, J = 8.1 Hz, 4H), 7.98 (d, J = 8.6 Hz, 2H), 7.91 (d, J = 14.0 Hz, 2H), 7.76 (t, J = 7.6 Hz, 2H), 7.65 (d, J = 8.1 Hz, 4H), 7.44−7.36 (m, 4H), 6.21 (t, J = 13.2 Hz, 1H), 2.18 (s, 6H). ^{13}C NMR was not obtained due to sparing solubility. IR (neat, cm^{-1}): 3611, 3395, 2354, 2332, 2116, 1619, 1612, 1530, 1527, 1471. HRMS *m/z* calculated for $C_{37}H_{27}N_4$ $[M]^+$: 527.2236, found 527.2251. Melting point (dec.): 187−191 °C.

(Z)-1-Methyl-3-((E)-3-(1-methyl-2-phenylindolizin-3-yl)- allylidene)-2-phenyl-3H-indolizin-4-ium Perchlorate (**IndzOMe- C5**): Part 1: 7-Methoxy-1-methyl-2-phenylindolizine (**4**, **PhIndzOMe**). To a round-bottom flask equipped with a stir bar and a reflux condenser were added 2-ethyl-4-methoxypyridine (0.39 g, 2.81 mmol) and bromoacetophenone (0.84 g, 4.22 mmol) in acetone (5.62 mL). The mixture was heated to reflux in an oil bath for 24 h. The reaction was monitored by TLC. Upon disappearance of the starting material **2**, water (5.62 mL) and sodium bicarbonate (0.94 g, 11.2 mmol) were added to the reaction mixture. The mixture was heated at reflux in an

oil bath for 2 h. The crude product oiled out of solution and was extracted with dichloromethane to yield a brown oil that was immediately subjected to a rapid plug filtration through silica gel with 20:80 ethyl acetate/hexanes to yield an off-white solid. Due to oxidative instability, the intermediate was carried forward to the next reaction without any further purification or characterization. To a round-bottom flask equipped with a stir bar under nitrogen, the intermediate **PhIndzOMe** (0.25 g, 1.05 mmol) was added to acetic anhydride (10.5 mL) followed by perchloric acid (0.11 g, 1.05 mmol). The mixture was allowed to stir at room temperature for 5 min. (Phenylamino)pentadienylidene aniline HCl (**6**) (0.15 g, 0.52 mmol) was added along with triethylamine (0.13 g, 1.26 mmol). The reaction mixture was allowed to stir at room temperature for 3 h before being subjected to a plug of silica with a solvent gradient from 100% dichloromethane to 50:50 ethyl acetate/dichloromethane. A final purification was performed by dissolving the concentrated product in a minimal amount of dichloromethane followed by the addition of diethyl ether/hexanes (50:50) to yield the pure product as a green solid (0.03 g, 10%). ^{1}H NMR (300 MHz, DMSO-d6) δ 9.02 (d, J = 7.5 Hz, 2H), 7.73−7.53 (m, 10H), 7.33 (d, J = 7.2 Hz, 4H), 7.15− 7.01 (m, 4H), 5.86 (t, J = 14.4 Hz, 1H), 4.01 (s, 6H), 2.10 (s, 6H). ^{13}C NMR was not obtained due to sparing solubility. IR (neat, cm^{-1}): 3788, 3691, 2917, 2633, 2329, 2116, 1797, 1775, 1630, 1527, 1444. HRMS *m/z* calculated for $C_{37}H_{33}N_2O_2$ $[M]^+$: 537.2542, found 537.2532. Melting point (dec.): 162−165 °C.

CHAPTER III.

Donor−Acceptor−Donor NIR II Emissive Rhodindolizine Dye Synthesized by C−H Bond Functionalization

Adapted with permission from Chathuranga S. L. Rathnamalala, Jacqueline N. Gayton, Austin L. Dorris, Shane A. Autry, **William Meador**, Nathan I. Hammer, Jared H. Delcamp, and Colleen N. Scott.

J. Org. Chem. 2019, 84, 13186 (Copyright (2019) ACS Online Library).

(See Appendix D. for permission license)

William Meador synthesized all of the indolizine donors, Chathuranga Rathnamalala synthesized and characterized the rest of the materials and wrote the manuscript, Jacqueline Gayton performed initial synthesis and characterization of the materials, Austin Dorris and Shane A. Autry performed absorption and fluorescence spectroscopic measurements and calculated quantum yields. All other PIs contributed experimental design and intellectual merit.

All Supplemental Information Items are provided in Appendix B.

ABSTRACT

A NIR II emissive dye was synthesized by the C−H bond functionalization of 1-methyl-2-phenylindolizine with 3,6- dibromoxanthene. The rhodindolizine (RhIndz)

spirolactone product was nonfluorescent; however, upon opening of the lactone ring by the formation of the ethyl ester derivative, the fluorophore absorbs at 920 nm and emits at 1092 nm, which are both in the NIR II region. In addition, 4-cyanophenyl- (CNRhIndz) and 4- methoxyphenyl-substituted rhodindolizine (MeORhIndz) could also be prepared by the C−H activation reaction.

INTRODUCTION

Photoluminescent materials in the near-infrared I (NIR I) (~0.7−0.9 μm) and near-infrared II (NIR II) (~0.9−1.7 μm) region of the electromagnetic spectrum have applications in many areas such as optical recording, laser filters, thermal writing displays, bioimaging, NIR photography, photodynamic therapy, and solar cells.[2-4, 42-49] Among these applications, NIR I and NIR II materials are desirable for tissue imaging due to the deeper penetration of light, minimal tissue damage, and high spatial resolution as a result of low autofluorescence in the NIR I and NIR II regions.[5, 10, 13, 50-52] There are several examples of NIR I dyes derived from common fluorescent dye scaffolds such as cyanine,[1, 30, 53-56] phthalocyanine and porphyrin,[47, 57-58] squaraine,[25, 59-61] BODIPY analogs,[62-64] benzo [c]heterocycle,[65] and xanthene derivatives.[47, 66-69] Among these common scaffolds, xanthene-based dyes are widely explored due to their outstanding photophysical properties and stimuli responses. Consequently, they have been modified to achieve absorption and emission wavelengths in the NIR I region. For example, replacing the bridged oxygen atom of the xanthene scaffold to phosphorus[70] or silicon[71] leads to a reduced optical energy gap into the NIR I region. Subsequently, there are a number of examples from our group,[72] and others[73-74] that have demonstrated strong atom

substitution effects with various xanthene-based dyes. In addition, Yuan and co-workers have developed several NIR I dyes with moderate to high quantum yields by extending the π-conjugation of the xanthene scaffold.[75-76] In contrast, while there are several examples of NIR I emissive dyes, there are only a few NIR II fluorophores available.[5, 10, 13, 15, 26, 51, 77-79] 2 Nanoparticles and quantum dots have shown interesting photophysical properties as NIR II fluorophores with very high quantum efficiencies;[80-81] however, these nanoparticles tend to be insoluble, slow to excrete from the body, and accumulate in the spleen and liver, making them nonideal therapeutic agents in many cases.[82-83] In this regard, small molecule organic dyes are attractive for clinical applications because of their tendency to metabolize in the cells and low toxicity.[10, 53-54] Recently, researchers have sought different strategies to develop NIR II organic emissive dyes such as combining donor and acceptor groups.[24, 29, 84-85] This approach is well-developed for organic electronic devices, and this strategy has been successful in producing low bandgap molecules. The choice of a good donor−acceptor pair can significantly lower the optical bandgap of a dye due to the promotion of charge transfer events.[48, 86] Indolizines are gaining use in dye-sensitized solar cells as the donor due to a good donor strength compared to ubiquitous triphenylamine donors and other alkyl amine-based donor groups.[23, 26, 87-88] The excellent donor strength of indolizines is a result of several factors, such as having a nitrogen atom with three separate single bonds creating a fully planar geometry, a fully conjugated π-scaffold with the nitrogen lone pair, low stabilization energy, and a pro-aromatic nature.[23, 26, 89] Owing to the excellent photophysical properties of xanthene-based dyes and their electron accepting ability, we have designed a donor−acceptor−donor NIR II fluorescent dye by coupling the 3-position of the electron

rich indolizine to the 3 and 6 positions of the electron poor xanthene using the C−H bond functionalization reaction (Figure 12).

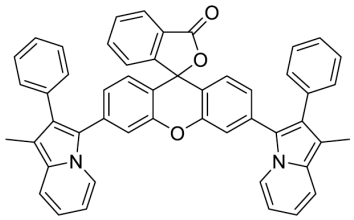

Figure 12. Rhodindolizine structure.

C−H bond functionalization/activation has emerged as a very useful method for the formation of sp^2-hybridized C−C bonds. C−H activation synthetic routes have an advantage over the classical cross-coupling approaches in that additional synthetic steps to activate the carbon site and the production of toxic byproducts are avoided.[90-92] C−H functionalization can be highly tolerant of many functional groups, which makes it desirable for the preparation of drugs and natural products. However, since there are usually many C−H bonds on the substrates, selectivity can be challenging. While C−H functionalization on sp^2-hybridized carbon centers has been widely developed for the preparation of conjugated compounds for applications in organic devices, only a few examples have been reported for the synthesis of photoluminescent dyes.[85] For instance, Verbelen et al. have developed several BODIPY dyes by radical C−H arylation and alkylation.[93-94] They have also reported the direct palladium catalyzed C−H activation at the 3- and 3,5-positions of a BODIPY derivative that resulted in high fluorescence quantum yields ($\Phi > 0.85$).[94] Perumal and co-workers have reported tetra-substituted olefinic xanthene dyes with aggregation induced emission (AIE) properties, which were synthesized by a tandem Pd catalyzed 6-exo-dig cyclization followed by a C−H activation reaction.[95] Gryko and co-workers have prepared indolizine based dyes by a

double C−H activation of electron deficient indolizines with the electron rich dibromoarenes, fluorene and thiophene.[96] They obtained the desired bis-indolizine products in 58% and 47% yield, respectively.

Herein, we reported the first NIR II xanthene-based dye, which was prepared by the C−H bond functionalization reaction of 1-methyl-2-phenylindolizine with 3′,6′-dibromofluoran (a xanthene derivative). The specific methyl/phenyl substitution pattern on the indolizine was selected as these groups allow for a simple synthesis of an electron rich indolizine with prolonged ambient stability. The target dye is inspired by the popular rhodamine dyes; however, the xanthene core is attached to carbon atoms of indolizine (Figure 12), instead of nitrogen atoms, which is common to the rhodamine structure. Interestingly, 3′,6′-bis(1-methyl-2-phenylindolizin- 3-yl)-3H-spiro[2-benzofuran-1,9′-xanthen]-3-one (Figure 12), which is referred to as rhodindolizine (**RhIndz**) from here on, undergoes the typical molecular optical switching between the closed spirocyclic ring structure and the open-form that is commonly observed for rhodamine dyes. **RhIndz** shows intense absorption and emission in the NIR II region of the spectrum, which is desirable for biological imaging. To analyze the substituent effects on the C−H activation reaction, substituted indolizines containing both electron withdrawing and electron donating groups on the phenyl ring were investigated.

RESULTS AND DISCUSSION

The C−H bond functionalization is an attractive method for preparing 3-substituted indolizine since preparing/isolating 3-haloindolizines, which are common precursors to other classical cross coupling reagents, such as organoboron and organotin

reagents, is challenging. Furthermore, the direct borylation at the 3-position of the indolizine is also challenging, while the C−H bond functionalization at the 3- position of indolizine has been reported.[96-97] The synthesis of **RhIndz** begins with the known 3,6-ditriflated fluorescein (**1**) reported by Lavis and co-workers.[98] The intermolecular C−H bond functionalization of 1-methyl-2-phenylindolizine with the 3,6-ditriflated xanthene derivative was explored by varying the catalyst, ligand, base, additive, solvent, temperature and time according to Table 5 and Table S1.

Table 5. Optimization of Reaction Conditions for Xanthene Ditriflate[a]

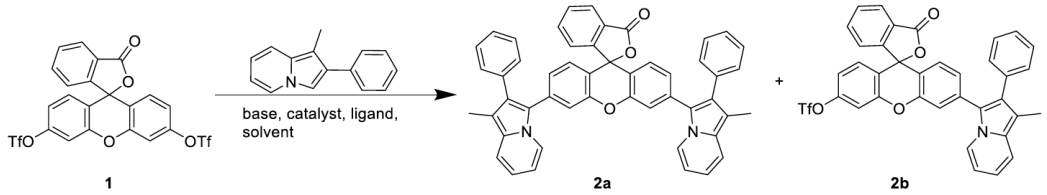

1 2a 2b

entry	catalyst	ligand	KOAc (equiv)	temp (°C)	time (h)	(%)[b] **2a**:**2b**
1	$PdCl_2(PPh_3)_2$	none	(5.2)	80	6.5	5:10
2	$PdCl_2(PPh_3)_2$	none	(5.2)	80	18	8:17
3	$Pd(OAc)_2$	PPh_3	(3.0)	150	20	14:0
4	$Pd(OAc)_2$	XPhos	(6.0)	100	20	22:20
5[c]	$Pd(OAc)_2$	XPhos	(6.0)	100	20	5:6

[a]Reactions are carried out in a sealed tube under nitrogen atmosphere in the presence of **1** (0.083 mmol), 1-methyl-2-phenylindolizine (0.167 mmol), NMP (entries 1 and 2) or DMF as solvent (0.34−2.0 mL), catalyst (10 mol %), ligand (20 mol % when added), and KOAc. [b]Isolated yields (%) were reported for **2a** and **2b**. [c]Pivalic acid added (30 mol %).

We began our study with $PdCl_2(PPh_3)_2$ (10 mol %) as the catalyst, potassium acetate (KOAc) (5.2 equiv) as the base, and N-methyl-2-pyrrolidone (NMP) as the solvent at 80 °C for 6.5 h (Table 5, Entry 1). For these conditions, 5% of the desired disubstituted product (2a, **RhIndz**) and 10% of undesired monosubstituted product (2b) were isolated. Increasing the time to 18 h only slightly increased the yield of the desired

product (Table 5, Entry 2). Notably, changing the base to cesium carbonate (Cs_2CO_3), potassium *tert*-butoxide (KO^tBu), or sodium *tert*-butoxide (NaO^tBu) yielded trace or no product (Supporting Information Table S1, Entries 1−3). In fact, the ditriflated xanthene precursor was converted to fluorescein by a detriflation process that was previously observed by Rogers et al.,[99] with the recovery of the indolizine starting material. When the catalyst was changed to $Pd(OAc)_2$ (10 mol %) with triphenylphosphine (PPh_3) (20 mol %) as the ligand, KOAc (3 equiv) as the base in DMF at 150 °C for 20 h, only the desired product was obtained in 14% isolated yield (Table 5, Entry 3). The yield of the desired product increased to 22% when XPhos (20 mol %) was used as the ligand in place of PPh_3 at 100 °C (Table 5, Entry 4). The work of Fagnou and co-workers has shown the direct arylation of electron rich indolizines with trialkylphosphines;[97] however, with $(^tBu)_2PMeHBF_4$ added as the ligand, no product was obtained (Supporting Information Table S1, Entry 4). In fact, the addition of pivalic acid (30 mol %) or any condition that requires strong bases such as K_2CO_3, Cs_2CO_3, and KO^tBu, including the conditions reported by Ozawa and co-workers that use $Pd(dba)_3{\cdot}CHCl_3$ adduct (10 mol %) as the catalyst,[100] resulted in only trace or no product at all (Supporting Information, Table S1, Entries 5−10). In all cases, mostly unreacted starting materials were recovered.

While the target dye is accessible from the xanthene ditriflate precursor with yields high enough for photophysical studies, the C−H bond functionalization of 1-methyl-2-phenylindolizine with 3′,6′-dibromofluoran[101] was investigated to determine if the reaction yield could be improved (Table 6). 3′,6′-dibromofluoran (3) and 1-methyl-2-phenylindolizine were subjected to $PdCl_2(PPh_3)_2$ (10 mol %) as the catalyst, KOAc (5.2 equiv) as the base, and NMP as the solvent at 80 °C for 18 h. From these reaction

conditions, the desired product was isolated in 23% yield (Table 6, Entry 1). Changing the base to Cs_2CO_3 did not affect the yield (Table 6, Entry 2), and there was no observable conversion with NaO^{t}Bu (Table S2, Entry 1). However, by increasing the reaction temperature and time to 110 °C and 24 h respectively, the desired product could be isolated in 35% yield (Table 6, Entry 3). Further increase in the temperature to 150 °C did not improve the yield (Table 6, Entry 4). Again, Fagnou's conditions or the use of XPhos only lowered the percent conversion after 18 h (Table S2, Entries 2 and 3). To the best of our knowledge, this is the first known case of a xanthene-based C(sp^2)−C(sp^2) bond C−H activation cross-coupling reaction, and this route sets a precedent for the rapid access of aryl-xanthene derivatives. Furthermore, our yields were comparable to the literature where bis-indolizine products were prepared by C− H bond functionalization.[96]

Table 6. Optimization of Reaction Conditions with 3′,6′-Dibromofluoran (3)[a]

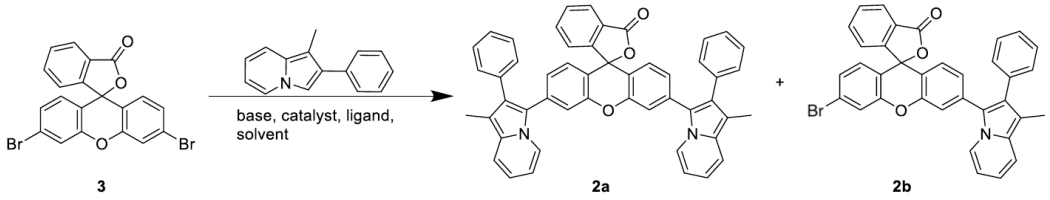

3 2a 2b

entry	catalyst	base (equiv)	temp (°C)	time (h)	yield (%)[b]
1	$PdCl_2(PPh_3)_2$	KOAc (5.2)	80	18	23
2	$PdCl_2(PPh_3)_2$	Cs_2CO_3 (5.2)	80	18	23
3	$PdCl_2(PPh_3)_2$	KOAc (5.2)	110	24	35
4	$PdCl_2(PPh_3)_2$	KOAc (5.2)	150	24	35

[a]Unless otherwise specified, the reaction was carried out in a sealed tube under nitrogen atmosphere in the presence of **3** (0.11 mmol), 1-methyl-2-phenylindolizine (0.24 mmol), NMP solvent (0.34−2 mL), $PdCl_2(PPh_3)_2$ (10 mol %), and base, for 18−24 h at 80−150 °C. [b]Isolated yields (%) reported for **2a**.

In order to probe the substrate scope with respect to the C− H bond functionalization of the indolizine coupling partner, the electronic effects on the reaction were investigated. As such, the C−H bond functionalization of six phenyl-substituted 1-

methyl-2-phenylindolizine containing electron donating and withdrawing groups were investigated in comparison with the parent 1-methyl-2-phenylindolizine using the optimized conditions from Table 7. 4-Cyanophenyl-substituted rhodindolizine (**CNRhIndz**) was obtained in comparative yield relative to **RhIndz** (30% versus 35% respectively) indicating that the resonance withdrawing CN group is tolerated in this reaction. However, 4-trifluoromethylphenyl-substituted (**CF_3RhIndz**), 4-nitrophenyl-substituted rhodindolizine (**NO_2RhIndz**) and 3,5-ditrifluoromethylphenyl-substituted (**diCF_3RhIndz**), led to low or trace amounts of the corresponding products. The origin of the low yields is not obvious, but it is notable that the starting materials, compound 3 and indolizine precursors were not consumed during the reaction. Modifying the phenyl group with the electron donating phenol substituent led to only trace product, presumably due to the reaction not tolerating acidic functionality (Table 7, Entry 5.) On the other hand, the methoxy derivative gave a reasonable yield (20%) of the desired product (Table 7, Entry 6).

Table 7. Substrate Scope with Substituted Indolizines

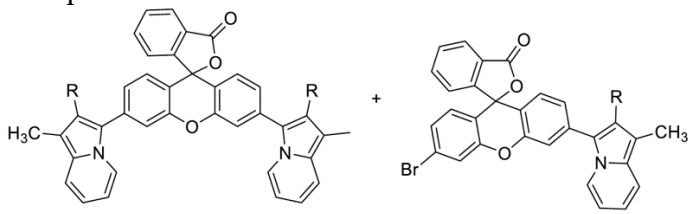

di-substituted Prod **mono-substituted Prod**

compound	R group	yield (%) di:mono
CNRhIndz 4	4-CNPh	30:14
CF_3RhIndz 5	4-CF_3Ph	11:6
NO_2RhIndz 6	4-NO_2Ph	trace
diCF_3RhIndz 7	3,5-bisCF_3Ph	trace
HORhIndz 8	4-OHPh	trace
MeORhIndz 9	4-OMePh	20:0

With **RhIndz** in hand, the reactivity of the spirolactone functionality was explored. Interestingly, upon exposure to strong Bronsted acids the lactone ring resisted ring opening. However, the ring-opened acid chloride derivative could be prepared directly from the lactone using $POCl_3$ in refluxing 1,2-dichloroethane (Scheme 1),[102] which was reacted with anhydrous ethanol to form the ethyl ester (**10**). Having accessed both the ring closed (**2a**) and ring open (**10**) forms, the photophysical properties of these derivatives were investigated.

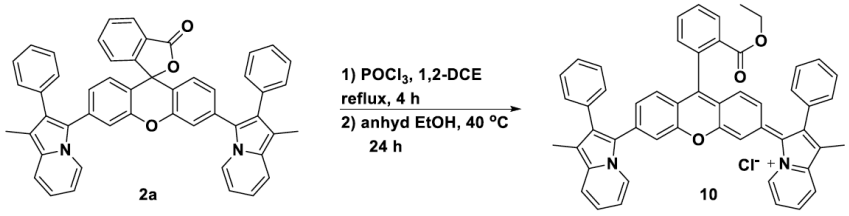

Scheme 1. Synthesis of **RhIndz** Ethyl Ester 10 from **RhIndz 2a**

The absorption maximum for **RhIndz** is 375 nm (Figure S1). However, upon the formation of the ethyl ester, a large bathochromic shift of 550 nm occurs shifting the maximum absorption to 920 nm, which is within the NIR II region. The dye also displays a high molar absorptivity of 97,500 $M^{-1}cm^{-1}$, which is critical for a practical molecular brightness (MB). Excitingly, dye **10** also exhibits an emission peak at ~1092 nm in the NIR II region, which is almost 200 nm Stokes shift (Figure 13). This observed emission is broad extending from 950 nm to just beyond 1400 nm in dichloromethane with a quantum yield (Φ) of ~0.03% when using a cyanine references dye (C5).[55] While this Φ appears low, we stress that very few molecular emissive materials exist in this region.[49] Additionally, a range of solvent polarities were evaluated to access the polarity of **RhIndz** in the ground-state via absorption spectroscopy and in the excited-state via fluorescence spectroscopy (Figure S2, Table S3). Both the absorption and emission

maxima varied by <0.04 eV in energy for solvents ranging in dipole from 3.96 debye to 0.36 debye and with dielectric constants ranging from 46.7 to 3.96. These very large ranges of solvent properties show very small changes in the absorption maxima, which indicates minimal conformational or localized charge density changes occurring in the ground or excited state of 10 due to the solvent properties.

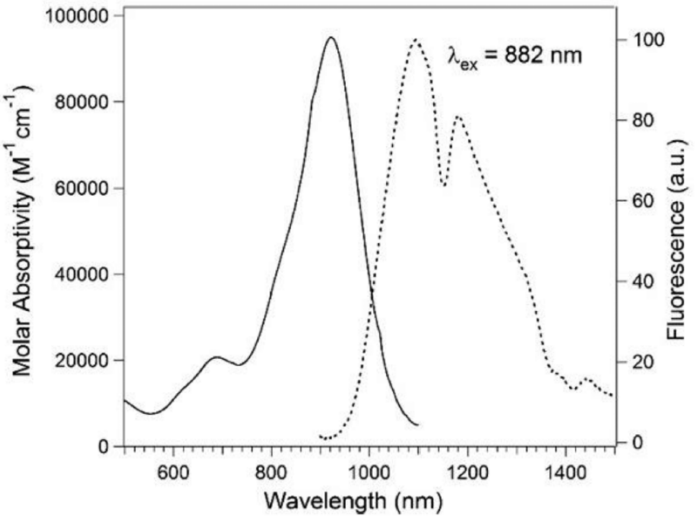

Figure 13. Molar absorptivity and emission of **RhIndz** ethyl ester in dichloromethane. Note: the drop in the emission spectrum at ~1150 nm is a possible spectrometer artifact (see Figure S3).

CONCLUSION

In conclusion, we have demonstrated the use of C−H bond functionalization reaction to prepare NIR II emissive dyes by the combination of the electron rich indolizine donor with the electron poor xanthene core. The best condition found was $PdCl_2(PPh_3)_2$ catalyst with KOAc base and NMP as solvent at 110 °C. **CNRhIndz** and **MeORhIndz** were also prepared by the C-bond activation reaction, while **CF_3RhIndz**, **(diCF_3)-RhIndz** and **OHRhIndz** only gave trace amounts of the product, with recovery of the starting materials. The **RhIndz** dye, while not a typical rhodamine structure with

N-xanthene bonds, was nonfluorescent in the closed spirocyclic structure; however, with the formation of the opened ethyl ester derivative, the fluorophore possessed absorption and emission within the NIR II region with high molar absorptivity and a Φ of ~0.03%. To the best of our knowledge, this is the first xanthene-based emissive dye with photophysical properties in the NIR II region.

EXPERIMENTAL SECTION

General Methods. All chemicals and solvents were purchased from commercial suppliers and used without further purification unless otherwise specified. ^{1}H NMR (500 MHz) and ^{13}C NMR (500 MHz) spectra were recorded in deuterated solvents on a Bruker AVANCE 500 NMR Spectrometer. J values are expressed in Hz and quoted chemical shifts are in ppm downfield from tetramethylsilane (TMS) reference using the residual protonated solvents as an internal standard. The signals have been designated as follows: s (singlet), d (doublet), t (triplet), m (multiplets). High resolution mass spectra (HRMS) were determined on Bruker-micrOTOF-Q II Mass Spectrometer. Melting point was recorded on a Thermal Analysis (TA) Differential Scanning Calorimeter (Q200) under nitrogen flow. Absorption spectra were acquired using a Cary 5000 UV−vis-NIR spectrophotometer in a 1 cm quartz cell. Fluorescence spectra were acquired using a Horiba QuantaMaster 8075−21 spectrofluorometer with xenon lamp excitation and liquid nitrogen cooled indium gallium arsenide solid state detector. The choice of 882 nm excitation was chosen to coincide with a Xe emission peak. The relative quantum yield of the rhodindolizine dye was calculated using a technique previously outlined by Miller et al.[35] A cyanine dye was chosen as the standard due to the similar absorption and emissive

regions. The dye, C5, has a known quantum yield of 2.2%.[54] The absorbance point for the quantum yield was chosen because of similar overlap in the absorption spectra between the standard and the rhodindolizine dye. An excitation wavelength of 870 nm was used for both the C5 and rhodindolizine dyes. Both samples were solvated in DCM to a 10 μM concentration.

3-Oxo-3H-spiro[isobenzofuran-1,9'-xanthene]-3',6'-diylbis-(trifluoromethanesulfonate) (**1**). Title compound was prepared according to literature procedure.[98]

3',6'-Dibromofluoran (**3**). Title compound was prepared according to literature procedure.[101]

Representative Procedure for the Preparation of RhIndz (**2a**) (Table 1). Compound **1** (50 mg, 0.083 mmol), 1-methyl-2- phenylindolizine (35 mg, 0.167 mmol), solvent (0.34−2.0 mL), catalyst (5−10 mol %), base, and additives (pivalic acid) were placed in a microwave sealed tube, flushed with nitrogen and heated for 12− 24 h at 80−150 °C according to Table 1. The reactions were monitored by TLC and NMR. Once it was determined that the reaction conversion has plateaued, the crude was diluted with 30 mL of dichloromethane and washed with water (5 × 10 mL). The crude product was dried over anhydrous sodium sulfate, filtered, and concentrated under reduced pressure.

3',6'-Bis(1-methyl-2-phenylindolizin-3-yl)-3H-spiro[2-benzofuran- 1,9'-xanthen]-3-one (**2a**). The crude product was purified by column chromatography on silica gel (hexane:ethyl acetate, 70:30) to give the product (**2a**) as a light-yellow solid in 20% yield (12 mg). mp 331.4−348.4 °C. ^{1}H NMR (500 MHz, CD_2Cl_2) δ 8.11 (d, J = 7.2 Hz, 2H), 8.00 (d, J = 7.6 Hz, 1H), 7.73 (td, J = 7.6, 1.1 Hz, 1H), 7.68−7.63 (m, 1H), 7.40 (d, J =

9.0 Hz, 2H), 7.33−7.20 (m, 13H), 6.97 (dd, J = 8.2, 1.7 Hz, 2H), 6.78 (d, J = 8.2 Hz, 2H), 6.73−6.68 (m, 2H), 6.46 (t, J = 6.7 Hz, 2H), 2.31 (d, J = 4.5 Hz, 6H). $^{13}C\{^{1}H\}$ NMR (126 MHz, CD_2Cl_2) δ 169.6, 153.3, 152.0, 135.82, 135.79, 135.1, 131.4, 131.2, 130.6, 129.3, 128.8, 128.6, 127.1, 126.9, 126.3, 126.2, 125.6, 124.6, 124.5, 124.3, 122.5, 120.4, 119.6, 118.7, 118.1, 117.9, 117.7, 117.2, 111.2, 108.2, 82.8, 9.5. HRMS-ESI-TOF (*m/z*) $[M + H]^+$ calcd for $C_{50}H_{34}N_2O_3$ 711.2642, found 711.2642.

3'-(1-Methyl-2-phenylindolizin-3-yl)-3-oxo-3H-spiro[2-benzofuran- 1,9'-xanthen]-6'-yl trifluoromethanesulfonate (**2b**). The crude product was purified by column chromatography on silica gel (hexane:ethyl acetate, 70:30) to give the product (**2b**) as a light yellow solid in 22% yield (12 mg). mp 234.6−256.8 °C. ^{1}H NMR (500 MHz, CD_2Cl_2) δ 8.14 (s, 1H), 8.03 (d, J = 6.6 Hz, 1H), 7.73− 7.67 (m, 2H), 7.54 (s, 1H), 7.41 (d, J = 7.7 Hz, 1H), 7.32−7.24 (m, 8H), 7.00−7.01 (m, 1H), 6.92 (br, s, 1H), 6.81−6.82 (m, 1H), 6.71 (br, s, 1H), 6.47 (br, s, 1H), 2.32 (s, 3H). $^{13}C\{^{1}H\}$ NMR (126 MHz, CD_2Cl_2) δ 169.4, 153.2, 152.8, 152.3, 151.9, 135.86, 135.85, 135.8, 135.14, 135.12, 131.47 131.45, 131.2, 130.6, 129.5, 129.3, 128.8, 128.7, 126.9, 126.4, 125.6, 124.6, 122.5, 120.3, 118.8, 118.2, 118.1, 117.9 (q, JC−F = 320 Hz), 117.2, 111.3, 111.0, 108.2, 82.4, 9.5. HRMS-ESI-TOF (*m/z*) $[M + K]^+$ calcd for $C_{36}H_{22}F_3NO_6SK$ 692.0752, found 692.0751.

Representative Procedure for the Preparation RhIndz and Phenyl-Substituted RhIndz (Table 2 and Table 3). The reaction was carried out in a sealed tube under nitrogen atmosphere in the presence of 3′,6′-dibromofluoran (**3**) (0.458 g, 1 mmol), 1-methyl-2- phenylindolizine (0.456 g, 2.2 mmol), solvent (3 mL), catalyst (10 mol %), base, and additives (PivOH) for 18−24 h at 110 °C. The reactions were monitored by

TLC and 1H NMR. Once it was determined that the reaction conversion had plateaued, the crude was diluted with 30 mL of dichloromethane and washed with water (5 × 10 mL). The crude product was dried over anhydrous sodium sulfate, filtered, and concentrated under reduced pressure. The crude product was purified by column chromatography on silica gel (hexane:ethyl acetate, 70:30) to give the product (**2a**) as a light-yellow solid in 35% yield (244 mg).

4-(3-{3'-[2-(4-Cyanophenyl)-1-methylindolizin-3-yl]-3-oxo-3-Hspiro[2-benzofuran-1,9'-xanthen]-6'-yl}-1-methylindolizin-2-yl)- benzonitrile (**4a**). Yellow solid, 30% yield, (25 mg). mp 238.9−259.1 °C. ^{1}H NMR (500 MHz, CD_2Cl_2) δ 8.09 (d, J = 7.1 Hz, 2H), 8.03 (d, J = 7.6 Hz, 1H), 7.77 (t, J = 7.5 Hz, 1H), 7.68 (t, J = 7.5 Hz, 1H), 7.59 (d, J = 8.1 Hz, 4H), 7.42 (d, J = 9.0 Hz, 2H), 7.33 (d, J = 8.0 Hz, 4H), 7.28 (d, J = 7.7 Hz, 1H), 7.22 (s, 2H), 6.93 (d, J = 8.2 Hz, 2H), 6.82 (d, J = 8.2 Hz, 2H), 6.76−6.71 (m, 2H), 6.50 (t, J = 6.8 Hz, 2H), 2.32 (s, 6H). ^{13}C{^{1}H} NMR (126 MHz, CD_2Cl_2) δ 169.5, 153.2, 152.0, 141.1, 135.9, 134.5, 132.5, 131.8, 131.7, 130.7, 129.2, 127.3, 127.0, 126.5, 125.7, 124.5, 122.5, 120.6, 119.6, 118.9, 118.4, 118.3, 117.7, 111.9, 110.5, 108.1, 82.5, 9.5. HRMS-ESI-TOF (*m/z*) $[M + K]^+$ calcd for $C_{52}H_{32}N_4O_3K$ 799.2106, found 799.2106.

3'-(2-(4-Cyanophenyl)-1-methylindolizin-3-yl)-3-oxo-3H-spiro[2- benzofuran-1,9'-xanthen]-6'-yltrifluormethanesufonate (**4b**). Yellow solid, 14% yield, (9 mg). mp 239.4−255.3 °C. ^{1}H NMR (300 MHz, CD_2Cl_2) δ 8.11 (d, J = 7.2 Hz, 1H), 8.04 (d, J = 7.4 Hz, 1H), 7.79−7.72 (m, 1H), 7.72−7.65 (m, 1H), 7.61 (s, 1H), 7.59 (s, 1H), 7.57−7.54 (m, 1H), 7.43 (d, J = 9.0 Hz, 1H), 7.38−7.30 (m, 3H), 7.26 (d, J = 5.6 Hz, 2H), 7.00−6.91 (m, 2H), 6.85 (d, J = 8.2 Hz, 1H), 6.74 (dd, J = 8.7, 6.5 Hz, 1H), 6.50 (t, J = 6.8 Hz, 1H), 2.33 (d, J = 2.8 Hz, 3H). ^{13}C{^{1}H} NMR (126 MHz, CD_2Cl_2) δ 169.6, 153.4, 152.1, 152.0,

142.8, 141.1, 135.9, 134.4, 132.5, 131.8, 131.8, 130.7, 129.21, 129.16, \ 127.3, 126.8, 126.4, 125.7, 124.5, 123.3, 122.5, 120.7, 119.6, 119.3, 119.0, 118.4, 118.3, 117.7, 116.2, 111.9, 110.5, 108.1, 82.4, 9.6. HRMS-ESI-TOF (*m/z*) $[M + K]^+$ calcd for $C_{36}H_{21}BrN_2O_3K$ 609.0808, found 609.0877.

3',6'-Bis(2-(3,5-bis(trifluoromethyl)phenyl)-1-methylindolizin-3- yl)-3H-spiro[2-benzofuran-1,9'-xanthen]-3-one (**5a**). Brown solid, 11% yield (10 mg). mp 200.5−230.4 °C. ^{1}H NMR (300 MHz, CD_2Cl_2) δ 8.09 (d, J = 7.2 Hz, 2H), 8.02 (d, J = 7.5 Hz, 1H), 7.78− 7.72 (m, 1H), 7.70−7.64 (m, 1H), 7.57 (d, J = 8.1 Hz, 4H), 7.42 (d, J = 9.0 Hz, 2H), 7.36 (d, J = 8.0 Hz, 4H), 7.29 (d, J = 7.6 Hz, 1H), 7.23 (d, J = 1.5 Hz, 2H), 6.96 (dd, J = 8.2, 1.6 Hz, 2H), 6.82 (d, J = 8.2 Hz, 2H), 6.73 (dd, J = 8.9, 6.5 Hz, 2H), 6.52−6.45 (m, 2H), 2.32 (s, 6H). ^{13}C{^{1}H} NMR (126 MHz, CD_2Cl_2) δ 169.5, 153.2, 152.1, 140.0, 135.9, 134.7, 131.6, 131.5, 130.7 (q, 2JC−F = 32 Hz), 129.1, 128.8, 128.5 (q, 3JC−F = 4 Hz), 127.6, 127.0, 126.4, 126.2, 125.7, 125.6, 125.5, 124.5 (q, 1JC−F = 272 Hz), 124.0, 122.5, 120.6, 118.9, 118.3, 118.2, 117.6, 111.7, 108.2, 82.6, 9.5. HRMS-ESI-TOF (*m/z*) $[M + H]^+$ calcd for $C_{52}H_{32}F_6N_2O_3H$ 847.2389, found 847.2389.

3'-(1-Methyl-2-(4-(trifluoromethyl)phenyl)indolizin-3-yl)-3-oxo- 3H-spiro[2-benzofuran-1,9'-xanthen]-6'-yltrifluoromethanesulfonate (**5b**). Brown solid, 6% yield (5 mg). mp 205.9−255.9 °C. ^{1}H NMR (300 MHz, CD_2Cl_2) δ 8.11 (d, J = 7.2 Hz, 1H), 8.04 (d, J = 7.3 Hz, 1H), 7.71 (dt, J = 20.2, 7.2 Hz, 2H), 7.62−7.51 (m, 3H), 7.47− 7.23 (m, 6H), 6.99 (d, J = 8.1 Hz, 1H), 6.93 (d, J = 8.1 Hz, 1H), 6.85 (d, J = 8.2 Hz, 1H), 6.78−6.69 (m, 1H), 6.49 (t, J = 6.7 Hz, 1H), 2.33 (s, 3H). ^{13}C{^{1}H} NMR (126 MHz, CD_2Cl_2) δ 169.6, 153.4, 152.11, 152.06, 142.8, 140.0, 135.9, 134.7, 131.6, 131.5, 130.7 (q, 2JC−F = 32 Hz), 129.2, 129.1, 128.5 (q, 3JC−F = 4 Hz), 127.6, 126.9, 126.4, 125.7,

125.57, 125.55, 124.5 (q, 1JC−F = 272 Hz), 123.2, 122.5, 120.6, 119.3, 119.0, 118.3, 118.2, 117.5, 116.2, 111.7, 108.2, 82.4, 9.6. HRMS-ESITOF (*m/z*) $[M + K]^+$ calcd for $C_{36}H_{21}BrF_3NO_3K$ 690.0288, found 690.0284.

3',6'-Bis(2-(4-methoxyphenyl)-1-methylindolizin-3-yl)-3H-spiro- [2-benzofuran-1,9'-xanthen]-3-one (**9a**). Pale green solid, 20% yield (17 mg). mp 236.2−255.2 °C. ^{1}H NMR (500 MHz, CD_2Cl_2) δ 8.11 (d, J = 7.1 Hz, 2H), 8.01 (d, J = 7.6 Hz, 1H), 7.74 (t, J = 7.4 Hz, 1H), 7.66 (t, J = 7.3 Hz, 1H), 7.39 (d, J = 8.9 Hz, 2H), 7.31−7.23 (m, 3H), 7.13 (t, J = 9.3 Hz, 4H), 6.96 (d, J = 8.2 Hz, 2H), 6.85 (d, J = 7.1 Hz, 4H), 6.78 (d, J = 8.1 Hz, 2H), 6.68 (dd, J = 15.7, 7.7 Hz, 2H), 6.44 (t, J = 6.7 Hz, 2H), 3.79 (s, 6H), 2.29 (s, 6H). $^{13}C\{^1H\}$ NMR (126 MHz, CD_2Cl_2) δ 169.6, 158.9, 153.3, 152.0, 135.8, 135.3, 132.2, 131.5, 130.6, 128.9, 128.8, 127.9, 127.1, 126.3, 125.6, 124.6, 122.4, 120.3, 118.7, 118.0, 117.8, 117.1, 114.1, 111.1, 108.2, 82.8, 55.7, 9.5. HRMSESI- TOF (*m/z*) $[M + K]^+$ calcd for $C_{52}H_{38}N_2O_5K$ 809.2412, found 809.2411.

(Z)-3-(9-(2-(Ethoxycarbonyl)phenyl)-6-(1-methyl-2-phenylindolizin- 3-yl)-3H-xanthen-3-ylidene)-1-methyl-2-phenyl-3H-indolizin-4- ium (**10**). Compound **2a** (80 mg, 0.112 mmol) was transferred to a 150 mL two neck round-bottom flask and flushed with nitrogen thoroughly for 10 min. 1,2-Dichloroethane (4.8 mL) and $POCl_3$ (0.03 mL) were added to the flask and the reaction was refluxed for 4 h. The reaction mixture was allowed to cool to room temperature and concentrated under reduced pressure to give a green solid, which was used in the next step without further purification. The reaction mixture was thoroughly flushed with nitrogen for 10 min, followed by the addition of dry ethanol (3.0 mL), and stirring at 50 °C for 24 h. The reaction mixture was concentrated under reduced pressure and the solid was dissolved in chloroform (20 mL). The organic

layer was washed with water (8 × 10 mL), dried over anhydrous sodium sulfate, filtered and concentrated under reduced pressure to give a green solid. The solid was then washed with hot hexane (20 × 5 mL), and recrystallize from hexane:ethyl acetate mixture to give 28 mg of a green solid in 34% yield. mp 303.7−329.1 °C. ^{1}H NMR (500 MHz, CD_2Cl_2) δ 8.32 (s, 1H), 8.11 (d, J = 5.9 Hz, 1H), 8.01 (d, 1H), 7.79 (s, 2H), 7.73 (s, 1H), 7.66 (t, 1H), 7.57 (s, 1H), 7.41 (s, 4H), 7.27 (dd, J = 29.1, 13.4 Hz, 10H), 6.93 (d, J = 26.1 Hz, 2H), 6.83 (d, J = 6.4 Hz, 1H), 6.78 (d, J = 7.4 Hz, 1H), 6.70 (t, 1H), 6.46 (t, 1H), 4.09 (q, 2H), 2.35−2.23 (m, 6H), 1.31 (t, 3H). ^{13}C{^{1}H} NMR (126 MHz, $CDCl_3$) δ 165.4, 161.2, 157.1, 142.7, 137.5, 135.3, 134.7, 134.6, 134.4, 133.9, 133.3, 131.3, 131.2, 131.1, 130.9, 130.8, 130.7, 130.2, 129.3, 129.1, 129.0, 128.8, 128.5, 128.4, 127.8, 126.6, 126.0, 125.4, 124.9, 124.0, 122.2, 122.14, 122.09, 118.34, 118.30, 117.9, 117.4, 116.9, 115.1, 114.3, 113.1, 111.0, 107.9, 61.9, 14.3, 9.4. HRMS-ESI-TOF (*m/z*) $[M]^+$ calcd for $C_{52}H_{39}N_2O_3^+$ 739.2955, found 739.2924.

CHAPTER IV.

Water-Soluble NIR Absorbing and Emitting Indolizine Cyanine and Indolizine Squaraine Dyes for Biological Imaging

Adapted with permission from **William E. Meador**, Shane A. Autry, Riley N. Bessetti, Jacqueline N. Gayton, Alex S. Flynt, Nathan I. Hammer, and Jared H. Delcamp.

J. Org. Chem. 2020, 85, 4089 (Copyright (2020) ACS Online Library).

(See Appendix D. for permission license)

William Meador synthesized and characterized all of the materials in the paper, conducted photostability studies, performed the absorption spectroscopy, and wrote the manuscript. Jacqueline Gayton advised and aided in the synthesis of the materials. Shane A. Autry gathered fluorescence emission data and calculated quantum yields. Riley N. Bessetti and Alex S. Flynt performed cytotoxic analyses and cellular imaging experiments. All other PIs contributed experimental design and intellectual merit.

All Supplemental Information Items are provided in Appendix C.

ABSTRACT

Organic dyes that absorb and emit in the near-infrared (NIR) region are potentially noninvasive, high-resolution, and rapid biological imaging materials. Indolizine donor-based cyanine and squaraine dyes with water-solubilizing sulfonate

groups were targeted in this study due to strong absorptions and emissions in the NIR region. As previously observed for nonwater-soluble derivatives, the indolizine group with water-solubilizing groups retains a substantial shift toward longer wavelengths for both absorption and emission with squaraines and cyanines relative to classically researched indoline donor analogues. Very high quantum yields (as much as 58%) have been observed with absorption and emission >700 nm in fetal bovine serum. Photostability studies, cell culture cytotoxicity, and cell uptake specificity profiles were all studied for these dyes, demonstrating exceptional biological imaging suitability.

INTRODUCTION

Near-infrared (NIR) emissive materials are intensely researched due to a plentiful number of practical applications, including biological imaging,[49-50, 52, 78, 103-106] photodynamic therapy,[47, 69, 79, 103, 107] telecommunications,[4, 108-109] secure displays, which can be coupled to night vision technologies,[3, 48, 110] and many other innovative areas of research.[8, 106, 111-112] NIR biological imaging agents use low-energy photons in a spectral region where tissue is readily penetrated at a maximal depth optically.[5, 13, 49, 79] The desirable properties of biological imaging dyes include (1) absorbing and emitting light in the "therapeutic window" ranging from 700 to 1400 nm, (2) a significant Stokes shift to enable high-precision imaging, (3) efficient absorption and emission of photons through both a high molar absorptivity and quantum yield, and (4) water solubility. While there are many exciting dye design prospects being pursued in the literature,[104] exceptional NIR emissive materials are still needed for practical biological imaging since current dyes fall short of meeting all of the desired criteria simultaneously.

Among NIR emissive dyes, squaraines[112-113] and cyanines[1, 8] are ubiquitous.[7, 50, 103] Previous research has frequently investigated indoline donor-based cyanine and squaraine dyes with indocyanine green (ICG) having been awarded FDA approval several decades ago.[6, 114] Both of these classes of dyes need design strategies that allow access to longer wavelength NIR photons in aqueous environments.[104] In fact, the indoline squaraine absorbs outside the therapeutic window, which renders it impractical for use as a noninvasive biological imaging agent.[25] To deepen the NIR absorbing properties of these dye classes, designs capable of extending the π-system through a conjugated donor (such as indolizine) are attractive.[25, 54-55, 115] Recent photophysical studies using proaromatic indolizine donors in place of indoline donors show redshifting of the absorption and emission profiles of these dyes firmly into the therapeutic window in nonaqueous environments (**C5** and **SQ** compared to ICG and indoline squaraine, respectively; Figure 14).[25, 54-55, 115] These studies indicated that in the case of phenyl-indolizine derivatives, the phenyl group does not play a significant role in tuning the absorption or emission energy values of the NIR indolizine dyes.[25, 54] This enables the use of the phenyl group to append water-soluble functionality without perturbing the core chromophore properties of the dyes, permitting the probing of the photophysical properties of the dyes in aqueous environments. Sulfonate-substituted dyes, **SO$_3$C5** and **SO$_3$SQ**, were targeted given the water-solubilizing properties of sulfonate groups and FDA approval for human use by way of ICG (Figure 14). This work aims to compare the photophysical properties of **SO$_3$C5**, **SO$_3$SQ**, and benchmark ICG in a biologically relevant medium.

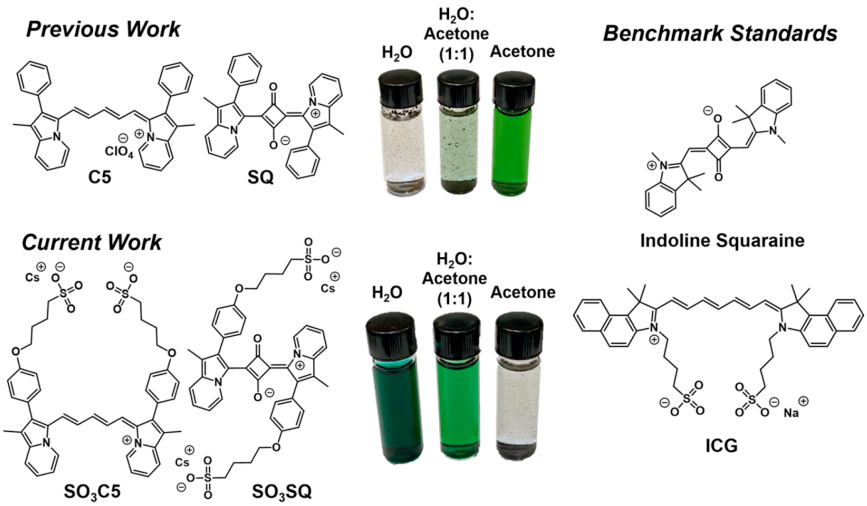

Figure 14. Current work demonstrating water solubility of indolizine cyanine and indolizine squaraine dyes using sulfonate groups.

SYNTHESIS

The target dyes were synthesized in two steps from previously reported indolizine phenol **1** (Scheme 2).[25] First, **1** was alkylated with butane sultone (**2**) in the presence of base to give sulfonate indolizine **3**. Interestingly, this reaction required a careful selection of solvent and base to avoid significant side product formation as a carbon alkylated product (see Table S1 and Figure S1). Intermediate **3** is common to both **SO_3C5** and **SO_3SQ** target dyes. The target sulfonate indolizine cyanine dye (**SO_3C5**) is synthesized by reacting **3** with the methine bridge linker **4** in the presence of perchloric acid and acetic anhydride at room temperature similar to previously reported conditions in the literature.[54] The target sulfonate indolizine squaraine (**SO_3SQ**) is synthesized via an electrophilic aromatic substitution/condensation reaction between sulfonate indolizine **3** and squaric acid (**5**). Importantly, during optimization of the condensation reaction, it was found that the addition of small amounts of water led to an increase in product formation. Ultimately, running the reaction in nondried laboratory-grade methanol gave the highest

yields (Table S2). Both target dyes are formed in an approximately 50% overall yield in this route over two steps.

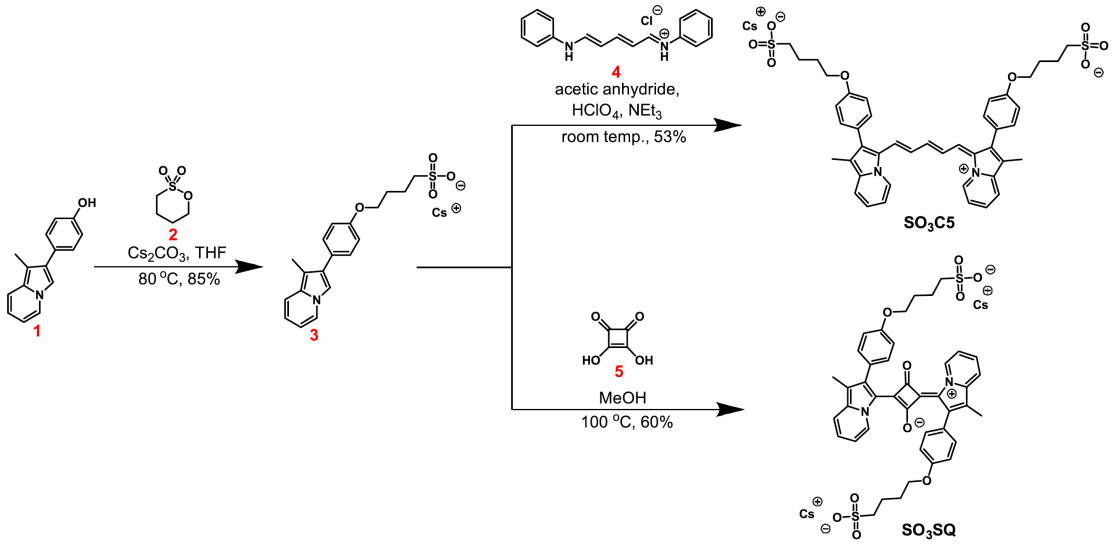

Scheme 2. Synthetic Route to **SO_3C5** and **SO_3SQ**.

RESULTS AND DISCUSSION

With **SO_3C5** and **SO_3SQ** in hand, absorption and emission studies were undertaken for comparison to ICG as a benchmark reference dye (Figures 15, S2 and S3; Table 8). Dimethyl sulfoxide (DMSO) and MeOH were also selected as solvents, which allows for the comparison of **SO_3C5** and **SO_3SQ** to the previously reported dyes **C5** and **SQ**, respectively (see Table S3 for solubility data).[25, 54] H_2O and fetal bovine serum (FBS) were selected as well due to the biological relevance and for a convenient analysis of how these dyes will behave with biological matrix elements in place, as has been previously reported in the literature.[15, 49, 116] The absorption profiles of both dyes in DMSO and MeOH are not significantly changed relative to the previously published dyes with no sulfonate groups.[25, 54] The absorption curves in H_2O and FBS are similar to the curves observed in DMSO and MeOH for **SO_3SQ**; however, the absorption curve of **SO_3C5** in water deviates shape significantly, which is likely due to aggregation in water

(Figure S4). Upon changing concentrations, no significant evidence of aggregate disruption could be observed down to concentrations near the detection limit of the spectrometer (Figure S5). Notably, the evidence of aggregation of **SO_3SQ** (modest amounts) and ICG (significant amounts) in H_2O at concentrations of $\geq 10^{-5}$ M is apparent at higher energy wavelengths when the absorption curves are overlaid with curves at 10^{-6} M in H_2O, which appear to have disrupted aggregate features (Figures S6 and S7).[117] It should be noted that while all three dyes were observed to form aggregates in H_2O via dynamic light scattering analysis at 5×10^{-6} M (Figure S8), **SO_3C5** is the only dye that shows a significant impact of this aggregative behavior from the absorption profile. Interestingly, upon dissolving **SO_3C5** in FBS, the original curve shape observed in DMSO and MeOH is regained with a notable red shift of the λ_{max} value by about 40 nm (Figure 15).

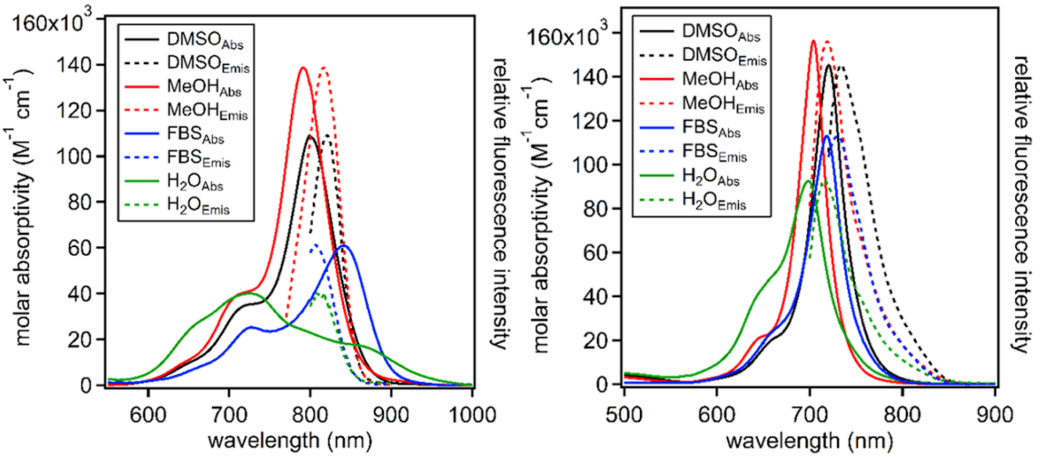

Figure 15. Vis−NIR region molar absorptivity and normalized fluorescence emission of **SO_3C5** (left) and **SO_3SQ** (right) in DMSO, MeOH, H_2O, and FBS at 5×10^{-6} M.

FBS is commonly used in photophysical studies for NIR dyes intended for biological use as the albumin proteins help to better separate dye molecules from one another as is dramatically demonstrated here. The disruption of aggregation under

biologically relevant conditions is encouraging as it leads to the minimization of thermal relaxations resulting in increased quantum yields. For comparison, the curve shape of ICG retains the same profile in all four solvents (Figure S3). The molar absorptivities are similar for **SO_3C5** and **SO_3SQ** in MeOH and DMSO at approximately 110,000−150,000 M^{-1} cm^{-1} (Figure 15 and Table 8). In H_2O and FBS, the **SO_3C5** molar absorptivities drop substantially to ~60,000 M^{-1} cm^{-1} or less. For **SO_3SQ** in H_2O or FBS, the molar absorptivities remain significantly higher at 113,000−93,000 M^{-1} cm^{-1}. The molar absorptivity values and order of λ_{max} values follow the same trend for **SO_3SQ** and ICG with each of the four solvents. **SO_3C5** deviates from this trend with obvious aggregation in water-based solutions. Compared to ICG, the λ_{max} of **SO_3C5** is shifted toward lower energy values (~15 nm), and the λ_{max} of **SO_3SQ** is shifted toward higher energy by about 100 nm (0.21 eV, Table 8).

Table 8. Optical Properties of **SO_3C5**, **SO_3SQ**, and ICG in Water, Fetal Bovine Serum (FBS), Methanol, and DMSO

dye	solvent	abs. max. (nm)	emis. max. (nm)	stokes shift (nmleVlcm^{-1})	ε (M^{-1} cm^{-1})	Φ (%)	MB ($\varepsilon \times \Phi$)
SO_3C5	DMSO	801	821	20 I 0.04 I 304	109 000	2.0	2180
	MeOH	791	817	26 I 0.05 I 403	139 000	0.3	420
	FBS	842	808		61 000	0.1	60
	water	726	808		40 000	0.05	20
SO_3SQ	DMSO	720	734	14 I 0.03 I 265	145 000	8.6	12 500
	MeOH	704	719	15 I 0.04 I 296	156 000	0.8	1250
	FBS	719	730	11 I 0.03 I 210	113 000	58.3	65 900
	water	698	716	18 I 0.04 I 360	93 000	0.3	280
ICG	DMSO	794	825	31 I 0.06 I 473	211 000	11.0	23 200
	MeOH	784	819	35 I 0.07 I 545	230 000	4.3	9900
	FBS	798	827	29 I 0.05 I 439	174 000	9.3	16 200
	water	779	812	33 I 0.06 I 522	157 000	0.5	780

Fluorescence spectroscopy was probed with each of the dyes to understand the excited-state behavior. Prior reports on **C5** and **SQ** in organic solvents such as dichloromethane have shown Stokes shifts of 43 and 50 nm, respectively (taken as the difference between the λ_{max}^{abs} and λ_{max}^{emis}).[25, 54-55] The Stokes shifts of both sulfonate dyes decreased to ≤26 nm (≤400 cm^{-1}) in all solvents where single molecule behavior is

likely occurring. As the magnitude of the Stokes shift is directly related to the reorganization energy of the dye, the decrease in the Stokes shift demonstrates that there is smaller reorganization energy of **SO_3SQ** and **SO_3C5** relative to the nonsulfonate substituted dyes. Stokes shifts for **SO_3C5** could not be determined in FBS and H_2O due to the presence of multiple species due to aggregation, leading to apparent emission energies higher than the lowest energy features of the combined absorption spectrum of all monomer and aggregate states. This suggests that in aqueous solvents, the higher-energy absorption feature of **SO_3C5** corresponds to the observed emission, while the lower-energy absorption feature is either weakly emissive or has an emission beyond the InGaAs fluorimeter detection limit.

Quantum yields (Φ) for each dye were calculated as relative values with respect to ICG in DMSO at 11.0% as the benchmarking system (Table 8).[36] The quantum yields for ICG in water, MeOH, and FBS were calculated with respect to ICG in DMSO. Previously reported quantum yields for **C5** in organic solvents ranged from 2.0 to 3.6%;[54-55] however, **SO_3C5** shows Φ values below 1% in all three protic solvents examined. In DMSO, a Φ of 2% is observed, which is similar to the values observed for the parent **C5** structure. The Φ data for **SO_3SQ** is exceptionally intriguing. In water or methanol, the Φ of **SO_3SQ** is <1%, which is not uncommon in the NIR spectral region. Upon changing the solvent environment to DMSO, a significantly increased Φ value of 8.6% is observed, which can be rationalized as the protic environments promoting nonradiative decay pathways leading to low Φ values in water and methanol. However, **SO_3SQ** in FBS gives a 58% quantum yield, which is a number that is truly remarkable in the field of NIR dyes and encourages further studies with this material. The dramatic

enhancement of Φ values in the complex biologically relevant environment of FBS has been previously observed in the literature.[116] By comparison, the benchmark dye ICG shows a much lower 9% Φ in FBS.

An important metric for biological imaging materials is the molecular brightness (MB), which balances the contributions of ε and Φ through the equation MB = ε × Φ. MB is a good indicator of the amount of dye needed to give comparable fluorescence signal intensities among dyes with varying molar absorptivities and quantum yields. The MB values for **SO_3C5** are quite low in all solvents at ≤2,180 M^{-1} cm^{-1} when compared with ICG at a maximum value of 23,000 M^{-1} cm^{-1} in DMSO (Table 8). Notably, the observed MB value for ICG is low in H_2O at 780 M^{-1} cm^{-1} but remains high in the remaining solvents examined (>9,000 M^{-1} cm^{-1}). **SO_3SQ** shows an MB value of >65,000 M^{-1} cm^{-1} in FBS, which is dramatically larger than the substantial 23,000 M^{-1} cm^{-1} value for ICG and is likely one of the largest values in this spectral region known in the literature. This indicates that significantly less dye (∼3 × less) would be needed with **SO_3SQ** to generate the same amount of signal as ICG.

A key desirable property of biological imaging dyes is prolonged photostability.[24] To probe this, **SO_3C5**, **SO_3SQ**, and ICG were dissolved in water under an ambient atmosphere at a concentration of 1×10^{-6} M and irradiated with a solar-simulated light-emitting diode (LED) spectrum from 400 to 1,100 nm with white light irradiation (Figures 16 and S9−S11). Under these conditions, ICG has a half-life of approximately 35 min with complete consumption by 80 min. Both **SO_3C5** and **SO_3SQ** show a higher photostability than ICG with half-lives of 50 and 100 min, respectively. The higher photostability of **SO_3SQ** can be attributed, in part, to the squaraine structure being devoid

of double-substituted alkenes, which are known to undergo various degradation pathways with ICG.[118] In MeOH, **SO_3SQ** and ICG are exceptionally stable with halflives >24 h (Figures S12−S15). **SO_3C5** is notably less stable than ICG or **SO_3SQ** in MeOH where the dye appears to be deaggregated, which suggests that the aggregate states of **SO_3C5** in water could impart some photostability since this dye is more stable than ICG in water. Overall, **SO_3SQ** has a likely record quantum yield in this spectral region, a high molar absorptivity, an exceptional molecular brightness, and the highest photostability measured in this study in H_2O.

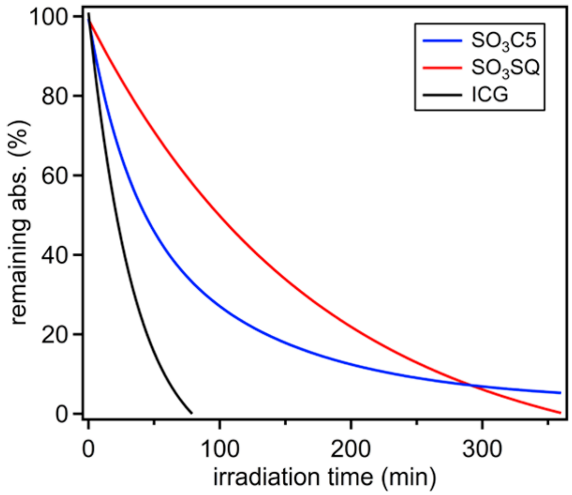

Figure 16. Photostability of **SO_3C5**, **SO_3SQ**, and ICG in water.

Finally, the cytotoxicity and cellular uptake of **SO_3C5** and **SO_3SQ** were examined with human (HEK293) and *Drosophila* (S2) tissue culture cells (Figure 17). HEK cells are a human cell line grown at physiological conditions found in mammals. Performance and cytotoxicity of the dyes in HEK cells inform in vivo biocompatibility for clinical and veterinary settings for use in diagnostic or therapeutic technologies. In contrast, S2 cells grow at a lower temperature under normal atmospheric conditions and are derived from invertebrates (fruit fly embryos). Dye behavior in these cells is a proxy for understanding

the environmental impact of these compounds. Both **SO_3C5** and **SO_3SQ** show < 25% HEK cell death at or below 2 mM concentrations. At high dye loadings (10 mM), cell death is near 30%, which indicates that these dyes are relatively benign toward a human cell line. A similar trend is observed with the cytotoxicity studies of the S2 cell line, although ≥2 mM **SO_3C5** and 10 mM **SO_3SQ** show >50% cell death. S2 cells are more phagocytically active compared to HEK293 cells, which may explain greater sensitivity to the dyes. This suggests that low-to-moderate concentrations of the dyes are not toxic to animal cells. **SO_3C5** and **SO_3SQ** cell uptake studies were undertaken with LysoTracker by comparing the fluorescence overlap of each NIR dye with LysoTracker. With these studies, the **SO_3C5** dye shows a Pearson's correlation coefficient of 0.9, indicating that HEK cells largely uptake this dye into the cell lysosomes. A similarly high Pearson's correlation coefficient is observed for **SO_3SQ** and S2 cells at 0.7. This shows that nonfavorable interactions of the dye with cell organelles are minimized.

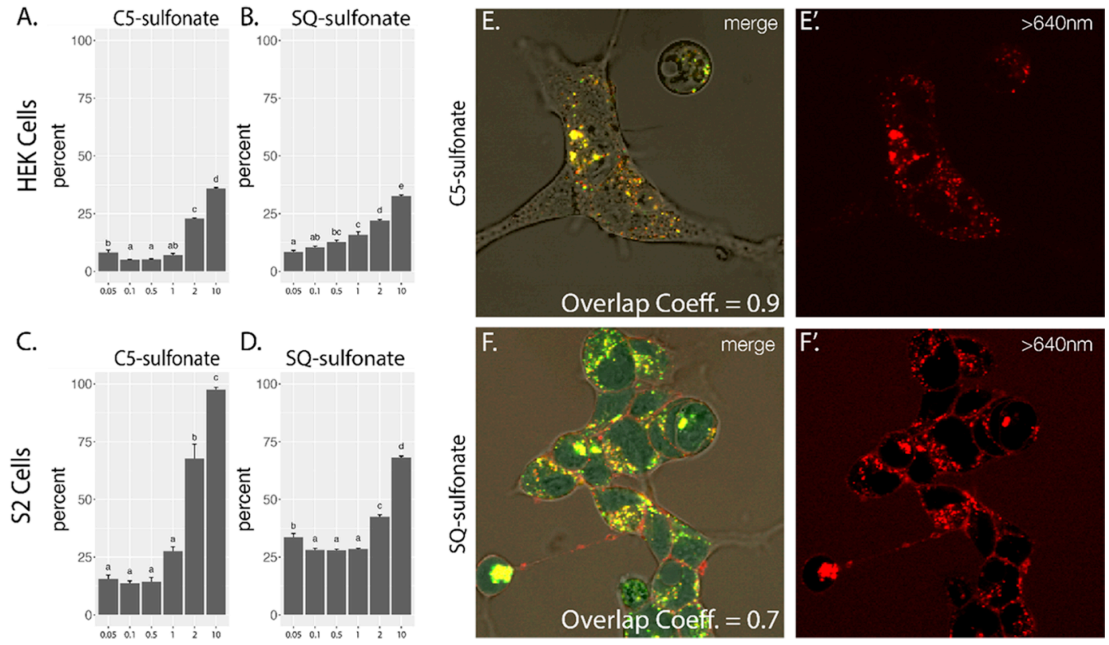

Figure 17. Interaction of **SO_3C5** and **SO_3SQ** dyes with human (HEK) and *Drosophila* (S2) cells. (A−D) Percent cytotoxicity for each combination as determined by the LDH assay. X-axis values are mM. Error bars represent standard error, and letter denotes significance groups determined by Tukey's HSD ($p \leq 0.05$). (E, F) Confocal images of live HEK (E) and S2 (F) cells after exposure to dye and LysoTracker. Left panels show the merging of bright field, lysotracker (green), and dye (red). Dye fluorescence alone is shown in the right panel (E′, F′). Pearson's correlation coefficient (noted as the overlap coefficient) shows colocalization between the dye and LysoTracker.

CONCLUSIONS

The need for biological imaging dyes that absorb and emit strongly in the NIR region is of paramount importance to society since this could enable noninvasive, nontoxic, and rapid imaging of medical patients and biological specimens. Indolizine donor-based cyanine and squaraine dyes with attached sulfonate groups were synthesized to provide a direct comparison in biological medium to benchmark ICG. The increased donor strength of the indolizine compared to that of the indoline allowed for these dyes to have a more red-shifted absorption and emission than their indoline counterparts. **SO_3SQ**

demonstrated a remarkable quantum yield of 58.3% (MB of > 65,000) in FBS, which is notable in that this is representative of the optical properties inside of a biological medium. **SO_3C5** shows significant concentration-independent aggregation effects in water, while **SO_3SQ** shows minimal aggregation in water. Prolonged irradiation studies demonstrate that both of the indolizine dyes have a significantly higher photostability than ICG in water. Cell culture studies exhibited high specificity for lysosomal uptake with overlap coefficients of 0.9 and 0.7 for **SO_3C5** and **SO_3SQ**, respectively, as well as low levels of cytotoxicity. The high molecular brightness, simple synthesis, prolonged photostability, and low toxicity of **SO_3SQ** show that it is an attractive potential NIR biological imaging material with very high metrics significantly surpassing the benchmark ICG over a range of tests.

EXPERIMENTAL SECTION

All commercially obtained reagents and solvents were used as received without further purification. All heating was done in an oil bath. Thinlayer chromatography (TLC) was conducted with Merck KGaA TLC silica gel 60 RP-18 F254S glass-backed plates and visualized with UV. Flash column chromatography was performed using a CombiFlash Rf + system. RediSep cartridges were charged with silica gel from RediSep Rf reversed-phase C18, 40−63 μm (230−400 mesh). ^{1}H and ^{13}C {1H} NMR spectra were recorded on a Bruker Ascend-300 (300 MHz) spectrometer and are reported in ppm using solvent as an internal standard (DMSO-d6 at 2.50 ppm and CD_3OD-d4 at 3.31 ppm). Data are reported as s = singlet, d = doublet, t = triplet, q = quartet, p = pentet, m = multiplet, b = broad, ap = apparent, dd = doublet of doublets, dt = doublet of triplets;

coupling constant(s) are in Hz; integration. UV−vis−NIR spectra were measured[13] with a Cary 5000 UV−vis−NIR spectrometer. For photostability studies, samples were irradiated with a Class AAA Rated G2V pico LED solar simulator providing a spectral range from 400 to 1,100 nm at 100 mW cm^{-2}. High-resolution mass spectrometry (HRMS) spectra were obtained with a quadrupole time-of-flight (QTOF) HRMS utilizing nanospray ionization. The mass analyzer was set to the 200−2,000 Da range. Infrared spectra were recorded with an Agilent Cary 660 attenuated total reflection-Fourier transform infrared (ATR-FTIR) spectrometer. All emission data was obtained using a Horiba PTI fluorimeter. Excitation wavelengths were achieved by passing white light through a dual-grating system. Photons were collected through a photomultiplier tube. The relative quantum yields were obtained using this equation:

$$\Phi_{\text{Sample}} = \Phi_{\text{Standard}} \cdot \frac{E_{\text{Sample}}}{E_{\text{Standard}}} \cdot \frac{A_{\text{Standard}}}{A_{\text{Sample}}} \cdot \frac{\eta^2_{\text{Sample}}}{\eta^2_{\text{Standard}}}$$

For the equation above, E is the sum of emission intensities and A is the maximum absorbance, η is the refractive index of the solvent used, and Φ denotes the quantum yield. The standard used to obtain the relative quantum yields was indocyanine green (ICG) with a quantum yield of 11% in DMSO.[36]

Cell Imaging. HEK293 cells were grown in standard conditions (37 °C, 5% CO_2) in Dulbecco's modified Eagle's medium (DMEM) media supplemented with 10% FBS. S2 cell cultures were maintained in S2 media with 10% FBS at 25 °C. Dye cytotoxicity was determined with a CyQUANT LDH Cytotoxicity Assay KitTM Invitrogen using a BioTek Synergy™ H1 microplate reader. Cells were imaged with a Zeiss LSM 510 META laser scanning confocal microscope following a 24 h exposure to dyes. Lysosome

was visualized with a LysoTracker Green DND-26 (Invitrogen) following the manufacturer's protocols.

Cesium 4-(4-(1-Methylindolizin-2-yl)phenoxy)butane-1-sulfonate (**3**). To a flame-dried round-bottom flask equipped with a stir bar and reflux condenser that had been purged with N2 for 10 min were added 4-(1-methylindolizin-2-yl)phenol (**1**) (1.00 g, 4.48 mmol),[25] Cs_2CO_3 (3.65 g, 11.20 mmol), and 1,4-butane sultone (**2**) (1.15 mL, 11.20 mmol). The reaction mixture was dissolved in tetrahydrofuran (THF) (140 mL) and heated to 80 °C in an oil bath for 16 h. The reaction mixture was cooled down to room temperature and yielded a light brown precipitate. Ethyl acetate was added (100 mL) to further precipitate the product, which was subsequently filtered to yield the crude material. The crude mixture was purified by recrystallization in water to yield a pure golden brown metallic in appearance solid (1.87 g, 85%). ^{1}H NMR (300 MHz, DMSO-d6; Figure S16) δ 8.13 (d, J = 6.9 Hz, 1H), 7.63 (s, 1H), 7.42 (d, J = 8.7 Hz, 2H) 7.37 (d, J = 9.1 Hz, 1H), 6.99 (d, J = 8.7 Hz, 2H), 6.60 (dd, J = 8.1, 7.2 Hz, 1H), 6.45 (dt, J = 7.1, 1.2 Hz, 1H), 3.98 (t, J = 5.8 Hz, 2H), 2.46 (t, J = 7.1 Hz, 2H), 2.34 (s, 3H), 1.85−1.65 (m, 4H). ^{13}C {^{1}H} NMR (300 MHz, DMSO-d6; Figure S17) δ 157.3, 130.2, 129.1, 127.8, 127.8, 125.2, 117.0, 115.6, 114.6, 109.8, 109.7, 104.2, 67.3, 51.1, 28.1, 22.0, 9.7. HRMS *m/z* calculated for $C_{19}H_{20}NO_4S$ $[M - Cs]^-$: 358.1119, found 358.1128. IR (neat, cm^{-1}) 3413, 3310, 3064, 3048, 2931, 2860, 1675, 1611, 1535, 1515. Melting point (dec.): 226−232 °C.

Cesium 4-(4-(1-Methyl-3-((1E,3E)-5-((Z)-1-methyl-2-(4-(4-sulfonatobutoxy)phenyl)-3H-indolizin-4-ium-3-ylidene)- penta-1,3-dien-1-yl)indolizin-2-yl)phenoxy)butane-1-sulfonate (**SO_3C5**). To a round-bottom flask equipped with a stir

bar was added cesium 4-(4-(1-methylindolizin-2-yl)phenoxy)butane-1-sulfonate (**3**) (0.50 g, 1.02 mmol) to acetic anhydride (10.2 mL) followed by perchloric acid (0.088 mL, 1.02 mmol) and N-[5-(phenylamino)-2,4 pentadienylidene]aniline monohydrochloride (**4**) (0.15 g, 0.51 mmol). The mixture was then sonicated and stirred until all of the starting material appeared to have been consumed in this first phase of the reaction (about 10 min). When the starting material was no longer visible, the reaction was allowed to stir for another 10 min before the addition of triethylamine (0.17 mL, 1.22 mmol). The reaction mixture quickly turned green and was allowed to stir for 2 h before diethyl ether was added to precipitate the crude product. The precipitate was filtered and rinsed once more with diethyl ether, collecting the solids. The solids were purified via reversed-phase column chromatography beginning with 100% H_2O and gradually transitioning to 40:60 ethanol/H_2O. The water was removed by blowing air over the surface of the solution to avoid heating. The pure product was yielded as a dark green solid (250 mg, 53%). ^{1}H NMR (300 MHz, CD_3OD-d4; Figure S18) δ 8.89 (d, J = 6.8 Hz, 2H), 7.73 (d, J = 8.6 Hz, 2H), 7.66−7.54 (m, 4H), 7.42−7.22 (m, 7H), 7.12 (d, J = 8.5 Hz, 4H), 6.57 (t, J = 13.1 Hz, 2H), 4.16 (t, J = 5.9 Hz, 4H), 2.95 (t, J = 7.0 Hz, 4H), 2.20 (s, 6H), 2.14−1.94 (m, 8H). ^{13}C {^{1}H} NMR (300 MHz, CD_3OD-d4; Figure S19) δ 168.4, 160.9, 144.4, 140.1, 135.6, 132.6, 131.3, 129.7, 127.4, 126.2, 122.5, 121.2, 119.4, 118.0, 116.1, 68.9, 52.4, 29.5, 23.1, 9.3. HRMS *m/z* calculated for $C_{43}H_{44}CsN_2O_8S_2$ $[M + H]^+$: 913.1588, found 913.1606. IR (neat, cm^{-1}): 3375 (br), 3099, 3070, 3033, 2917, 2861, 1651, 1611, 1521, 1508. UV−vis−NIR (DMSO) λ_{max} = 801 nm; UV−vis−NIR (MeOH) λ_{max} = 791 nm; UV−vis−NIR (H2O) λ_{max} = 726 nm; UV−vis−NIR (FBS) λ_{max} = 842 nm. Melting point (dec.): 211−217 °C.

Cesium (Z)-4-(4-(1-Methyl-3-(3-(1-methyl-2-(4-(4- sulfonatobutoxy)phenyl)-3H-indolizin-4-ium-3-ylidene)-2-oxido-4-oxocyclobut-1-en-1-yl)indolizin-2-yl)phenoxy)-butane-1-sulfonate (**SO_3SQ**). To a pressure flask equipped with a stir bar were added cesium 4-(4-(1-methylindolizin-2-yl)phenoxy)- butane-1-sulfonate (**3**) (0.100 g, 0.204 mmol) and 3,4-dihydroxy-1,2-cyclobutanedione (**5**) (0.012 g, 0.102 mmol). The reagents were dissolved in 10 mL methanol and degassed with N_2 for 10 min. The reaction mixture was then heated to 100 °C in an oil bath for 6 h. The reaction mixture was then concentrated, and the solids were further purified via reversed-phase column chromatography beginning with 100% H_2O and gradually transitioning to 40:60 ethanol/H2O. The water was removed by blowing air over the surface of the solution as the product appeared to be sensitive to heat. The pure product was yielded following this step as a metallic red solid in appearance (65 mg, 60%). ^{1}H NMR (300 MHz, CD_3OD-d4; Figure S20) δ 9.76 (d, J = 6.9 Hz, 2H), 7.57 (d, J = 8.7 Hz, 2H), 7.37 (dd, J = 6.8, 1.0 Hz, 2H), 7.23 (d, J = 8.6 Hz, 4H), 7.04−6.95 (m, 6H), 4.13 (t, J = 6.0 Hz, 4H), 2.95 (t, J = 7.0 Hz, 4H), 2.21 (s, 6H), 2.12−1.83 (m, 8H). ^{13}C {^{1}H} NMR (300 MHz, CD3OD-d4; Figure S21) δ 177.8, 166.1, 160.1, 143.2, 138.6, 134.9, 132.9, 128.9, 127.7, 121.0, 119.5, 118.4, 116.1, 114.8, 68.7, 52.5, 29.6, 23.1, 9.5. HRMS *m/z* calculated for $C_{42}H_{39}N_2O_{10}S_2$ [M − 2Cs + 2H]$^-$: 795.2052, found 795.2050. IR (neat, cm^{-1}): 3398 (br), 3068, 3038, 2919, 2864, 1733, 1600, 1570, 1523. UV−vis−NIR (DMSO) λ_{max} = 720 nm; UV−vis−NIR (MeOH) λ_{max} = 704 nm; UV−vis−NIR (H_2O) λ_{max} = 699 nm; UV−vis−NIR (FBS) λ_{max} = 719 nm. Melting point: 240−244 °C.

Photostability Studies. All photostability studies were conducted at a concentration of 1 × 10−6 M to maintain consistency and deter any aggregative effects throughout the photodecomposition process. The samples were irradiated with a white LED lamp providing a spectral range from 400 to 1,100 nm. The experiment was allowed to take place under ambient conditions without any further precautions to remove oxygen from the system. UV−vis−NIR was used to periodically measure the decline in absorption with respect to the λ_{max}. The photostability in methanol was conducted over a period of 24 h, while the photostability in water was conducted over a period of just 6 h as the photodecomposition was observed within a shorter time frame.

CHAPTER V.

CONCLUSION

The need for NIR fluorescent imaging materials that absorb and emit in the NIR region would enable noninvasive, nontoxic, rapid imaging of medical patients and biological specimens, and is thus of paramount importance to modern society. Herein, the synthesis and characterization of a series of novel indolizine cyanine dyes for applications in fluorescence biological imaging is discussed. The indolizine cyanine dyes demonstrate red shifted behavior as the length of the methine bridge increases, and the implementation of electron donating and withdrawing groups atop the phenyl ring displayed little impact on the spectral shift of the dyes. The indolizine donors are substantially red shifted and demonstrate increased stokes shifts compared to the indole donor analogues, all while maintaining a respectable molecular brightness. The synthesis and characterization of a novel donor-acceptor-donor xanthene dye incorporating indolizine heterocycles as donors, deemed rhodindolizine is also discussed. This is the first example of carbon-based donors on a xanthene core with an NIR emissive material, and we report a robust C-H activation coupling to install a range of substituted indolizines varying in electron donating and withdrawing groups. Rhodindolizine is the first xanthene dye to demonstrate far NIR-I absorption and NIR-II emission and lays a foundation for the design of future NIR-II emissive materials. Lastly, the synthesis, characterization, and application of water soluble indolizine cyanines and squaraines is reported. The water-soluble functionality was accessed through the installation of sulfonate groups on the electronically insignificant phenyl ring, allowing for the direct comparison of previously reported indolizine cyanine and indolizine squaraine dyes to

the industry standard ICG inside of an aqueous medium. SO_3C5 suffered from detrimental aggregative behaviors that impeded its absorption and emission in water; however, SO_3SQ demonstrated a record setting quantum yield for its spectral region inside of FBS with a quantum yield of 58.3%. Both dyes demonstrated excellent photostability inside of an aqueous medium, minimal cytotoxicity, and excellent lysosomal uptake.

REFERENCES

1. Shindy, H. A., Fundamentals in the Chemistry of Cyanine Dyes: A Review. *Dyes Pigm.* **2017,** *145*, 505-513.
2. Xue, J.; Li, C.; Xin, L.; Duan, L.; Qiao, J., High-Efficiency and Low Efficiency Roll-Off Near-Infrared Fluorescent OLEDs through Triplet Fusion. *Chem. Sci.* **2016,** *7* (4), 2888-2895.
3. Tuong Ly, K.; Chen-Cheng, R.-W.; Lin, H.-W.; Shiau, Y.-J.; Liu, S.-H.; Chou, P.-T.; Tsao, C.-S.; Huang, Y.-C.; Chi, Y., Near-Infrared Organic Light-Emitting Diodes with Very High External Quantum Efficiency and Radiance. *Nat. Photonics* **2016,** *11* (1), 63-68.
4. Suzuki, H., Organic Light-Emitting Materials and Devices for Optical Communication Technology. *J. Photochem. Photobiol. A* **2004,** *166*, 155-161.
5. Yang, Z.; Sharma, A.; Qi, J.; Peng, X.; Lee, D. Y.; Hu, R.; Lin, D.; Qu, J.; Kim, J. S., Super-Resolution Fluorescent Materials: An Insight into Design and Bioimaging Applications. *Chem. Soc. Rev.* **2016,** *45* (17), 4651-4667.
6. Keereweer, S.; Van Driel, P. B.; Snoeks, T. J.; Kerrebijn, J. D.; Baatenburg de Jong, R. J.; Vahrmeijer, A. L.; Sterenborg, H. J.; Lowik, C. W., Optical Image-Guided Cancer Surgery: Shallenges and Limitations. *Clin. Cancer Res.* **2013,** *19* (14), 3745-3754.
7. Escobedo, J. O.; Rusin, O.; Lim, S.; Strongin, R. M., NIR Dyes for Bioimaging Applications. *Curr. Opin. Chem. Biol.* **2010,** *14* (1), 64-70.
8. Bricks, J. L.; Slominskii, Y. L.; Panas, I. D.; Demchenko, A. P., Fluorescent J-Aggregates of Cyanine Dyes: Basic Research and Applications Review. *Methods Appl. Fluoresc.* **2017,** *6* (1), 012001.
9. Shi, C.; Wu, J. B.; Pan, D., Review on Near-Infrared Heptamethine Cyanine Dyes as Theranostic Agents for Tumor Imaging, Targeting, and Photodynamic Therapy. *J. Biomed. Opt.* **2016,** *21* (5), 050901.
10. Antaris, A. L.; Chen, H.; Cheng, K.; Sun, Y.; Hong, G.; Qu, C.; Diao, S.; Deng, Z.; Hu, X.; Zhang, B.; Zhang, X.; Yaghi, O. K.; Alamparambil, Z. R.; Hong, X.; Cheng, Z.; Dai, H., A Small-Molecule Dye for NIR-II Imaging. *Nat. Mater.* **2016,** *15* (2), 235-242.
11. Peng, X. S., F.; Lu, E.; Wang, Y.; Zhou, W.; Fan, J.; Gao, Y.;, Heptamethine Cyanine Dyes with a Large Stokes Shift and Strong Fluorescence: A Paradigm for Excited-State Intramolecular Charge Transfer. *J. Amer. Chem. Soc.* **2005,** *127*, 4170-4171.
12. Han, J.; Engler, A.; Qi, J.; Tung, C. H., Ultra Pseudo-Stokes Shift Near Infrared Dyes Based on Energy Transfer. *Tetrahedron Lett.* **2013,** *54* (6), 502-505.
13. Smith, A. M.; Mancini, M. C.; Nie, S., Bioimaging: Second Window for in Vivo Imaging. *Nat. Nanotechnol.* **2009,** *4* (11), 710-711.
14. Pham, W.; Cassell, L.; Gillman, A.; Koktysh, D.; Gore, J. C., A Near-Infrared Dye for Multichannel Imaging. *Chem. Commun.* **2008,** (16), 1895-1897.
15. Antaris, A. L.; Chen, H.; Diao, S.; Ma, Z.; Zhang, Z.; Zhu, S.; Wang, J.; Lozano, A. X.; Fan, Q.; Chew, L.; Zhu, M.; Cheng, K.; Hong, X.; Dai, H.; Cheng, Z., A High Quantum Yield Molecule-Protein Complex Fluorophore for Near-Infrared II Imaging. *Nat. Commun.* **2017,** *8*, 15269.
16. Siebrand, W., Radiationless Transitions in Polyatomic Molecules. I. Calculation of Franck—Condon Factors. *J. Chem. Phys.* **1967,** *46* (2), 440-447.
17. Siebrand, W., Radiationless Transitions in Polyatomic Molecules. II. Triplet-Ground-State Transitions in Aromatic Hydrocarbons. *J. Chem. Phys.* **1967,** *47* (7), 2411-2422.
18. Caspar, J. V.; Kober, E. M.; Sullivan, B. P.; Meyer, T. J., Application of the Energy Gap Law to the Decay of Charge-Transfer Excited States. *J. Amer. Chem. Soc.* **1982,** *104* (2), 630-632.
19. Englman, R. J., J., The Energy Gap Law for Radiationless Transitions in Large Molecules *Mol. Phys.* **1970,** *18*, 145-164.
20. McNamara, L. E.; Liyanage, N.; Peddapuram, A.; Murphy, J. S.; Delcamp, J. H.; Hammer, N. I., Donor-Acceptor-Donor Thienopyrazines via Pd-Catalyzed C-H Activation as NIR Fluorescent Materials. *J. Org. Chem.* **2016,** *81* (1), 32-42.
21. Alander, J. T.; Kaartinen, I.; Laakso, A.; Patila, T.; Spillmann, T.; Tuchin, V. V.; Venermo, M.; Valisuo, P., A Review of Indocyanine Green Fluorescent Imaging in Surgery. *Int. J. Biomed. Imaging* **2012,** *2012*, 940585.
22. Alander, J. T.; Villet, O. M.; Pätilä, T.; Kaartinen, I. S.; Lehecka, M.; Nakaguchi, T.; Suzuki, T.; Tuchin, V., Review of Indocyanine Green Imaging in Surgery. In *Fluorescence Imaging for Surgeons: Review of indocyanine Green imaging in Surgery*, Cham, S., Ed. 2015; pp 35-53.

23. Huckaba, A. J.; Giordano, F.; McNamara, L. E.; Dreux, K. M.; Hammer, N. I.; Tschumper, G. S.; Zakeeruddin, S. M.; Grätzel, M.; Nazeeruddin, M. K.; Delcamp, J. H., Indolizine-Based Donors as Organic Sensitizer Components for Dye-Sensitized Solar Cells. *Adv. Energy Mater.* **2015,** *5* (7).
24. Zhang, Y.; Autry, S. A.; McNamara, L. E.; Nguyen, S. T.; Le, N.; Brogdon, P.; Watkins, D. L.; Hammer, N. I.; Delcamp, J. H., Near-Infrared Fluorescent Thienothiadiazole Dyes with Large Stokes Shifts and High Photostability. *J. Org. Chem.* **2017,** *82* (11), 5597-5606.
25. McNamara, L. E.; Rill, T. A.; Huckaba, A. J.; Ganeshraj, V.; Gayton, J.; Nelson, R. A.; Sharpe, E. A.; Dass, A.; Hammer, N. I.; Delcamp, J. H., Indolizine-Squaraines: NIR Fluorescent Materials with Molecularly Engineered Stokes Shifts. *Chem. - Eur. J.* **2017,** *23* (51), 12494-12501.
26. Huckaba, A. J.; Yella, A.; McNamara, L. E.; Steen, A. E.; Murphy, J. S.; Carpenter, C. A.; Puneky, G. D.; Hammer, N. I.; Nazeeruddin, M. K.; Gratzel, M.; Delcamp, J. H., Molecular Design Principles for Near-Infrared Absorbing and Emitting Indolizine Dyes. *Chem. - Eur. J.* **2016,** *22* (43), 15536-15542.
27. Mustroph, H.; Towns, A., Fine Structure in Electronic Spectra of Cyanine Dyes: Are Sub-Bands Largely Determined by a Dominant Vibration or a Collection of Singly Excited Vibrations? *ChemPhysChem* **2018,** *19* (9), 1016-1023.
28. Bai, M.; Achilefu, S., Synthesis and Spectroscopy of Near Infrared Fluorescent Dyes for Investigating Dichromic Fluorescence. *Bioorg. Med. Chem. Lett.* **2011,** *21* (1), 280-284.
29. Qian, G. D., B.; Luo, M.; Yu, D.; Zhan, J.; Zhang, Z.; Ma, D.; Wang. Z. Y., Band Gap Tunable, Donor-Acceptor-Donor Charge-Transfer Heteroquinoid-Based Chromophores: Near Infrared Photoluminescence and Electroluminescence. *Chem. Mater.* **2008,** *20* (19), 6208-6216.
30. Tyler L Dost, M. T. G. M. H., Synthesis and Optical Properties of Pentamethine Cyanine Dyes With Carboxylic Acid Moieties. *Anal. Chem. Insights* **2017,** *12*, 1-6.
31. Zhao, Y.; Truhlar, D. G., The M06 Suite of Density Functionals for Main Group Thermochemistry, Thermochemical Kinetics, Noncovalent Interactions, Excited States, and Transition Elements: Two New Functionals and Systematic Testing of Four M06-Class Functionals and 12 Other Functionals. *Theor. Chem. Acc.* **2007,** *120* (1-3), 215-241.
32. Frisch, M. J.; Trucks, G. W.; Schlegel, H. B.; Scuseria, G. E.; Robb, M. A.; Cheeseman, J. R.; Scalmani, G.; Barone, V.; Petersson, G. A.; Nakatsuji, H.; Li, X.; Caricato, M.; Marenich, A. V.; Bloino, J.; Janesko, B. G.; Gomperts, R.; Mennucci, B.; Hratchian, H. P.; Ortiz, J. V.; Izmaylov, A. F.; Sonnenberg, J. L.; Williams-Young, D.; Ding, F.; Lipparini, F.; Egidi, F.; Goings, J.; Peng, B.; Petrone, A.; Henderson, T.; Ranasinghe, D.; Zakrzewski, V. G.; Gao, J.; Rega, N.; Zheng, G.; Liang, W.; Hada, M.; Ehara, M.; Toyota, K.; Fukuda, R.; Hasegawa, J.; Ishida, M.; Nakajima, T.; Honda, Y.; Kitao, O.; Nakai, H.; Vreven, T.; Throssell, K.; Montgomery, J. A., Jr.; ; Peralta, J. E.; Ogliaro, F.; Bearpark, M. J.; Heyd, J. J.; Brothers, E. N.; Kudin, K. N.; Staroverov, V. N.; Keith, T. A.; Kobayashi, R.; Normand, J.; Raghavachari, K.; Rendell, A. P.; Burant, J. C.; Iyengar, S. S.; Tomasi, J.; Cossi, M.; Millam, J. M.; Klene, M.; Adamo, C.; Cammi, R.; Ochterski, J. W.; Martin, R. L.; Morokuma, K.; Farkas, O.; Foresman, J. B.; Fox, D. J., *Gaussian 16*, Revision A.03 Gaussian, Inc.: Wallingford, CT. **2016**.
33. Marenich, A. V. C., C. J.; Truhlar, D. G., Universal Solvation Model Based on Solute Electron Density and on a Continuum Model of the Solvent Defined by the Bulk Dielectric Constant and Atomic Surface Tensions. *J. Phys. Chem. B* **2009,** *113*, 6378–6396.
34. Cao, J.; Fan, J.; Sun, W.; Guo, Y.; Wu, H.; Peng, X., The Photoprocess Effects of an Amino Group Located at Different Positions Along the Polymethine Chain in Indodicarbocyanine Dyes. *RSC Adv.* **2017,** *7* (49), 30740-30746.
35. Rhys Williams, A. T. W., S. A., Relative Fluorescence Quantum Yields Using a Computer-Controlled Luminescence Spectrometer. *Analyst* **1983,** *108*, 1067-1071.
36. Reindl, S. P., A.; Gong, S. H.; Landthaler, M.; Szeimies, R. M.; Abels, C.; Bamler, W., Quantum Yield of Triplet Formation for Indocyanine Green. *J. Photochem. Photobiol. A* **1997,** *105*, 65-68.
37. Krause, L.; Herbst-Irmer, R.; Sheldrick, G. M.; Stalke, D., Comparison of Silver and Molybdenum Microfocus X-Ray Sources for Single-Crystal Structure Determination. *J. Appl. Crystallogr.* **2015,** *48* (Pt 1), 3-10.
38. *APEX3; Programs for X-Ray Data Collection and Reduction*; Bruker-AXS Inc.: Madison, WI, USA, 2016.
39. Sheldrick, G. M., Crystal Structure Refinement with SHELXL. *Acta Crystallogr., Sect. C: Struct. Chem.* **2015,** *71* (Pt 1), 3-8.
40. Sheldrick, G. M., SHELXT - Integrated Space-Group and Crystal-Structure Determination. *Acta Crystallogr., Sect. A: Found. Adv.* **2015,** *71* (Pt 1), 3-8.

41. Spek, A. L., Platon Squeeze: A Tool for the Calculation of the Disordered Solvent Contribution to the Calculated Structure Factors. *Acta Crystallogr., Sect. C: Struct. Chem.* **2015,** *71* (Pt 1), 9-18.
42. Yao, J. H.; Chi, C.; Wu, J.; Loh, K. P., Bisanthracene bis(dicarboxylic imide)s as Soluble and Stable NIR Dyes. *Chem. - Eur. J.* **2009,** *15* (37), 9299-9302.
43. Yao, L.; Zhang, S.; Wang, R.; Li, W.; Shen, F.; Yang, B.; Ma, Y., Highly Efficient Near-Infrared Organic Light-Emitting Diode Based on a Butterfly-Shaped Donor-Acceptor Chromophore with Strong Solid-State Fluorescence and a Large Proportion of Radiative Excitons. *Angew. Chem. Int. Ed.* **2014,** *53* (8), 2119-2123.
44. Fabian, J.; Nakazumi, H.; Matsuoka, M., Near-Infrared Absorbing Dyes. *Chem. Rev.* **1992,** *92* (6), 1197-1226.
45. Berezin, M. Y. A., S., Fluorescence Lifetime Measurements and Biological Imaging. *Chem. Rev.* **2010,** *110*, 2641–2684.
46. Barlow, S.; Brédas, J.-L.; Getmanenko, Y. A.; Gieseking, R. L.; Hales, J. M.; Kim, H.; Marder, S. R.; Perry, J. W.; Risko, C.; Zhang, Y., Polymethine Materials with Solid-State Third-Order Optical Susceptibilities Suitable for All-Optical Signal-Processing Applications. *Mater. Horiz.* **2014,** *1* (6), 577-581.
47. Detty, M. R. G., S. L.; Wagner, S. J.d, Current Clinical and Preclinical Photosensitizers for Use in Photodynamic Therapy. *J. Med. Chem.* **2004,** *47*, 3897-3915.
48. Qian, G.; Wang, Z. Y., Near-Infrared Organic Compounds and Emerging Applications. *Chem. - Asian J.* **2010,** *5* (5), 1006-1029.
49. Jin, T., Critical Review—Recent Progress in NIR Fluorophores Emitting over 1000 nm for Bioimaging. *ECS J. Solid State Sci. Tech.* **2019,** *8* (1), R9-R13.
50. Guo, Z.; Park, S.; Yoon, J.; Shin, I., Recent Progress in the Development of Near-Infrared Fluorescent Probes for Bioimaging Applications. *Chem. Soc. Rev.* **2014,** *43* (1), 16-29.
51. Sun, Y.; Qu, C.; Chen, H.; He, M.; Tang, C.; Shou, K.; Hong, S.; Yang, M.; Jiang, Y.; Ding, B.; Xiao, Y.; Xing, L.; Hong, X.; Cheng, Z., Novel benzo-bis(1,2,5-thiadiazole) Fluorophores for in Vivo NIR-II Imaging of Cancer. *Chem. Sci.* **2016,** *7* (9), 6203-6207.
52. Zhang, X. D.; Wang, H.; Antaris, A. L.; Li, L.; Diao, S.; Ma, R.; Nguyen, A.; Hong, G.; Ma, Z.; Wang, J.; Zhu, S.; Castellano, J. M.; Wyss-Coray, T.; Liang, Y.; Luo, J.; Dai, H., Traumatic Brain Injury Imaging in the Second Near-Infrared Window with a Molecular Fluorophore. *Adv. Mater.* **2016,** *28* (32), 6872-9.
53. Braun, A. B.; Wehl, I.; Kolmel, D. K.; Schepers, U.; Brase, S., New Polyfluorinated Cyanine Dyes for Selective NIR Staining of Mitochondria. *Chem. - Eur. J.* **2019,** *25* (34), 7998-8002.
54. Gayton, J.; Autry, S. A.; Meador, W.; Parkin, S. R.; Hill, G. A.; Hammer, N. I.; Delcamp, J. H., Indolizine-Cyanine Dyes: Near Infrared Emissive Cyanine Dyes with Increased Stokes Shifts. *J. Org. Chem.* **2019,** *84* (2), 687-697.
55. Gayton, J.; Autry, S.; Fortenberry, R.; Hammer, N.; Delcamp, J., Counter Anion Effect on the Photophysical Properties of Emissive Indolizine-Cyanine Dyes in Solution and Solid State. *Molecules* **2018,** *23* (12), 3051.
56. Davydenko, I.; Barlow, S.; Sharma, R.; Benis, S.; Simon, J.; Allen, T. G.; Cooper, M. W.; Khrustalev, V.; Jucov, E. V.; Castaneda, R.; Ordonez, C.; Li, Z.; Chi, S. H.; Jang, S. H.; Parker, T. C.; Timofeeva, T. V.; Perry, J. W.; Jen, A. K.; Hagan, D. J.; Van Stryland, E. W.; Marder, S. R., Facile Incorporation of $Pd(PPh_3)_2Hal$ Substituents into Polymethines, Merocyanines, and Perylene Diimides as a Means of Suppressing Intermolecular Interactions. *J. Amer. Chem. Soc.* **2016,** *138* (32), 10112-10115.
57. Kuimova, M. K.; Collins, H. A.; Balaz, M.; Dahlstedt, E.; Levitt, J. A.; Sergent, N.; Suhling, K.; Drobizhev, M.; Makarov, N. S.; Rebane, A.; Anderson, H. L.; Phillips, D., Photophysical Properties and Intracellular Imaging of Water-Soluble Porphyrin Dimers for Two-Photon Excited Photodynamic Therapy. *Org. Biomol. Chem.* **2009,** *7* (5), 889-896.
58. Nesterova, I. V. V., V. T.; Pakhomov, S.; Strickler, K. L.; Allen, M. W.; Hammer, R. P.; Soper, S. A., Metallo-Phthalocyanine Near-IR Fluorophores: Oligonucleotide Conjugates and Their Applications in PCR Assays. *Bioconjugate Chem.* **2007,** *18*, 2159–2168.
59. Patwari, J.; Sardar, S.; Liu, B.; Lemmens, P.; Pal, S. K., Three-in-One Approach Towards Efficient Organic Dye-Sensitized Solar Cells: Aggregation Suppression, Panchromatic Absorption and Resonance Energy Transfer. *Beilstein J. Nanotechnol.* **2017,** *8*, 1705-1713.
60. Umezawa, K. C., D.; Suzuki, K., Water-Soluble NIR Fluorescent Probes Based on Squaraine and Their Application for Protein Labeling. *Anal. Sci.* **2008,** *24*.

61. Lambert, C.; Scherpf, T.; Ceymann, H.; Schmiedel, A.; Holzapfel, M., Coupled Oscillators for Tuning Fluorescence Properties of Squaraine Dyes. *J. Amer. Chem. Soc.* **2015,** *137* (10), 3547-3557.
62. Staudinger, C.; Breininger, J.; Klimant, I.; Borisov, S. M., Near-Infrared Fluorescent aza-BODIPY Dyes for Sensing and Imaging of pH from the Neutral to Highly Alkaline Range. *Analyst* **2019,** *144* (7), 2393-2402.
63. Sakamoto, N.; Ikeda, C.; Yamamura, M.; Nabeshima, T., Alpha-Bridged BODIPY Oligomers with Switchable Near-IR Photoproperties by External-Stimuli-Induced Foldamer Formation and Disruption. *Chem. Commun.* **2012,** *48* (40), 4818-20.
64. Yamazawa, S.; Nakashima, M.; Suda, Y.; Nishiyabu, R.; Kubo, Y., 2,3-Naphtho-Fused BODIPYs as Near-Infrared Absorbing Dyes. *J. Org. Chem.* **2016,** *81* (3), 1310-5.
65. Lu, Y.; Sun, Q.; Zhang, Z.; Tang, L.; Shen, X.; Xue, S.; Yang, W., New Frog-Type Dibenzo[a,c][1,2,5]thiadiazolo[3,4-i]phenazine Heterocyclic Derivatives with Aggregation-Enhanced One- and Two-Photon Excitation NIR Fluorescence. *Dyes Pigm.* **2018,** *153*, 233-240.
66. Wang, L. G.; Munhenzva, I.; Sibrian-Vazquez, M.; Escobedo, J. O.; Kitts, C. H.; Fronczek, F. R.; Strongin, R. M., Altering Fundamental Trends in the Emission of Xanthene Dyes. *J. Org. Chem.* **2019,** *84* (5), 2585-2595.
67. Sun, Y. Q.; Liu, J.; Lv, X.; Liu, Y.; Zhao, Y.; Guo, W., Rhodamine-Inspired Far-Red to Near-Infrared Dyes and their Application as Fluorescence Probes. *Angew. Chem. Int. Ed.* **2012,** *51* (31), 7634-7636.
68. Myochin, T.; Hanaoka, K.; Iwaki, S.; Ueno, T.; Komatsu, T.; Terai, T.; Nagano, T.; Urano, Y., Development of a Series of Near-Infrared Dark Quenchers Based on Si-Rhodamines and their Application to Fluorescent Probes. *J. Amer. Chem. Soc.* **2015,** *137* (14), 4759-4765.
69. Davies, K. S.; Linder, M. K.; Kryman, M. W.; Detty, M. R., Extended Rhodamine Photosensitizers for Photodynamic Therapy of Cancer Cells. *Bioorg. Med. Chem.* **2016,** *24* (17), 3908-3917.
70. Fukazawa, A.; Suda, S.; Taki, M.; Yamaguchi, E.; Grzybowski, M.; Sato, Y.; Higashiyama, T.; Yamaguchi, S., Phospha-Fluorescein: a Red-Emissive Fluorescein Analogue with High Photobleaching Resistance. *Chem. Commun.* **2016,** *52* (6), 1120-1123.
71. Fu, M.; Xiao, Y.; Qian, X.; Zhao, D.; Xu, Y., A Design Concept of Long-Wavelength Fluorescent Analogs of Rhodamine Dyes: Replacement of Oxygen with Silicon Atom. *Chem. Commun.* **2008,** (15), 1780-2.
72. Best, Q. A.; Sattenapally, N.; Dyer, D. J.; Scott, C. N.; McCarroll, M. E., pH-Dependent Si-Fluorescein Hypochlorous acid Fluorescent Probe: Spirocycle Ring-Opening and Excess Hypochlorous Acid-Induced Chlorination. *J. Amer. Chem. Soc.* **2013,** *135* (36), 13365-13370.
73. Butkevich, A. N.; Mitronova, G. Y.; Sidenstein, S. C.; Klocke, J. L.; Kamin, D.; Meineke, D. N.; D'Este, E.; Kraemer, P. T.; Danzl, J. G.; Belov, V. N.; Hell, S. W., Fluorescent Rhodamines and Fluorogenic Carbopyronines for Super-Resolution STED Microscopy in Living Cells. *Angew. Chem. Int. Ed.* **2016,** *55* (10), 3290-4.
74. Kushida, Y.; Nagano, T.; Hanaoka, K., Silicon-Substituted Xanthene Dyes and their Applications in Bioimaging. *Analyst* **2015,** *140* (3), 685-95.
75. Yuan, L.; Lin, W.; Zhao, S.; Gao, W.; Chen, B.; He, L.; Zhu, S., A Unique Approach to Development of Near-Infrared Fluorescent Sensors for in Vivo Imaging. *J. Amer. Chem. Soc.* **2012,** *134* (32), 13510-13523.
76. Yuan, L.; Lin, W.; Yang, Y.; Chen, H., A Unique Class of Near-Infrared Functional Fluorescent Dyes with Carboxylic-Acid-Modulated Fluorescence ON/OFF Switching: Rational Design, Synthesis, Optical Properties, Theoretical Calculations, and Applications for Fluorescence Imaging in Living Animals. *J. Amer. Chem. Soc.* **2012,** *134* (2), 1200-1211.
77. Cosco, E. D.; Caram, J. R.; Bruns, O. T.; Franke, D.; Day, R. A.; Farr, E. P.; Bawendi, M. G.; Sletten, E. M., Flavylium Polymethine Fluorophores for Near- and Shortwave Infrared Imaging. *Angew. Chem. Int. Ed.* **2017,** *56* (42), 13126-13129.
78. Wang, W.; Ma, Z.; Zhu, S.; Wan, H.; Yue, J.; Ma, H.; Ma, R.; Yang, Q.; Wang, Z.; Li, Q.; Qian, Y.; Yue, C.; Wang, Y.; Fan, L.; Zhong, Y.; Zhou, Y.; Gao, H.; Ruan, J.; Hu, Z.; Liang, Y.; Dai, H., Molecular Cancer Imaging in the Second Near-Infrared Window Using a Renal-Excreted NIR-II Fluorophore-Peptide Probe. *Adv. Mater.* **2018,** *30* (22), e1800106.
79. Zhao, J.; Zhong, D.; Zhou, S., NIR-I-to-NIR-II Fluorescent Nanomaterials for Biomedical Imaging and Cancer Therapy. *J. Mater. Chem. B* **2018,** *6* (3), 349-365.

80. Zebibula, A.; Alifu, N.; Xia, L.; Sun, C.; Yu, X.; Xue, D.; Liu, L.; Li, G.; Qian, J., Ultrastable and Biocompatible NIR-II Quantum Dots for Functional Bioimaging. *Adv. Funct. Mater.* **2018,** *28* (9).
81. Ma, Z.; Wan, H.; Wang, W.; Zhang, X.; Uno, T.; Yang, Q.; Yue, J.; Gao, H.; Zhong, Y.; Tian, Y.; Sun, Q.; Liang, Y.; Dai, H., A Theranostic Agent for Cancer Therapy and Imaging in the Second Near-Infrared Window. *Nano. Res.* **2019,** *12*, 273-279.
82. Hong, G.; Antaris, A. L.; Dai, H., Near-Infrared Fluorophores for Biomedical Imaging. *Nat. Biomed. Eng.* **2017,** *1* (1).
83. Zhang, Y.; Zhang, Y.; Hong, G.; He, W.; Zhou, K.; Yang, K.; Li, F.; Chen, G.; Liu, Z.; Dai, H.; Wang, Q., Biodistribution, Pharmacokinetics and Toxicology of Ag2S Near-Infrared Quantum Dots in Mice. *Biomaterials* **2013,** *34* (14), 3639-46.
84. Yang, Q.; Ma, Z.; Wang, H.; Zhou, B.; Zhu, S.; Zhong, Y.; Wang, J.; Wan, H.; Antaris, A.; Ma, R.; Zhang, X.; Yang, J.; Zhang, X.; Sun, H.; Liu, W.; Liang, Y.; Dai, H., Rational Design of Molecular Fluorophores for Biological Imaging in the NIR-II Window. *Adv. Mater.* **2017,** *29* (12).
85. Patalag, L. J.; Loch, M.; Jones, P. G.; Werz, D. B., Exploring the pi-System of the (Aza-)BOIMPY Scaffold: Electron-Rich Pyrrole Moieties Working in Concert with Electron-Depleted Meso-Positions. *J. Org. Chem.* **2019,** *84* (12), 7804-7814.
86. Kinnibrugh, T. L. S., S.; Getmanenko, Y. A.; Coropceanu, V.; Porter III, W. W.; Timofeeva, T. V.; Matzger, A. J.; Bre´das, J.; Marder, S. R.; Barlow, S., Dipolar Second-Order Nonlinear Optical Chromophores Containing Ferrocene, Octamethylferrocene, and Ruthenocene Donors and Strong π-Acceptors: Crystal Structures and Comparison of π-Donor Strengths. *Organometallics* **2009,** *28*, 1350–1357.
87. Cheema, H.; Baumann, A.; Loya, E. K.; Brogdon, P.; McNamara, L. E.; Carpenter, C. A.; Hammer, N. I.; Mathew, S.; Risko, C.; Delcamp, J. H., Near-Infrared-Absorbing Indolizine-Porphyrin Push-Pull Dye for Dye-Sensitized Solar Cells. *ACS Appl. Mater. Interfaces* **2019,** *11* (18), 16474-16489.
88. Huckaba, A. J.; Yella, A.; Brogdon, P.; Scott Murphy, J.; Nazeeruddin, M. K.; Gratzel, M.; Delcamp, J. H., A Low Recombination Rate Indolizine Sensitizer for Dye-Sensitized Solar Cells. *Chem. Commun.* **2016,** *52* (54), 8424-8427.
89. Brogdon, P.; Giordano, F.; Puneky, G. A.; Dass, A.; Zakeeruddin, S. M.; Nazeeruddin, M. K.; Gratzel, M.; Tschumper, G. S.; Delcamp, J. H., A Computational and Experimental Study of Thieno[3,4-b]thiophene as a Proaromatic pi-Bridge in Dye-Sensitized Solar Cells. *Chem. - Eur. J.* **2016,** *22* (2), 694-703.
90. Chen, X.; Engle, K. M.; Wang, D. H.; Yu, J. Q., Palladium(II)-Catalyzed C-H Activation/C-C Cross-Coupling Reactions: Versatility and Practicality. *Angew. Chem. Int. Ed.* **2009,** *48* (28), 5094-5115.
91. Daugulis, O. D., H.; Shabashov, D., Palladium- and Copper-Catalyzed Arylation of Carbon-Hydrogen Bonds. *Acc. Chem. Res.* **2009,** *42* (8), 1074-1086.
92. Davies, H. M. L.; Morton, D., Collective Approach to Advancing C-H Functionalization. *ACS Cent. Sci.* **2017,** *3* (9), 936-943.
93. Verbelen, B.; Boodts, S.; Hofkens, J.; Boens, N.; Dehaen, W., Radical C-H Arylation of the BODIPY Core with Aryldiazonium Salts: Synthesis of Highly Fluorescent Red-Shifted Dyes. *Angew. Chem. Int. Ed.* **2015,** *54* (15), 4612-4616.
94. Verbelen, B.; Cunha Dias Rezende, L.; Boodts, S.; Jacobs, J.; Van Meervelt, L.; Hofkens, J.; Dehaen, W., Radical C-H Alkylation of BODIPY Dyes Using Potassium Trifluoroborates or Boronic Acids. *Chem. - Eur. J.* **2015,** *21* (36), 12667-12675.
95. Nandakumar, A. P., P. T., Tetrasubstituted Olefinic Xanthene Dyes: Synthesis via Pd-Catalyzed 6-exo-dig Cyclization/C-H Activation of 2-Bromobenzyl-N-propargyl mines and Solid State Fluorescence Properties. *Org. Lett.* **2013,** *15*, 382–385.
96. Koszarna, B.; Matczak, R.; Krzeszewski, M.; Vakuliuk, O.; Klajn, J.; Tasior, M.; Nowicki, J. T.; Gryko, D. T., Direct Arylation of Electron-Poor Indolizines. *Tetrahedron* **2014,** *70* (2), 225-231.
97. Lie´gault, B. L., D.; Caron, L.; Vlassova, A.; Fagnou, K., Establishment of Broadly Applicable Reaction Conditions for the Palladium-Catalyzed Direct Arylation of Heteroatom-Containing Aromatic Compounds. *J. Org. Chem.* **2009,** *74*, 1826–1834.
98. Grimm, J. B. L., L. D., Synthesis of Rhodamines from Fluoresceins Using Pd-Catalyzed C-N Cross-Coupling. *Org. Lett.* **2011,** *13*, 6354–6357.
99. Roger, J.; Doucet, H., Aryl Triflates: Useful Coupling Partners for the Direct Arylation of Heteroaryl Derivatives via Pd-Catalyzed C-H Activation-Functionalization. *Org. Biomol. Chem.* **2008,** *6* (1), 169-174.
100. Wakioka, M.; Kitano, Y.; Ozawa, F., A Highly Efficient Catalytic System for Polycondensation of 2,7-Dibromo-9,9-dioctylfluorene and 1,2,4,5-Tetrafluorobenzene via Direct Arylation. *Macromolecules* **2013,** *46* (2), 370-374.

101. Woodroofe, C. C.; Lim, M. H.; Bu, W.; Lippard, S. J., Synthesis of Isomerically Pure Carboxylate- and Sulfonate-Substituted Xanthene Fluorophores. *Tetrahedron* **2005,** *61* (12), 3097-3105.
102. Best, Q. A.; Liu, C.; Van Hoveln, P. D.; McCarroll, M. E.; Scott, C. N., Anilinomethylrhodamines: pH Sensitive Probes with Tunable Photophysical Properties by Substituent Effect. *J. Org. Chem.* **2013,** *78* (20), 10134-10143.
103. Luo, S.; Zhang, E.; Su, Y.; Cheng, T.; Shi, C., A Review of NIR Dyes in Cancer Targeting and Imaging. *Biomaterials* **2011,** *32* (29), 7127-38.
104. Li, X.; Gao, X.; Shi, W.; Ma, H., Design Strategies for Water-Soluble Small Molecular Chromogenic and Fluorogenic Probes. *Chem. Rev.* **2014,** *114* (1), 590-659.
105. Owens, E. A.; Henary, M.; El Fakhri, G.; Choi, H. S., Tissue-Specific Near-Infrared Fluorescence Imaging. *Acc. Chem. Res.* **2016,** *49* (9), 1731-40.
106. Zhu, S.; Tian, R.; Antaris, A. L.; Chen, X.; Dai, H., Near-Infrared-II Molecular Dyes for Cancer Imaging and Surgery. *Adv. Mater.* **2019,** *31* (24), e1900321.
107. Sun, X.; Zhuang, B.; Zhang, M.; Jiang, H.; Jin, Y., Intratumorally Injected Photothermal Agent-Loaded Photodynamic Nanocarriers for Ablation of Orthotopic Melanoma and Breast Cancer. *ACS Biomater. Sci. Eng.* **2019,** *5* (2), 724-739.
108. Hales, J. M.; Barlow, S.; Kim, H.; Mukhopadhyay, S.; Brédas, J.-L.; Perry, J. W.; Marder, S. R., Design of Organic Chromophores for All-Optical Signal Processing Applications. *Chem. Mater.* **2013,** *26* (1), 549-560.
109. Samuel, I. D. W. T., G. A., Organic Semiconductor Lasers. *Chem. Rev.* **2007,** *107*, 1272-1295.
110. Ibrahim-Ouali, M.; Dumur, F., Recent Advances on Metal-Based Near-Infrared and Infrared Emitting OLEDs. *Molecules* **2019,** *24* (7).
111. Wang, J.; Lv, F.; Liu, L.; Ma, Y.; Wang, S., Strategies to Design Conjugated Polymer Based Materials for Biological Sensing and Imaging. *Coord. Chem. Rev.* **2018,** *354*, 135-154.
112. Ilina, K.; MacCuaig, W. M.; Laramie, M.; Jeouty, J. N.; McNally, L. R.; Henary, M., Squaraine Dyes: Molecular Design for Different Applications and Remaining Challenges. *Bioconjug. Chem.* **2020,** *31* (2), 194-213.
113. Gao, F. P.; Lin, Y. X.; Li, L. L.; Liu, Y.; Mayerhoffer, U.; Spenst, P.; Su, J. G.; Li, J. Y.; Wurthner, F.; Wang, H., Supramolecular adducts of squaraine and protein for noninvasive tumor imaging and photothermal therapy in vivo. *Biomaterials* **2014,** *35* (3), 1004-14.
114. Lerchenberger, M.; Gundogar, U.; Al Arabi, N.; Gallwas, J. K. S.; Stepp, H.; Hallfeldt, K. K. J.; Ladurner, R., Indocyanine Green Fluorescence Imaging During Partial Adrenalectomy. *Surg. Endosc.* **2020,** *34* (5), 2050-2055.
115. Rathnamalala, C. S. L.; Gayton, J. N.; Dorris, A. L.; Autry, S. A.; Meador, W.; Hammer, N. I.; Delcamp, J. H.; Scott, C. N., Donor-Acceptor-Donor NIR II Emissive Rhodindolizine Dye Synthesized by C-H Bond Functionalization. *J. Org. Chem.* **2019,** *84* (20), 13186-13193.
116. Li, B.; Lu, L.; Zhao, M.; Lei, Z.; Zhang, F., An Efficient 1064 nm NIR-II Excitation Fluorescent Molecular Dye for Deep-Tissue High-Resolution Dynamic Bioimaging. *Angew. Chem. Int. Ed.* **2018,** *57* (25), 7483-7487.
117. Rotermund, F. W., R.; Penzkofer A., J-aggregation and Disaggregation of Indocyanine Green in Water. *Chem. Phys* **1997,** *220*, 385-392.
118. Rüttger, F.; Mindt, S.; Golz, C.; Alcarazo, M.; John, M., Isomerization and Dimerization of Indocyanine Green and a Related Heptamethine Dye. *Chem. - Eur. J.* **2019,** *2019* (30), 4791-4796.

APPENDIX

APPENDIX A. CHAPTER 2 SUPPLEMENTAL INFORMATION

Table S1. Dielectric constant and dipole values for solvents used in photophysical studies

Solvent	Dielectric constant	Dipole (D)
DMSO	46.7	3.96
MeCN	37.5	3.92
DMF	38	3.82
Acetone	21	2.88
Water	80	1.85
Ethyl Acetate	6.0	1.78
THF	7.5	1.75
Methanol	33	1.70
Ethanol	24.6	1.69
Dichloromethane	9.1	1.60
Chloroform	4.8	1.04
Toluene	2.4	0.36

Table S2. The solubility of each dye in the series and ICG in various solvents where (PS) represents partial solubility and (IS) represents insolubility

	Solvent Solubility (mg/mL)													
Dye	MeCN	2:1 MeCN:H_2O	1:1 MeCN:H_2O	10:1 MeCN:H_2O	MeOH	Acetone	Toluene	CHCl3	DMF	EtOH	EA	THF	DMSO	DCM
C1	0.58	1.79	5.00	0.95	1.86	2.38	0.07	0.54	7.00	1.25	0.95	0.90	6.50	2.10
C3	1.00	1.47	0.37	1.22	0.35	0.85	0.02 (PS)	0.60	6.75	0.05 (PS)	0.06 (PS)	0.03 (PS)	5.50	0.50
C5	1.89	0.86	0.43	2.17	0.32	2.45	0.04 (PS)	1.87	8.00	0.18	0.04 (PS)	0.03 (PS)	4.00	2.80
PhOMeIndz-C5	2.78	1.30	0.43	4.00	0.29	1.25	(IS)	3.43	10.5	0.05 (PS)	0.05 (PS)	0.11	10.5	2.50
PhCNIndz-C5	0.48	0.18	0.15	0.70	0.15	0.22	0.04 (PS)	0.28	7.25	0.04 (PS)	0.04 (PS)	0.04 (PS)	8.00	0.30
PhIndzOMe-C5	2.50	0.55	0.20	2.75	0.13	0.22	0.02 (PS)	0.50	5.50	0.03 (PS)	0.03 (PS)	0.03 (PS)	5.50	1.20
ICG	0.04 (PS)	8.50	9.50	1.80	10.0	(IS)	(IS)	(IS)	1.40	0.05 (PS)	(IS)	(IS)	18.0	(IS)

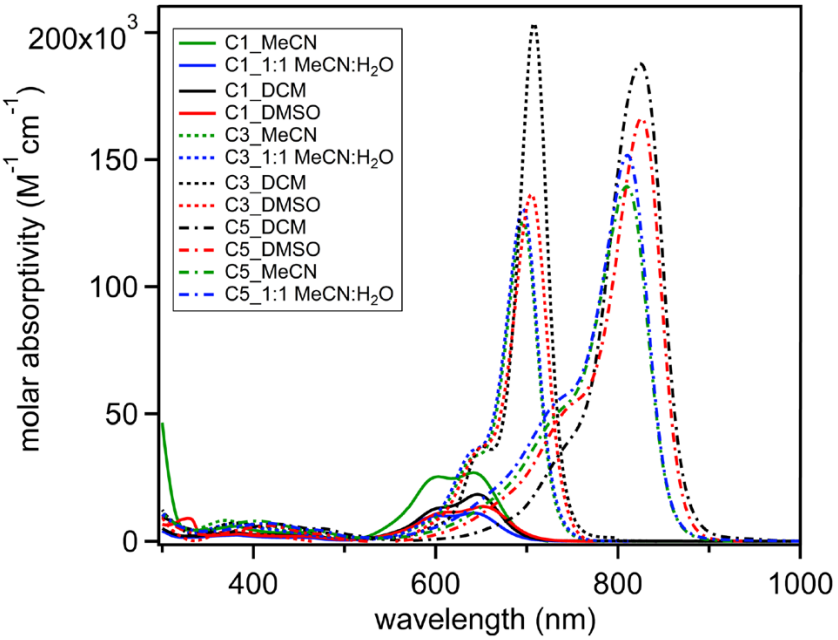

Figure S1. UV-Vis-NIR molar absorptivity of **C1**, **C3**, and **C5** in various solvents with window expanded from 300-1000 nm.

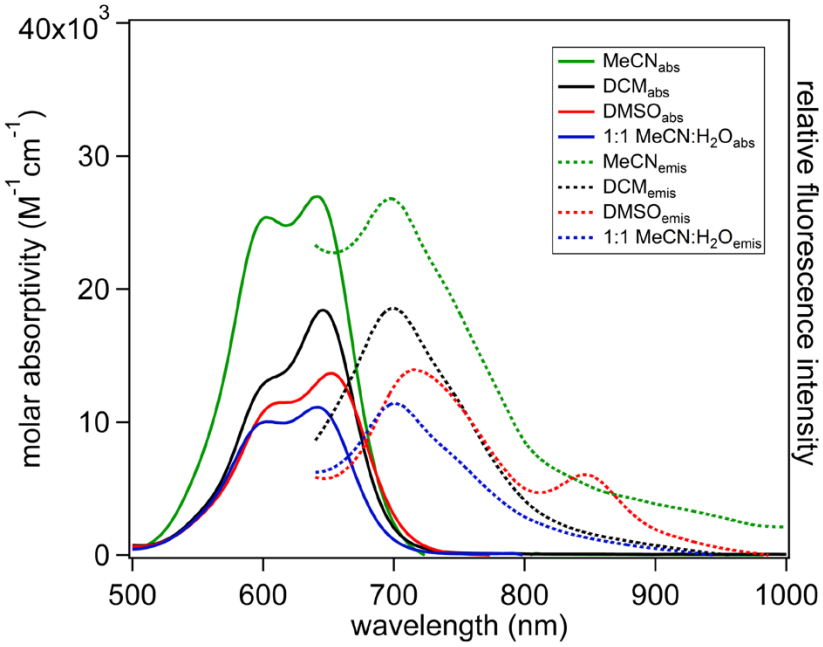

Figure S2. C1 UV-Vis-NIR molar absorptivity (solid lines) and normalized emission spectrum (dotted lines) in 4 solvents.

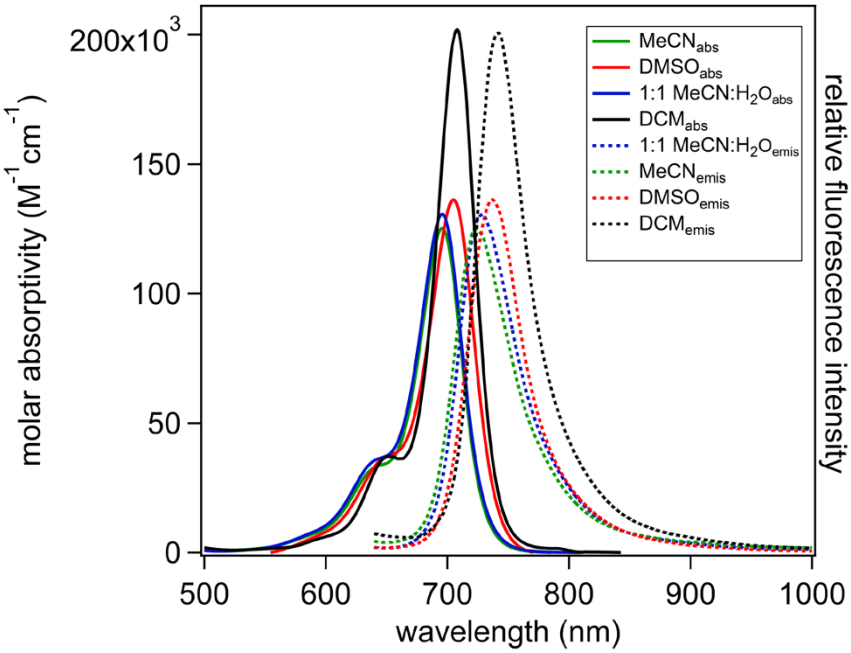

Figure S3. C3 UV-Vis-NIR molar absorptivity (solid lines) and normalized emission spectrum (dotted lines) in 4 solvents.

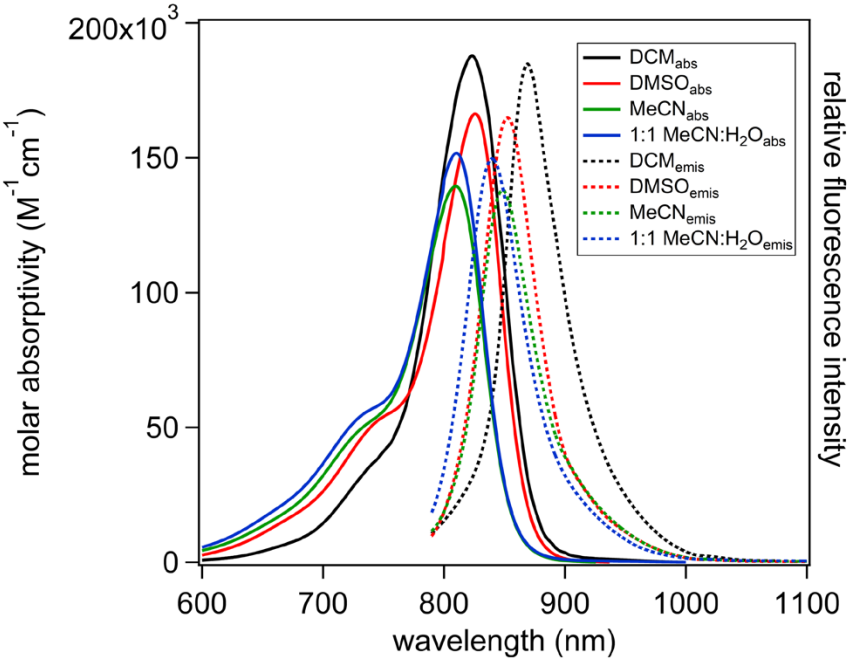

Figure S4. C5 UV-Vis-NIR molar absorptivity (solid lines) and normalized emission spectrum (dotted lines) in 4 solvents.

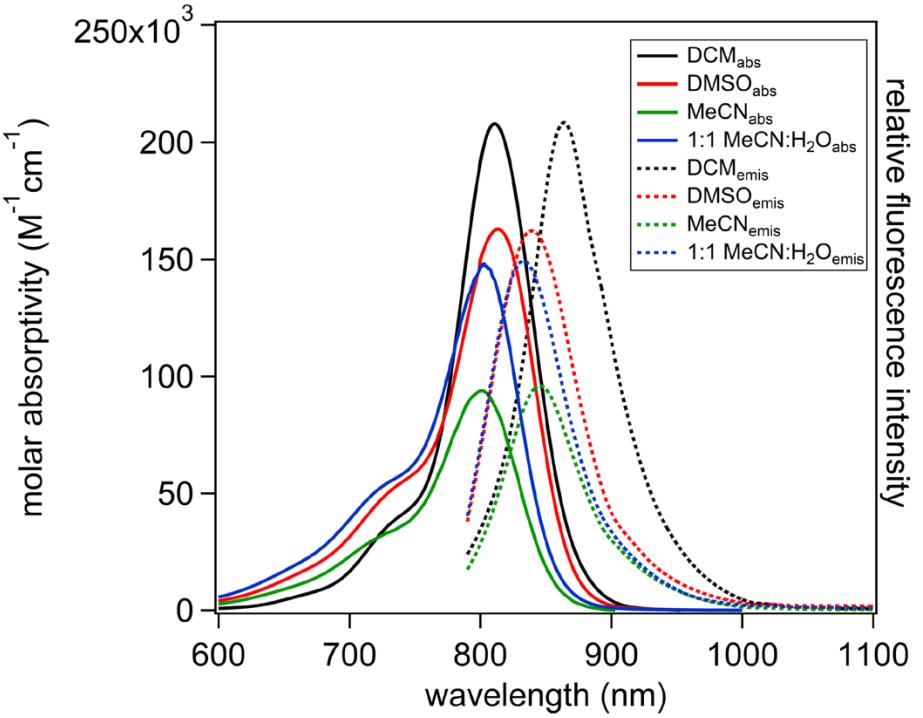

Figure S5. PhOMe-C5 UV-Vis-NIR molar absorptivity (solid lines) and normalized emission spectrum (dotted lines) in 4 solvents.

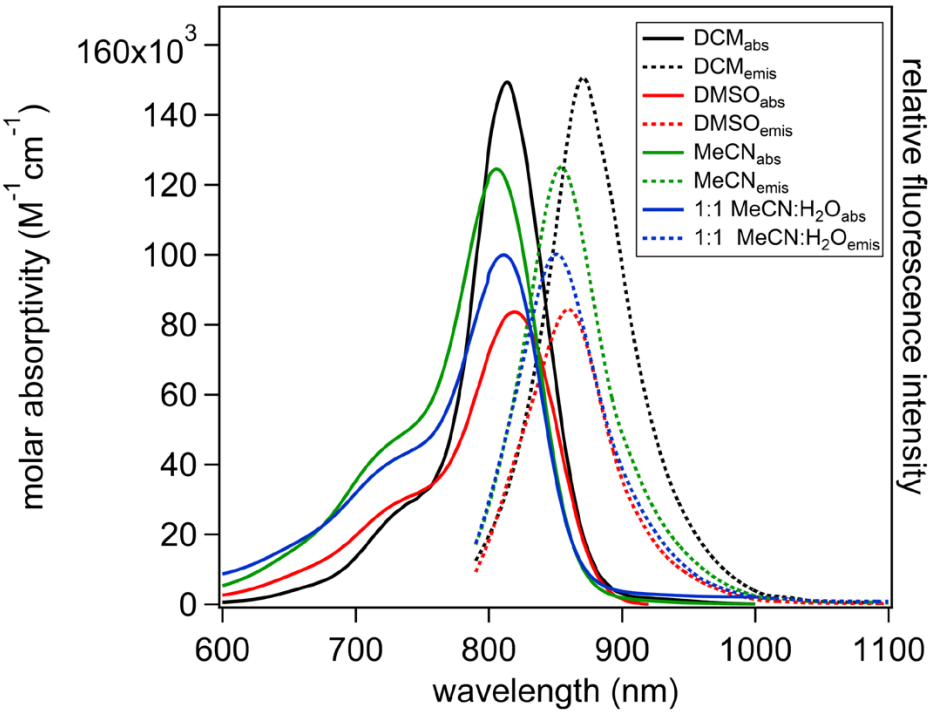

Figure S6. PhCN-C5 UV-Vis-NIR molar absorptivity (solid lines) and normalized emission spectrum (dotted lines) in 4 solvents.

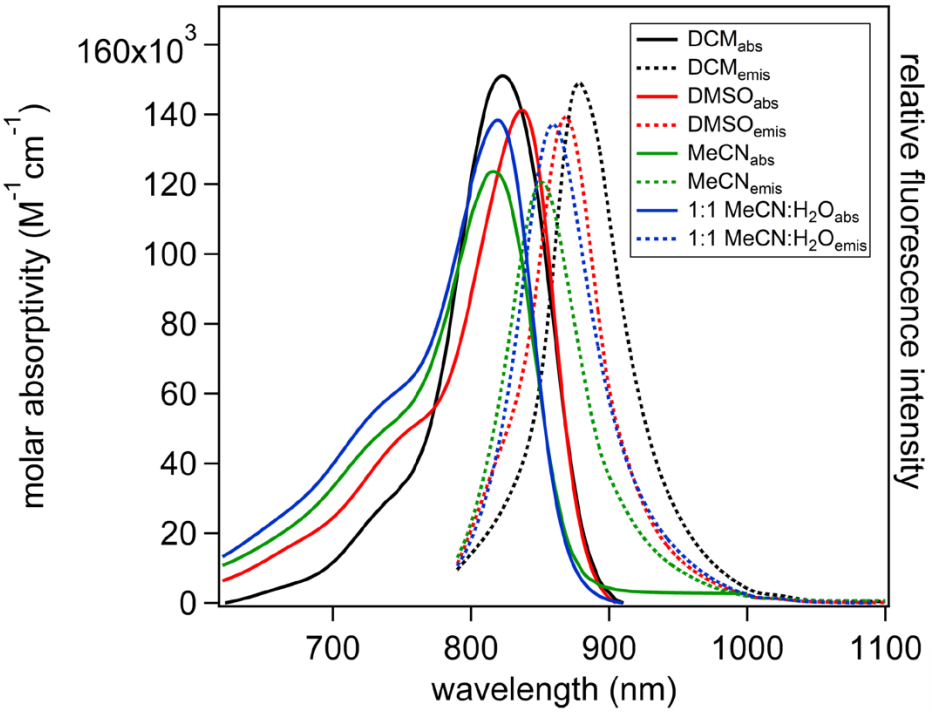

Figure S7. IndzOMe-C5 UV-Vis-NIR molar absorptivity (solid lines) and normalized emission spectrum (dotted lines) in 4 solvents.

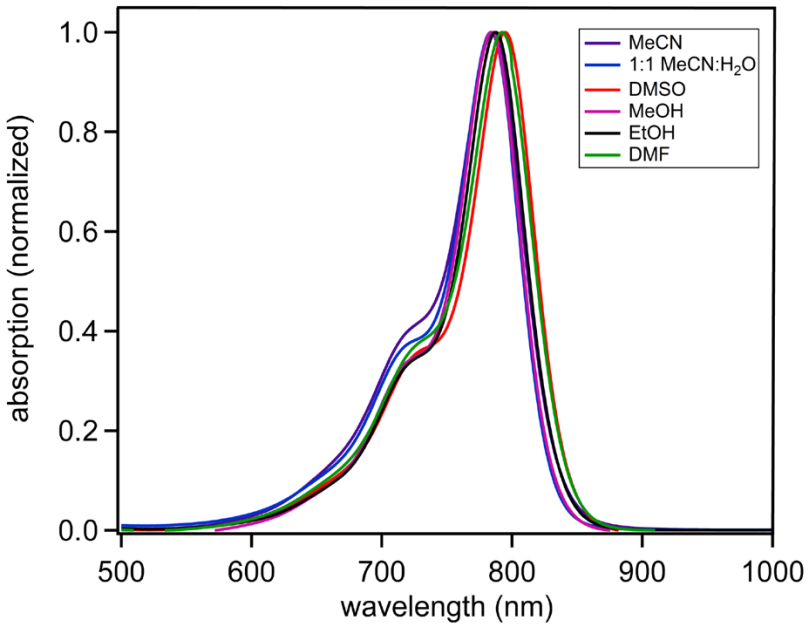

Figure S8. ICG UV-Vis-NIR absorbance in several solvents.

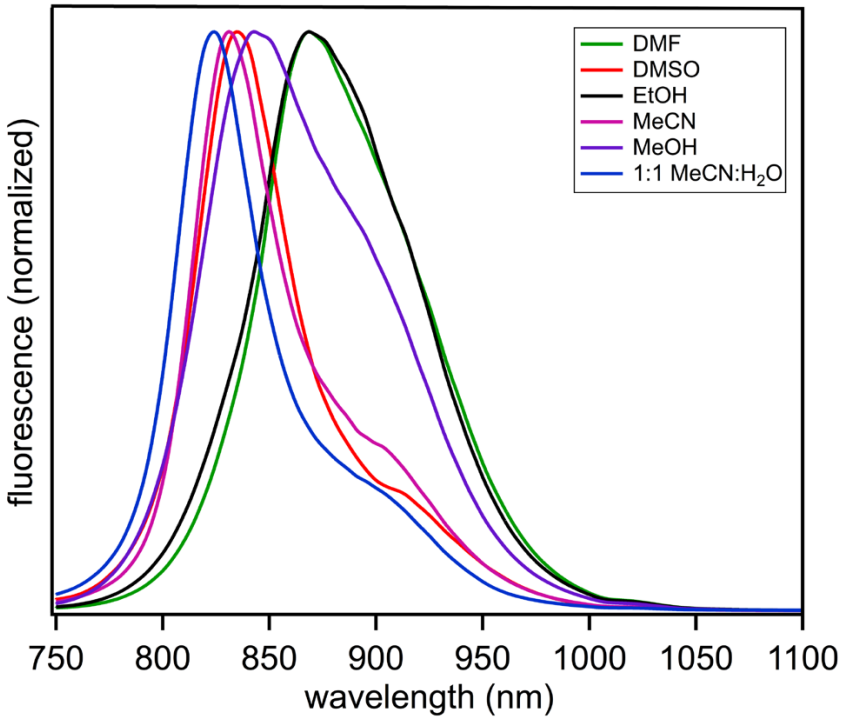

Figure S9. ICG normalized emission spectrum in several solvents.

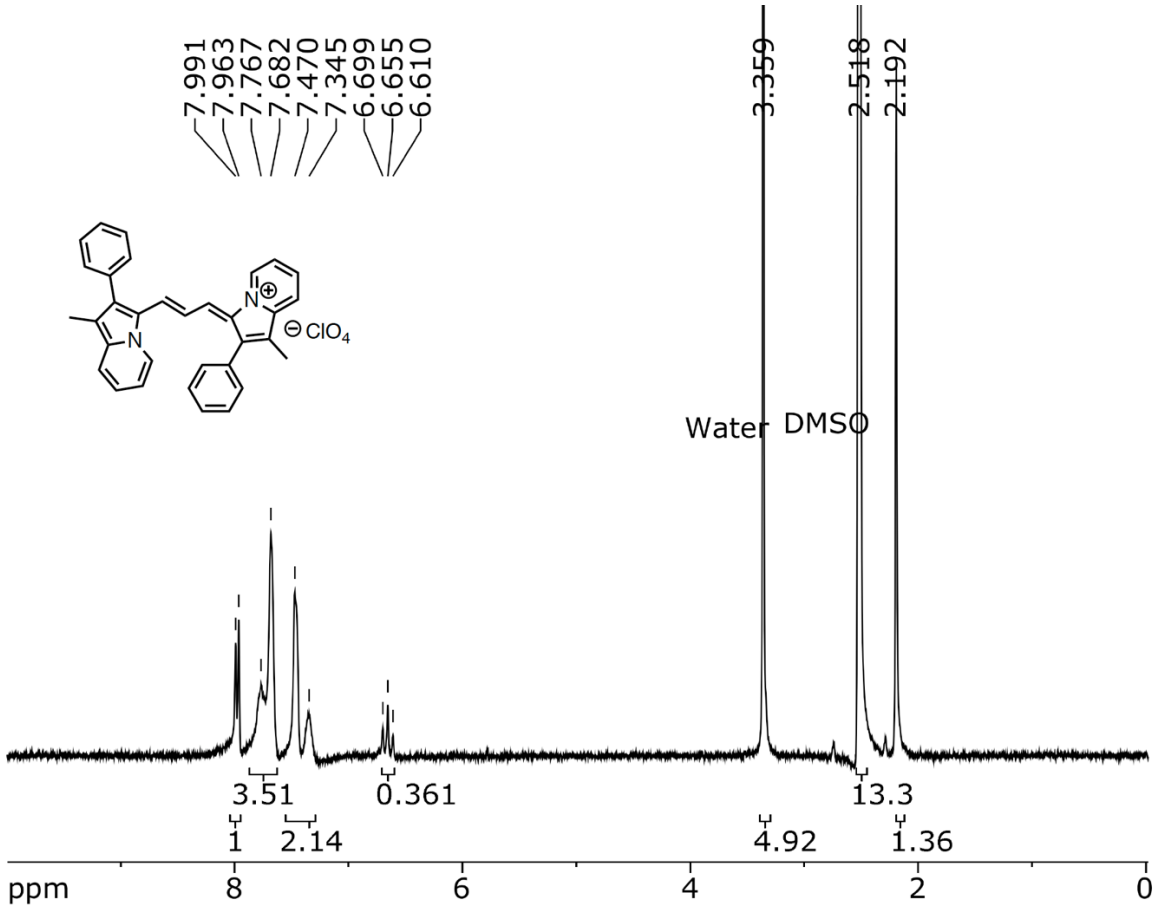

Figure S10. ^{1}H NMR (300 MHz, DMSO-d6) of **C1**.

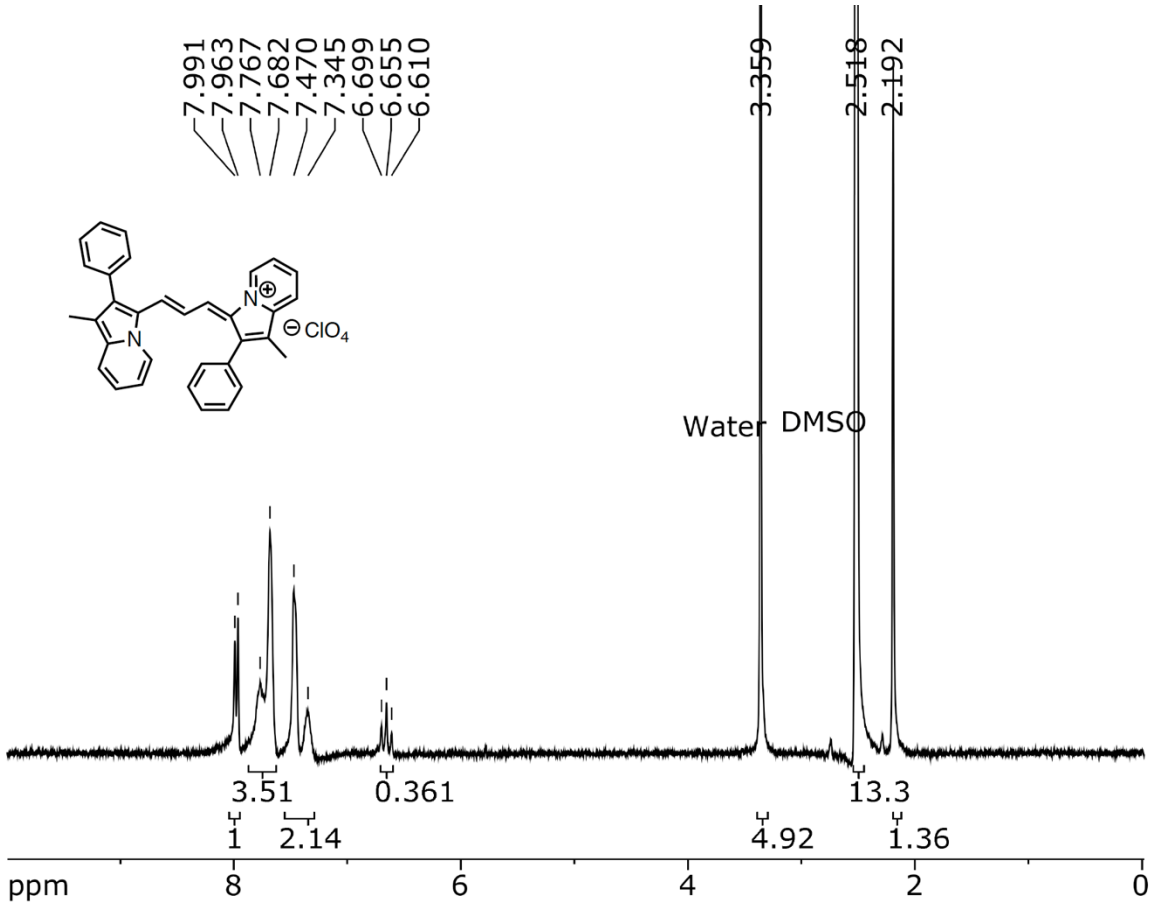

Figure S11. ^{1}H NMR (300 MHz, DMSO-d6) of **C3**.

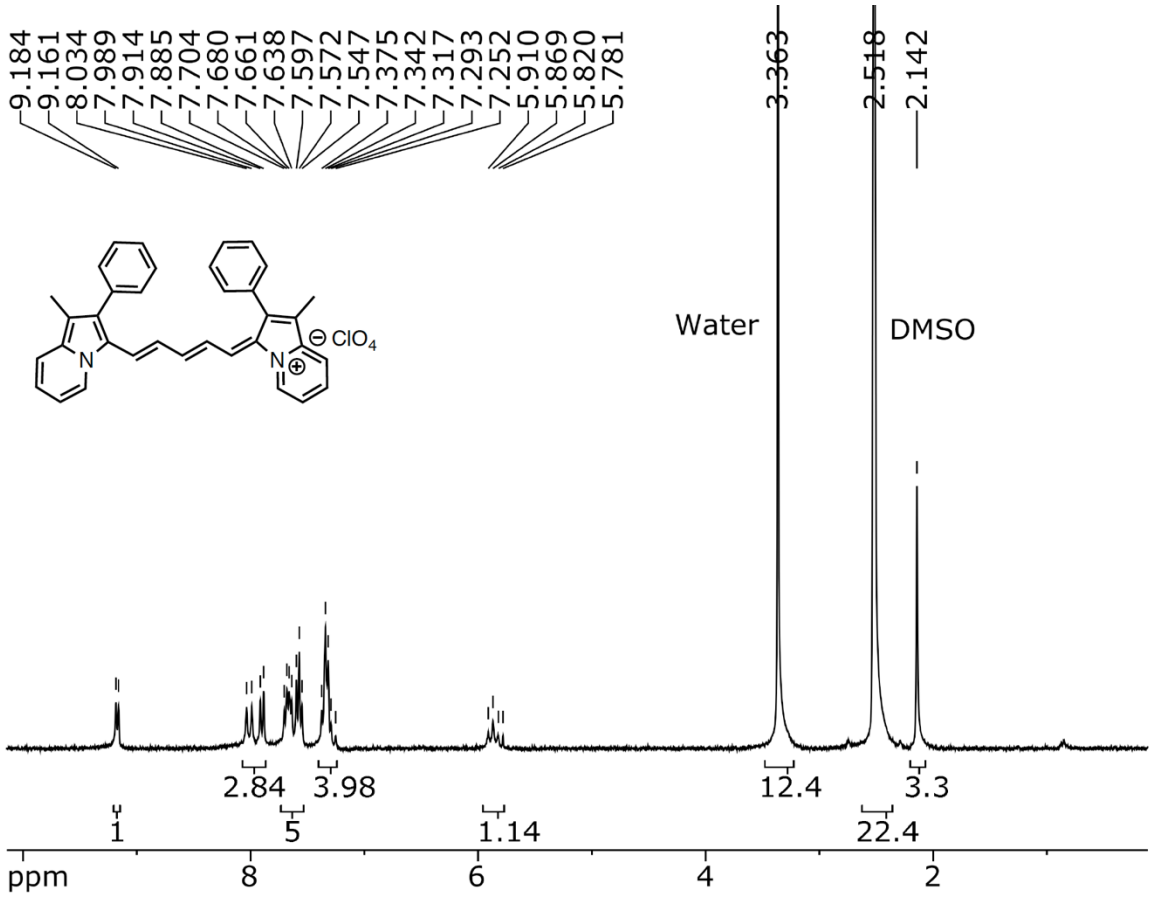

Figure S12. [1]H NMR (300 MHz, DMSO-d6) of **C5**.

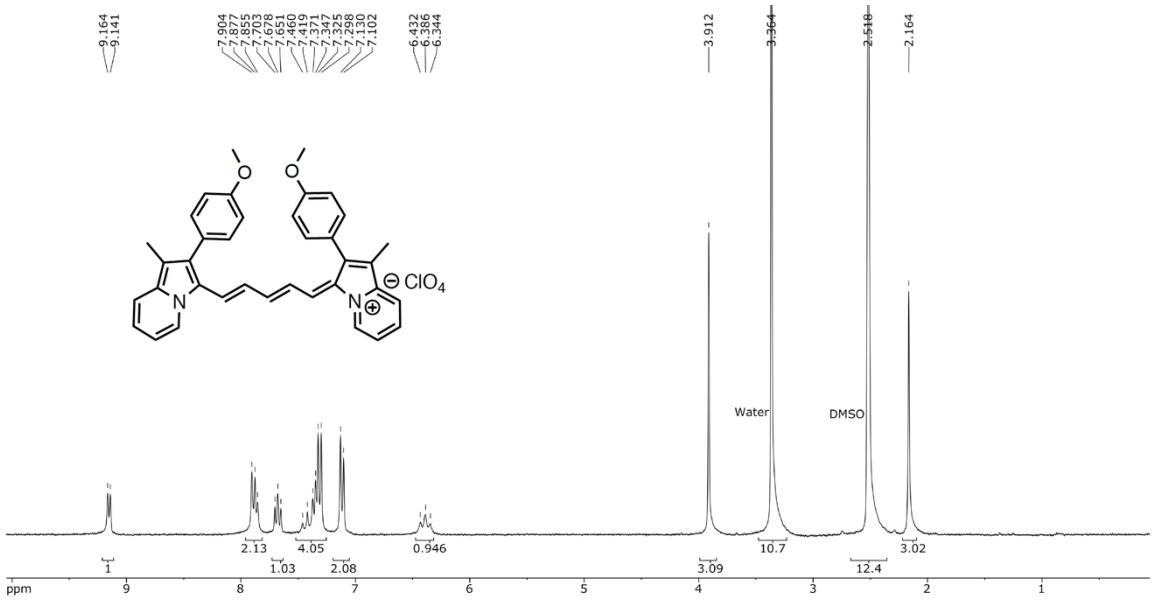

Figure S13. ^{1}H NMR (300 MHz, DMSO-d6) of **PhOMe-C5**.

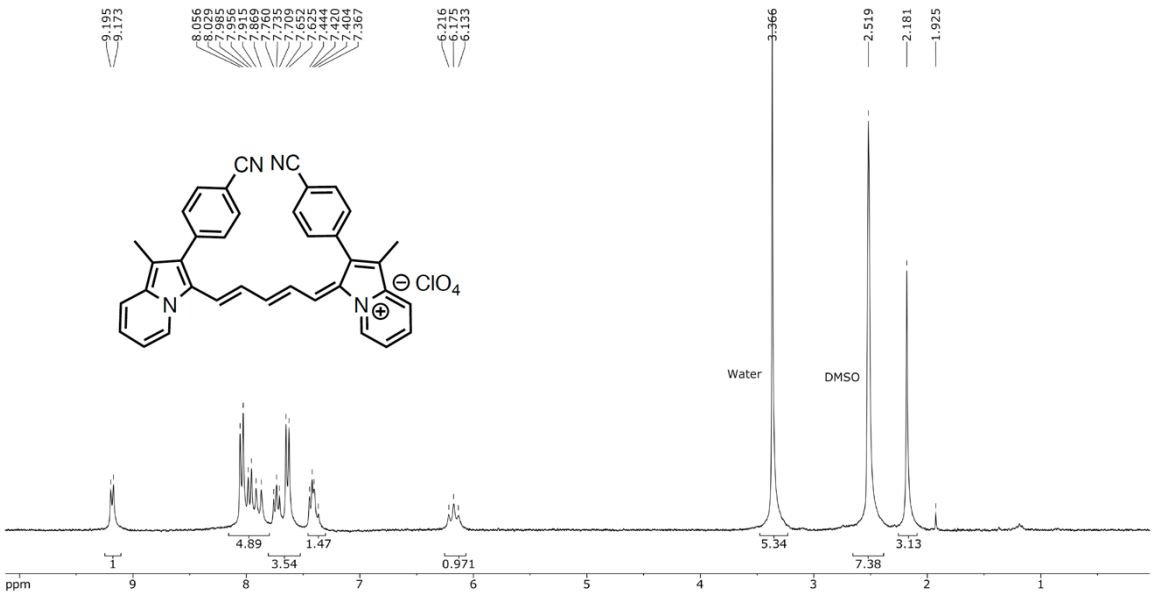

Figure S14. ^{1}H NMR (300 MHz, DMSO-d6) of **PhCN-C5**.

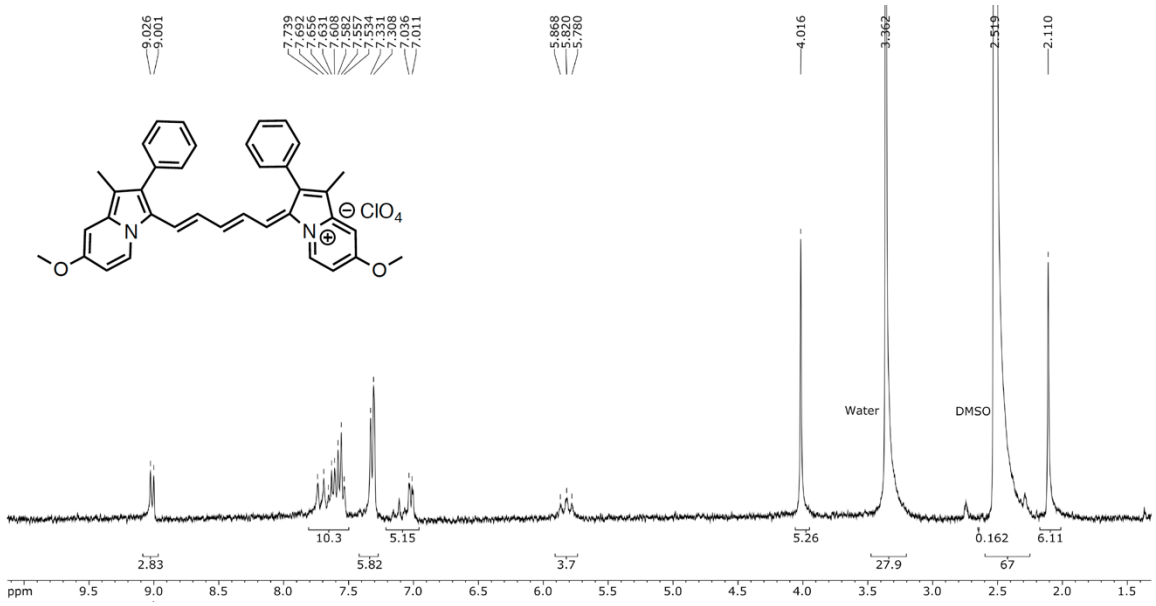

Figure S15. ^{1}H NMR (300 MHz, DMSO-d6) of **IndzOMe-C5**.

Table S3. Select computed bond angles. See below Table S4 for an illustration of the angles.

dye	angle 1 (°) GS | ES	angle 2 (°) GS | ES	angle 3 (°) GS | ES	angle 4 (°) GS | ES
C1 cis	128 | 123	134 | 125	N/A	N/A
C3 cis-7	129 | 127	133 | 129	118 | 121	N/A
C3 trans-7, 6	128, 123 | 127, 122	131, 126 | 129, 123	120 | 123	N/A
C5 cis-7	128 | 127	132 | 129	119 | 122	125 | 122
C5 cis-6	122 | 122	127 | 126	122 | 124	123 | 121
C5 trans-7, 6	128, 122 | 127, 122	133, 128 | 130, 126	120, 121 | 122, 123	125 | 123

Cis and trans refer to the relative orientation of the two indolizine groups.

Table S4. Select computed dihedral angles and atom-atom distances.

dye	dihedral (°) indz-cy GS | ES	dihedral (°) indz-indz GS | ES	H-H bond distance (Å) GS | ES
C1 cis	15 | 27	35 | 50	2.7 | 3.6[a]
C3 cis-7	3 | 21	8 | 2	1.8 | 2.0
C3 trans-7, 6	2, 10 | 11, 22	15 | 32	1.8, 2.1 | 1.9, 2.1
C5 cis-7	2 | 20	10 | 0	1.9 | 2.0
C5 cis-6	7 | 11	22 | 33	2.1 | 2.0
C5 trans-7, 6	3, 7 | 12, 15	12 | 35	1.9, 2.0 | 2.0, 2.0

Cis and trans refer to the relative orientation of the two indolizine groups.

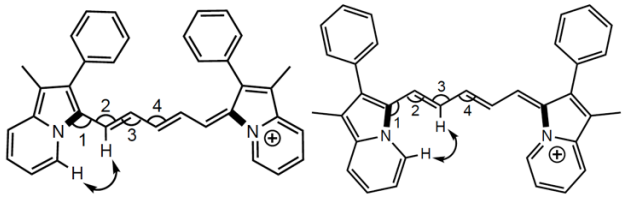

cis-6 conformer cis-7 conformer

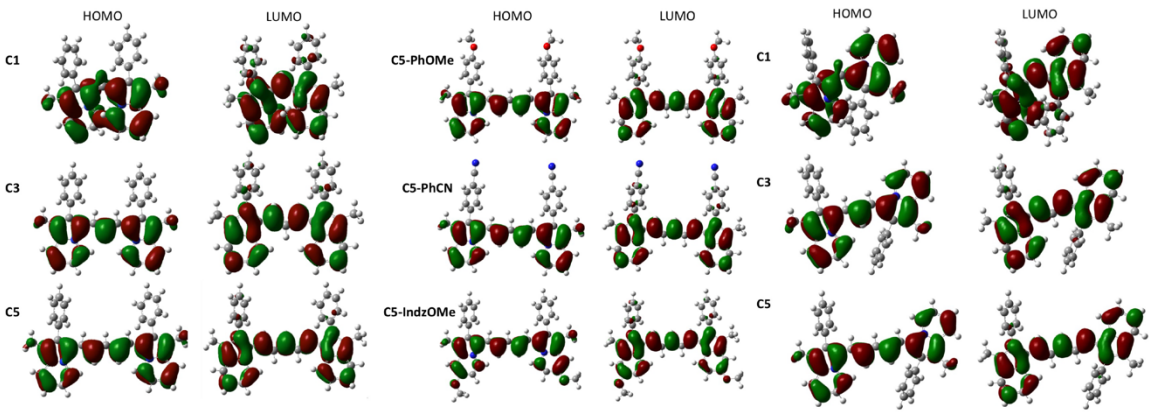

Figure S16. HOMO-LUMO diagrams of **C1**, **C3**, **C5**, **PhOMe-C5**, **PhCN-C5**, and **IndzOMe-C5**. The left two columns of HOMO-LUMO orbitals are shown as the cis-7 conformers, and the right column is shown as the trans conformer. See Table S4 for an illustration of cis-7 conformation. Isovalues of 0.02 are shown above.

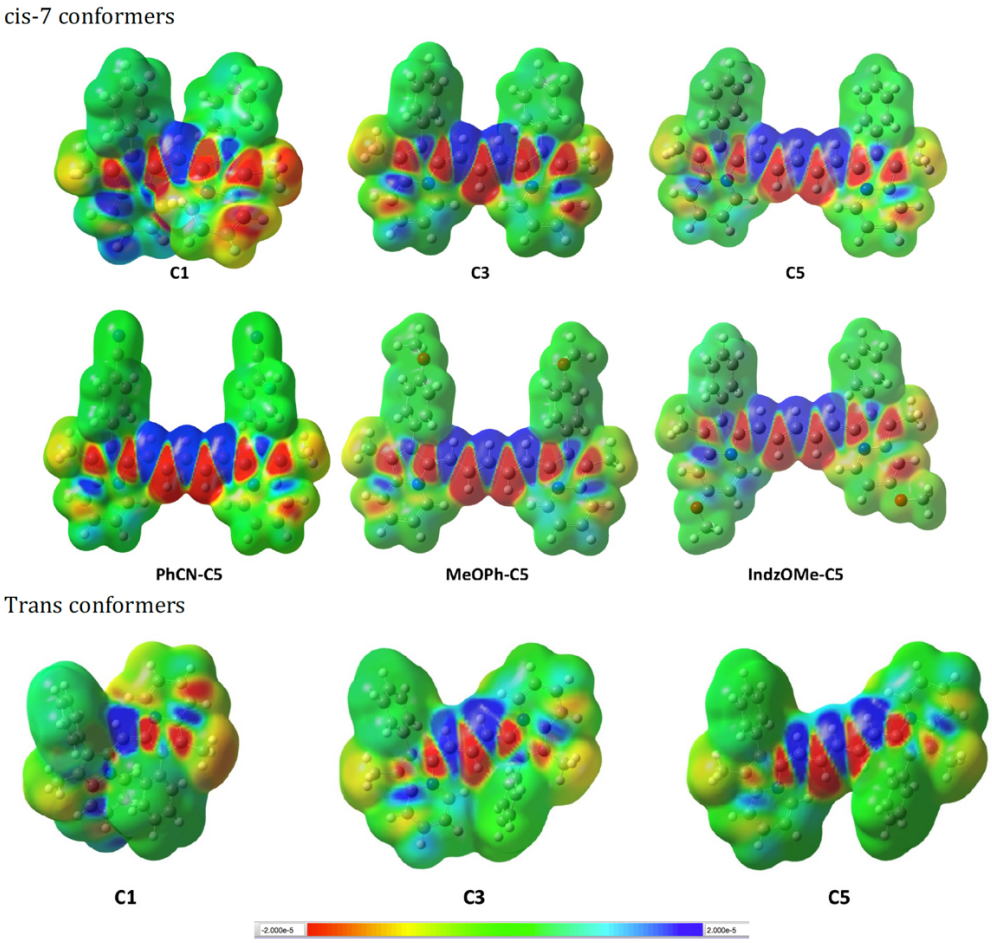

Figure S17. Electron density difference maps for **C1**, **C3**, **C5**, **PhCN-C5**, **PhOMe-C5**, and **IndzOMe-C5**. Red is where electrons originate from, blue is where they travel to upon photoexcitation, and green is neutral. Top dyes are in the cis-7 conformation as illustrated under Table S4, and the bottom row dyes are in the trans conformation.

Table S5. TD-DFT values for the ground- and excited-state optimized geometries for variable conformations.

dye	vertical trans. (eV, nm)	oscillator strength	dye* vertical trans. (eV, nm)	osc. str. dye*	Stokes shift (eV, nm)
C1 cis	2.20, 561	0.79	1.78, 697	0.47	0.42, 136
C3 cis-7	1.91, 648	1.49	1.74, 712	1.27	0.17, 64
C3 trans	2.33, 533	1.11	2.18, 569	0.97	0.15, 36
C5 cis-7	1.65, 752	2.06	1.51, 822	1.84	0.14, 70
C5 cis-6	2.08, 596	1.52	2.03, 611	1.75	0.05, 15
C5 trans	2.15, 576	1.78	2.04, 606	1.64	0.11, 30

See Table S4 for illustration of cis-6 and cis-7 conformations.

Table S6. Table of total energies and relative energies of ground state conformers.

dye	relative energy (kcal/mol)	energy (Hartree)
C1 cis	2.00	-1305.4230007
C1 trans	0.00	-1305.4261922
C3 cis-7	0.00	-1382.8119535
C3 trans-7, 6	4.44	-1382.8190310
C5 cis-7	1.98	-1460.2026484
C5 cis-6	0.00	-1460.2058166
C5 trans-7, 6	0.94	-1460.2043175

See Table S4 for illustration of cis-6 and cis-7 conformations.

XYZ Coordinates: See publisher's website for C1 cis Ground State, C1 cis Excited State, C1 trans Ground State, C3 cis-7 Ground State, C3 cis-7 Excited State, C3 trans Ground State, C3 trans Excited State, C5 cis-6 Ground, C5 cis-6 Excited State, C5 cis-7 Ground State, C5 cis-7 Excited State, C5 trans Ground State, and C5 trans Excited State in the full SI.

Crystallographic Data

Crystals were first transferred to polyisobutene oil, mounted on the tip of a fine glass fibre embedded in a copper mounting pin, and placed directly into the cold-stream path1 of a CryoIndustries LT3 lowtemperature device. X-ray diffraction data were collected at 90.0(2) K on a Bruker D8 Venture k-axis diffractometer using MoK(a) X-rays. Raw data were integrated, scaled, merged and corrected for Lorentz-polarization effects using the APEX3 package.2 Corrections for absorption were applied using SADABS.3 The structure was solved by direct methods (SHELXT)4 and refinement was carried out against F2 by weighted full-matrix least-squares (SHELXL)5. Hydrogen atoms were found in difference maps, but subsequently placed at calculated positions and refined using a riding model. Non-hydrogen atoms were refined with anisotropic displacement parameters. Atomic scattering factors were taken from the International Tables for Crystallography.6 For structure C3, a region of poorly-defined electron density could not be accounted for in a satisfactory way by modelling it as solvent. It was incorporated using the SQUEEZE method,7 as implemented in Platon8. Since SHELXL-2014,5 this allows for the contribution from any unmodelled electron density to be added to the calculated intensities via the ABIN command, which obtains the required information from a file with a .fab extension (generated by Platon). Crystal data, and relevant details of the structure determinations are summarized in Tables S3, S5, and S7 and selected geometrical parameters are given in Tables S4, S6, and S8.

For **Tables S7-S12** see publisher's website.

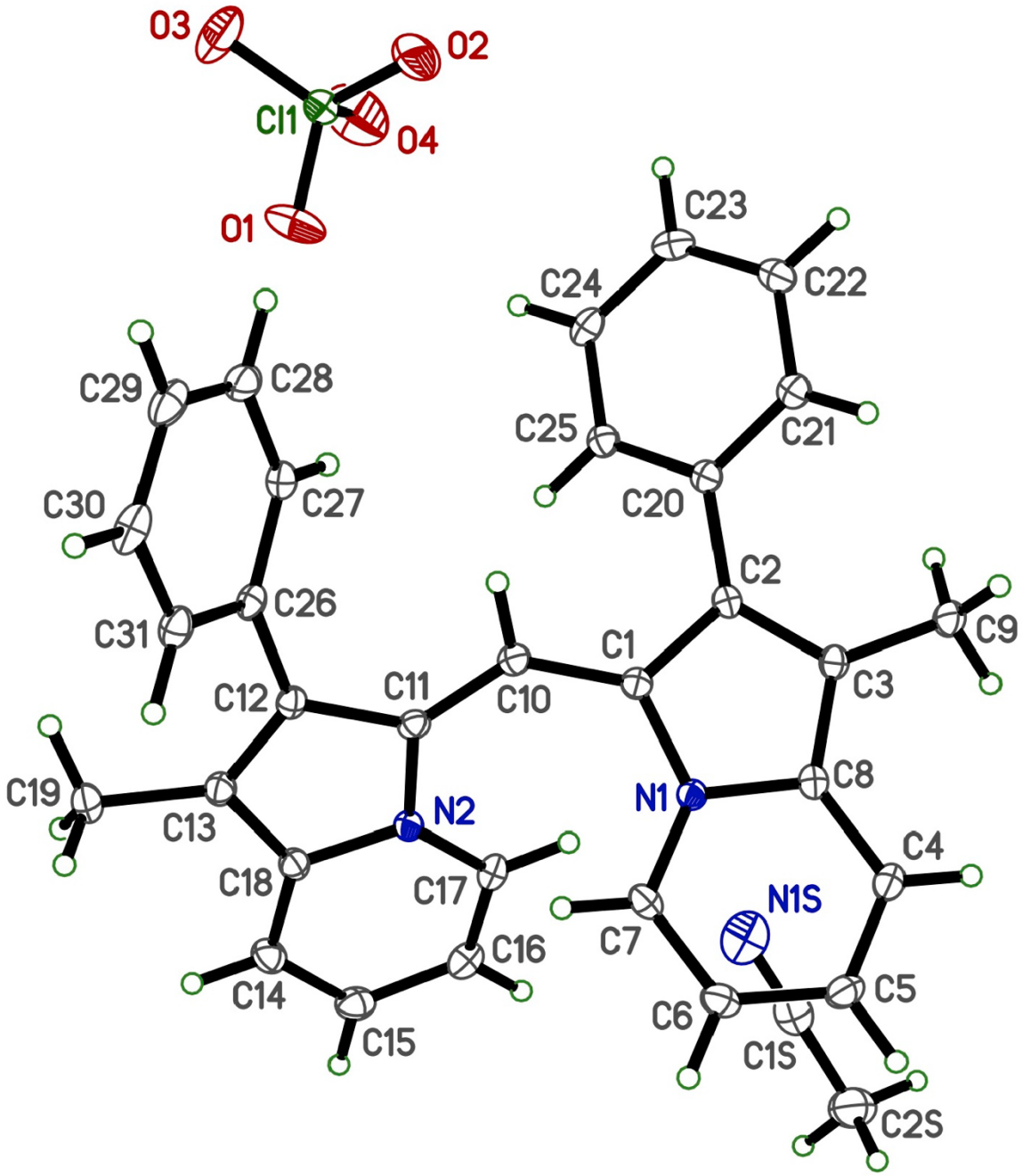

Figure S18. C1 thermal ellipsoid plot at 50% probability for a single **C1** molecule with added hydrogens.

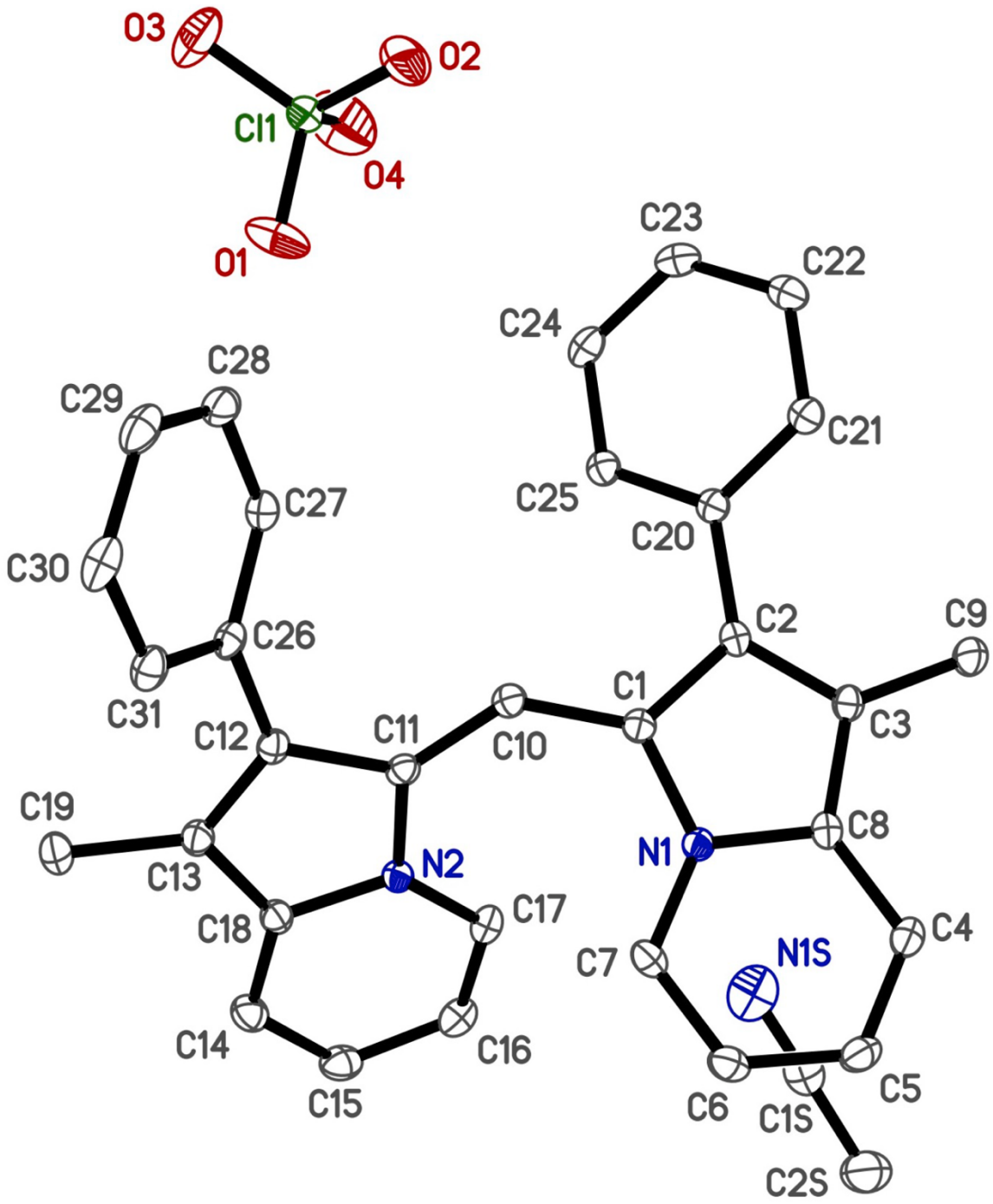

Figure S19. C1 thermal ellipsoid plot at 50% probability for a single **C1** molecule.

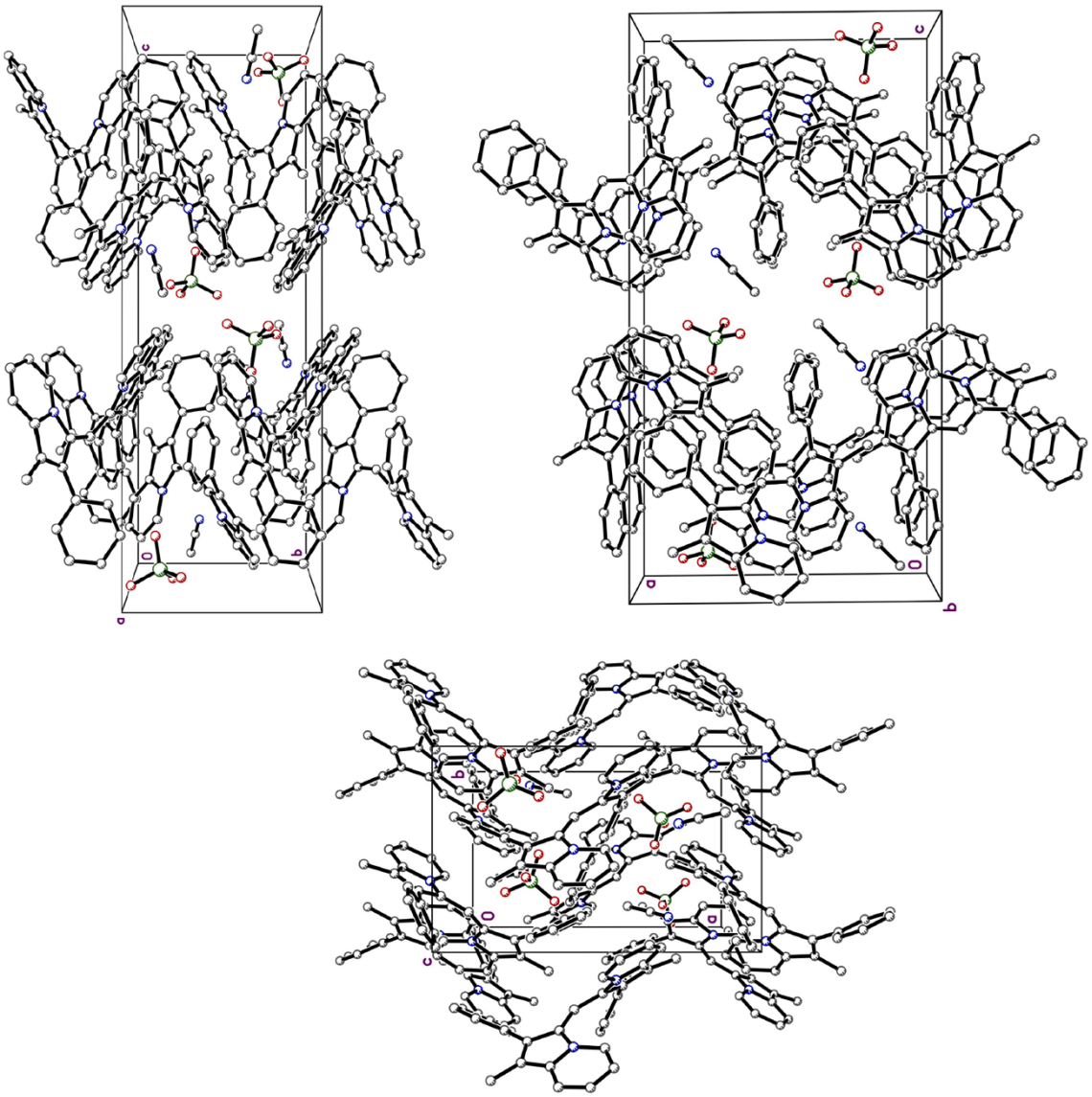

Figure S20. Crystal packing structure for **C1** from three different perspectives.

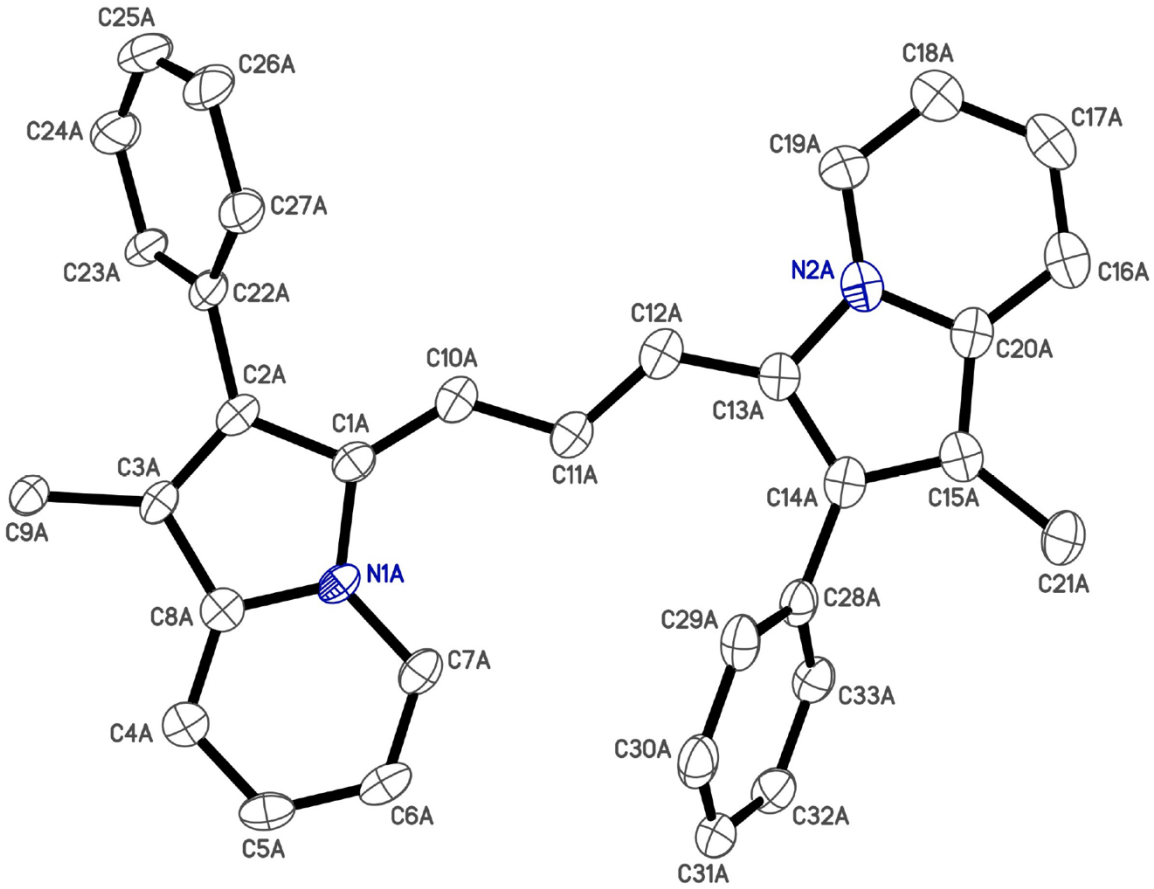

Figure S21. C3 molecule A thermal ellipsoid plot at 50% probability for a single **C3** molecule A.

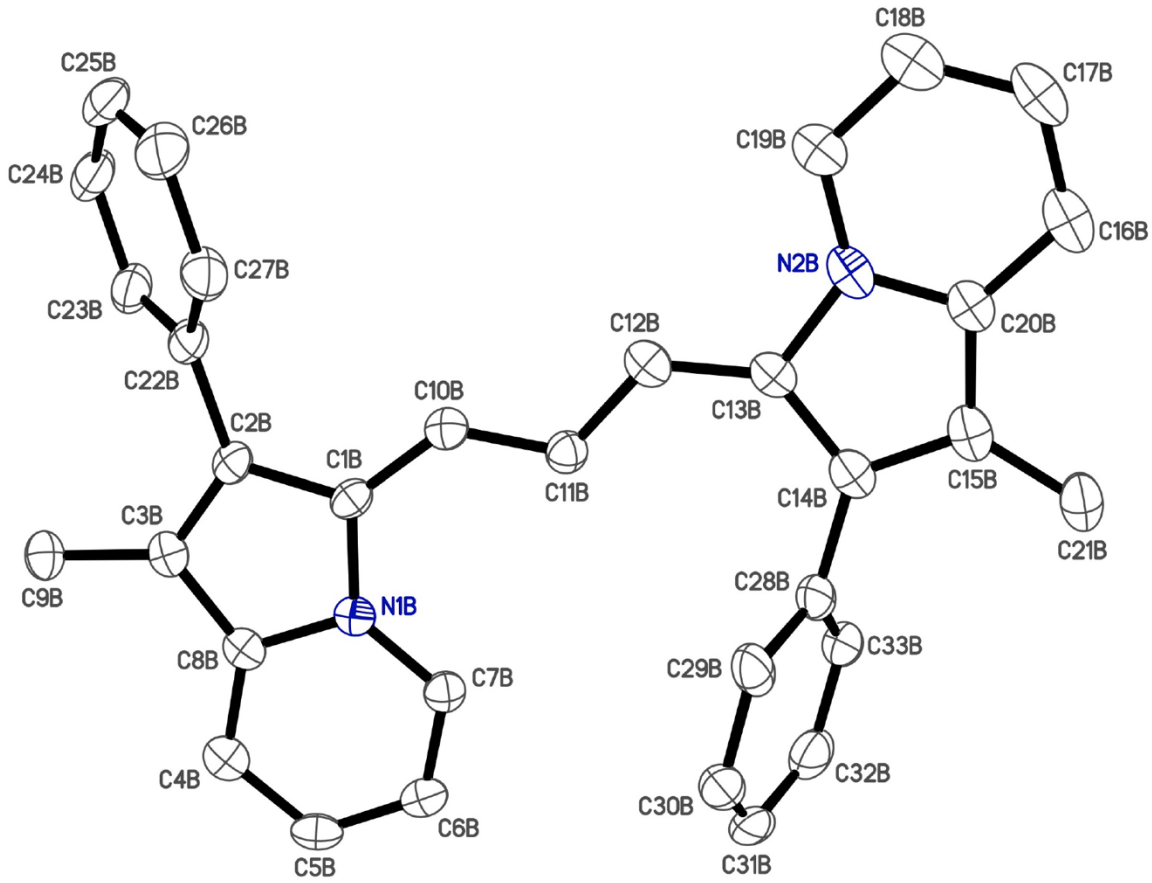

Figure S22. C3 molecule B thermal ellipsoid plot at 50% probability for a single **C3** molecule B.

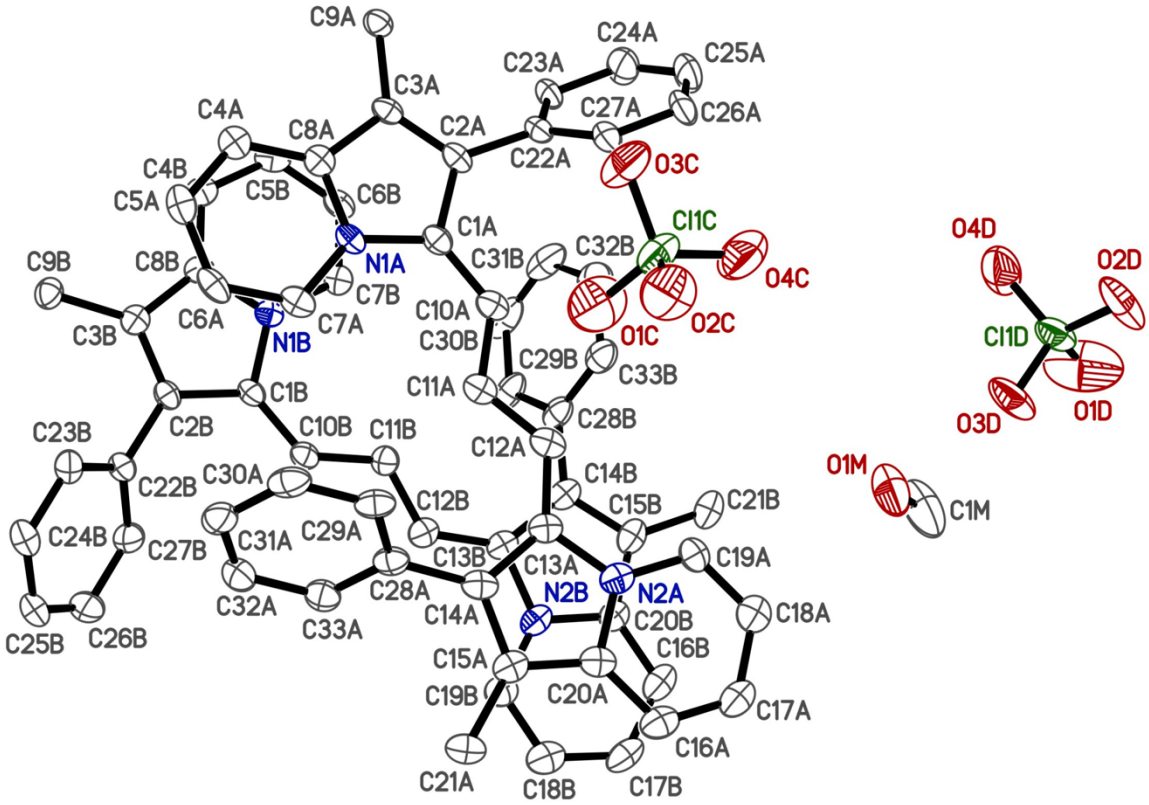

Figure S23. C3 thermal ellipsoid plot at 50% probability for a molecule A and B of **C3**.

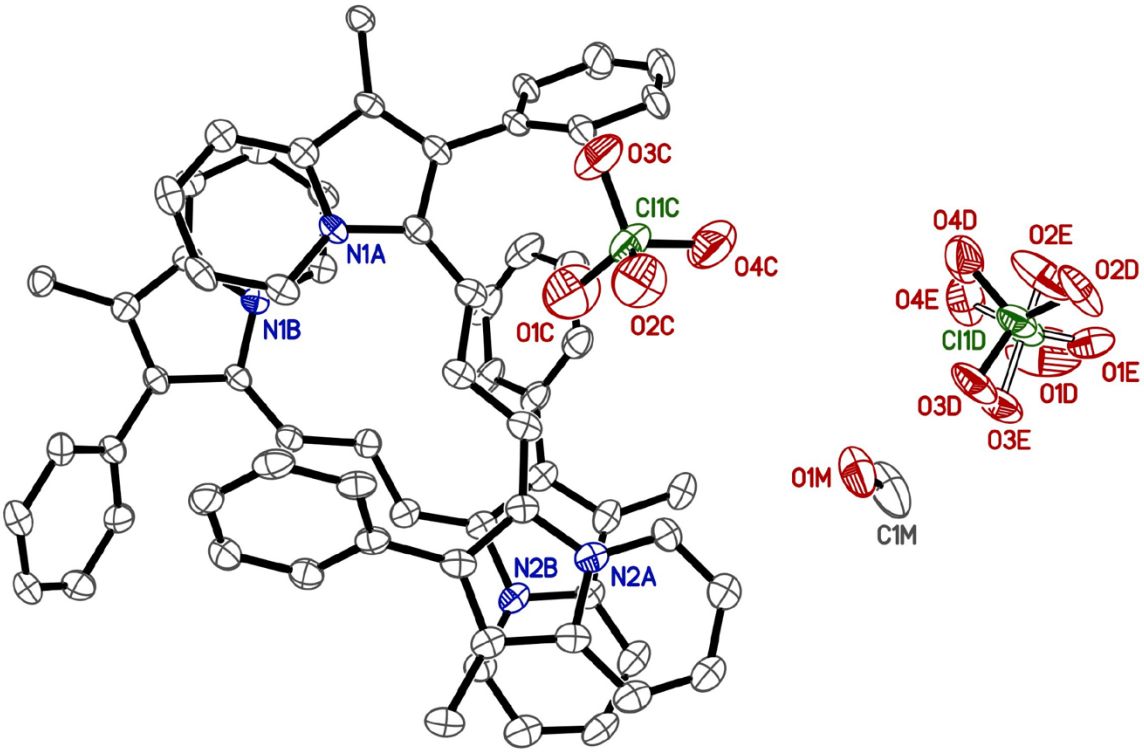

Figure S24. C3 thermal ellipsoid plot at 50% probability for a molecule A and B of **C3** with a reduced atom label count.

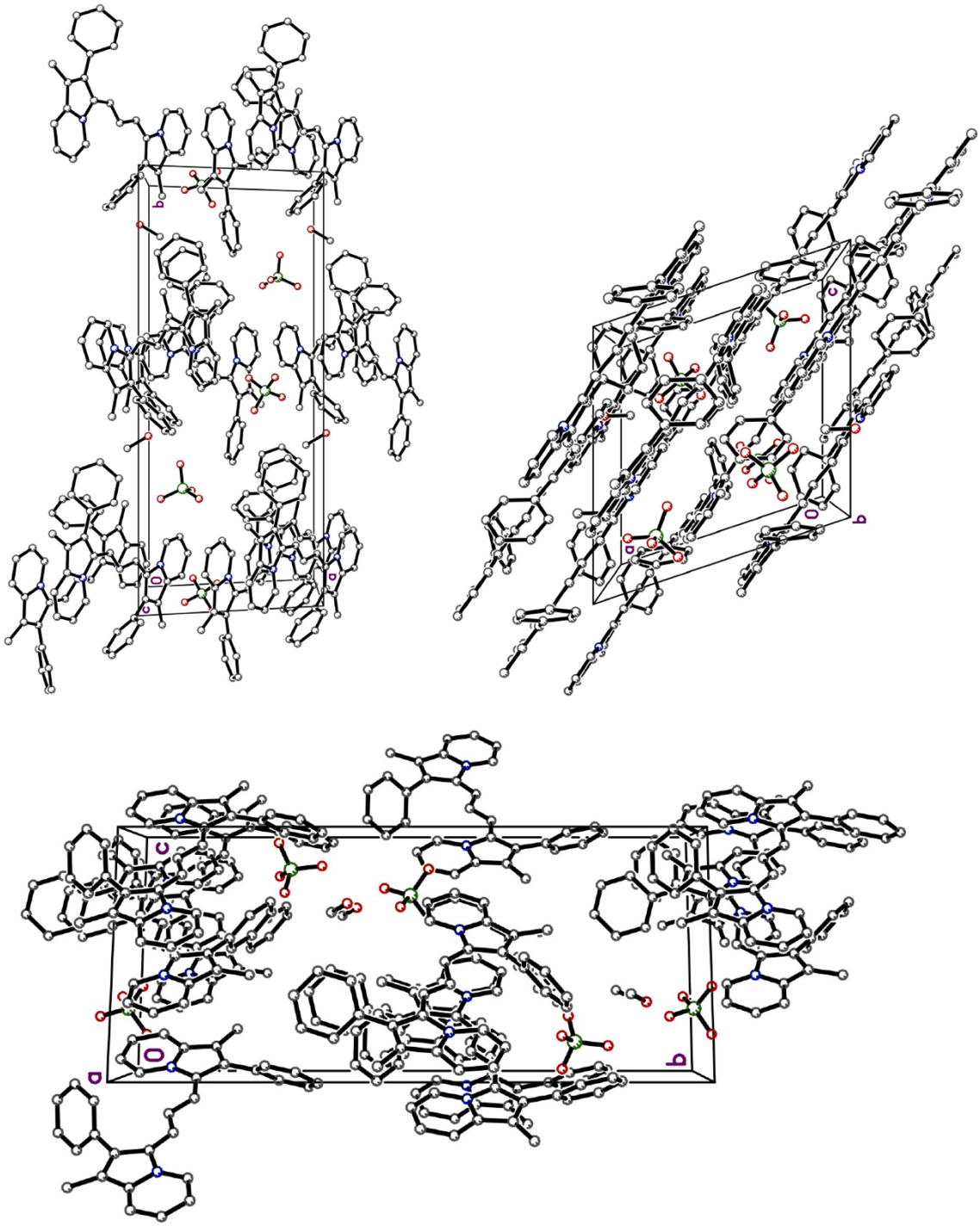

Figure S25. Crystal packing structure for **C3** from three different perspectives.

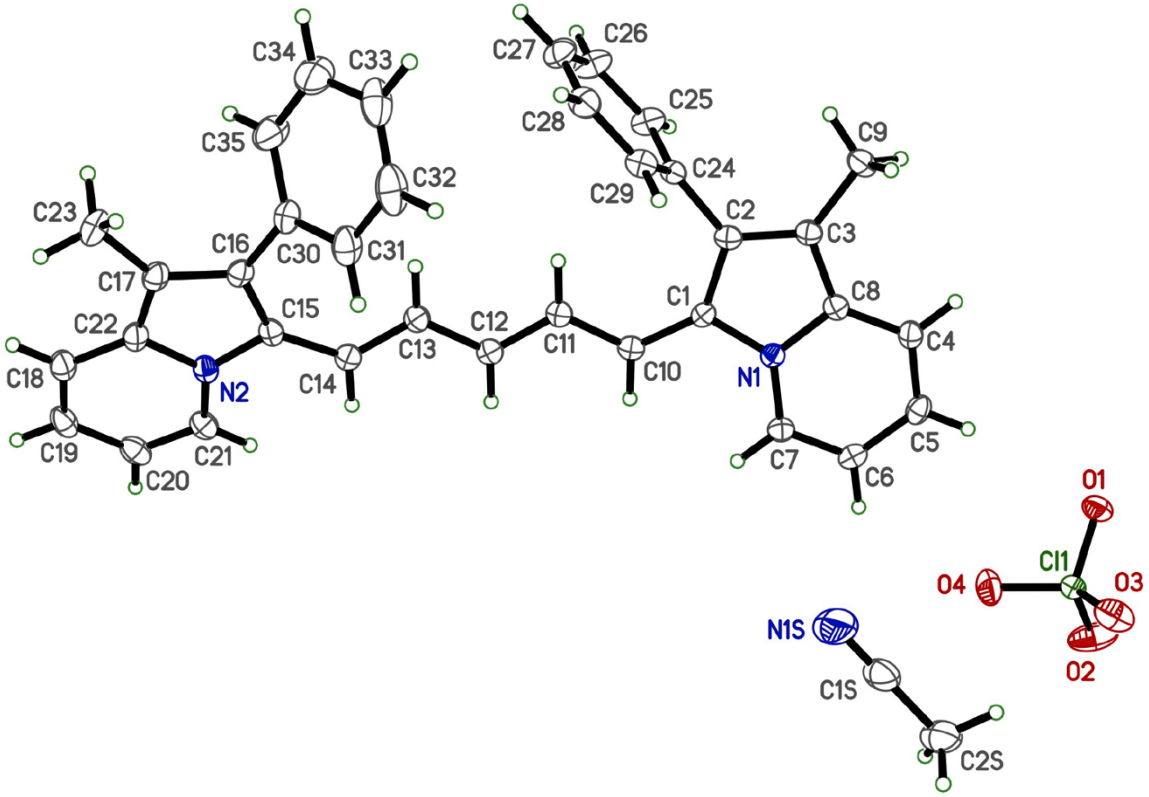

Figure S26. C5 thermal ellipsoid plot at 50% probability for a single **C5** molecule with added hydrogens.

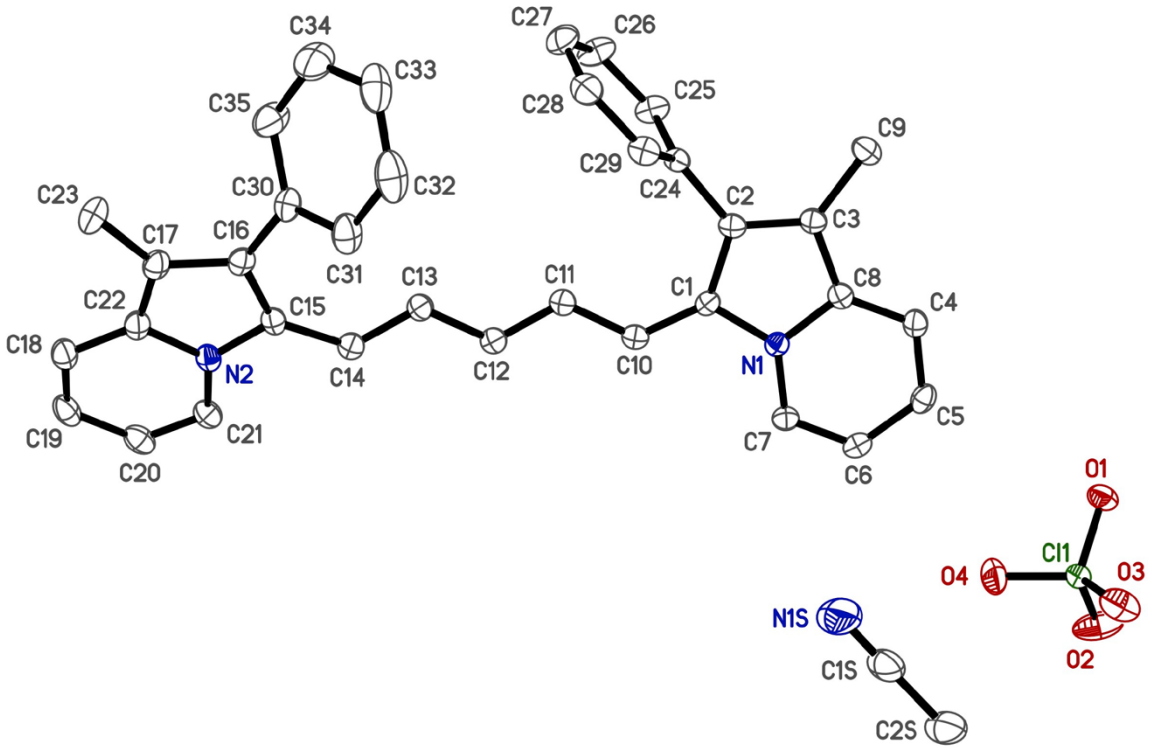

Figure S27. C5 thermal ellipsoid plot at 50% probability for a single **C5** molecule.

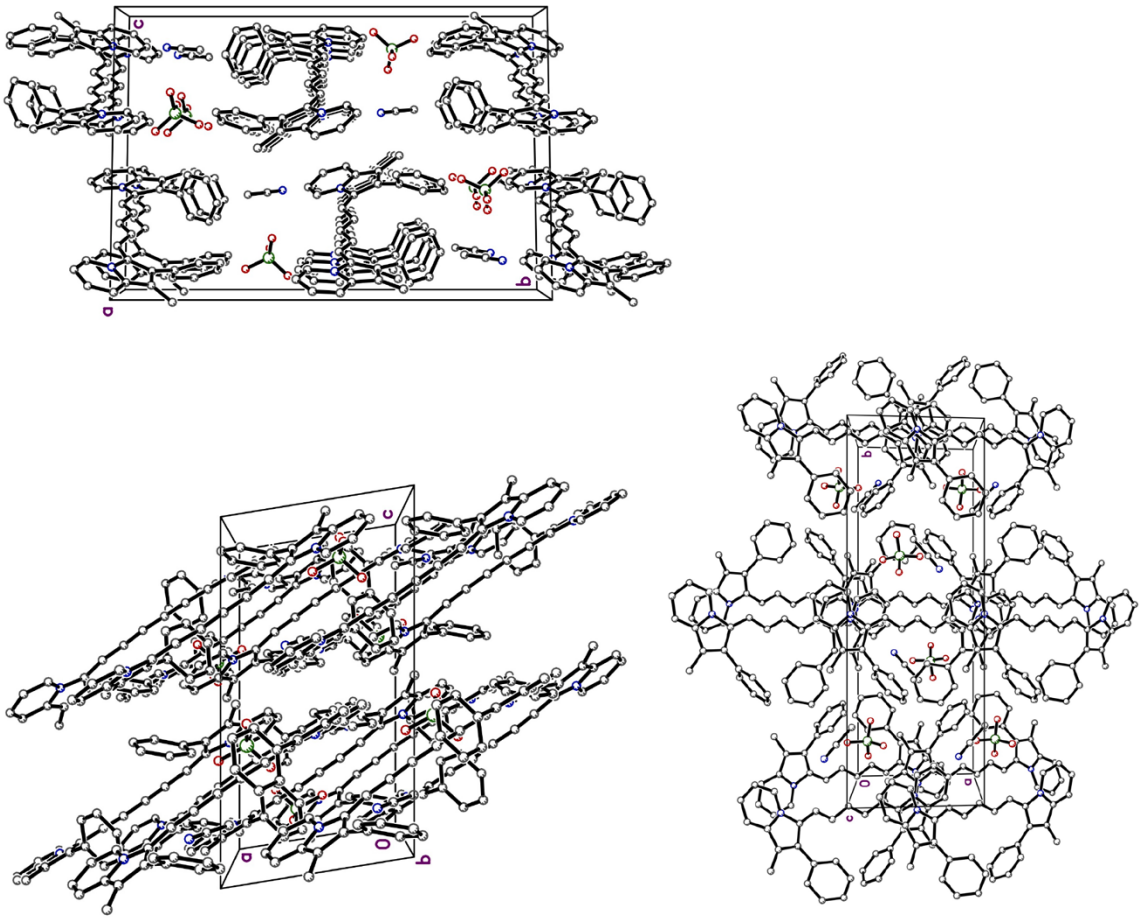

Figure S28. Crystal packing structure for **C5** from three different perspectives.

Table S1. Further optimization of **2a** from xanthene ditriflate

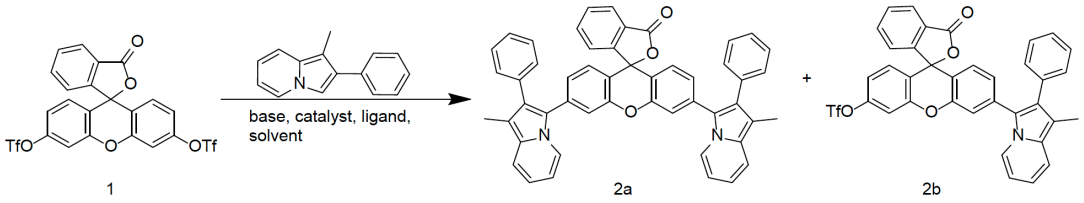

1 2a 2b

Entry	Catalyst (equiv)	Ligand (equiv)	Base (equiv)	Additive (equiv)	Solvent	Temp (°C)	Time (h)	(%) 2a:2b
1	$PdCl_2(PPh_3)_2$ (0.1)	None	Cs_2CO_3 (3.0)	None	NMP	80	18	<5
2	$PdCl_2(PPh_3)_2$ (0.1)	None	KO^{t}Bu (3.0)	None	NMP	80	18	0
3	$PdCl_2(PPh_3)_2$ (0.1)	None	NaO^{t}Bu (3.0)	None	NMP	80	18	0
4	$Pd(OAc)_2$ (0.1)	(^{t}Bu)$_2$PMeHBF$_4$ (0.2)	K_2CO_3 (6.0)	PivOH (0.3)	DMA	100	20	0
5	$Pd(OAc)_2$ (0.1)	XPhos (0.2)	K_2CO_3 (6.0)	PivOH (0.3)	DMA	100	20	0
6	$Pd(OAc)_2$ (0.05)	BINAP (0.075)	Cs_2CO_3 (3.0)	None	Toluene	100	20	trace
7	$Pd(OAc)_2$ (0.05)	BINAP (0.075)	Cs_2CO_3 (3.0)	PivOH (0.3)	Toluene	100	20	trace
8	$Pd(OAc)_2$ (0.05)	BINAP (0.075)	Cs_2CO_3 (3.0)	None	THF	100	20	trace
9	$Pd(OAc)_2$ (0.05)	BINAP (0.075)	Cs_2CO_3 (3.0)	None	Dioxane	100	20	trace
10	$Pd(dba)_3$. $CHCl_3$ adduct (0.1)	XPhos (0.2)	Cs_2CO_3 (3.0)	PivOH (0.3)	THF	100	24	0

Unless otherwise specified, the reaction was carried out in a sealed tube under nitrogen atmosphere in the presence of **1** (0.083 mmol) and 1-methyl-2-phenylindolizine (0.167 mmol), solvent (0.34 – 2.0 mL), catalyst (5 – 10 mol %), base, and additives (pivalic acid) for 12 – 24 h at 80 – 150 °C. Isolated yields (%) were reported for **2a** and **2b**.

Table S2. Further Optimization of **2a** from 3′,6′-dibromofluoran (**3**).

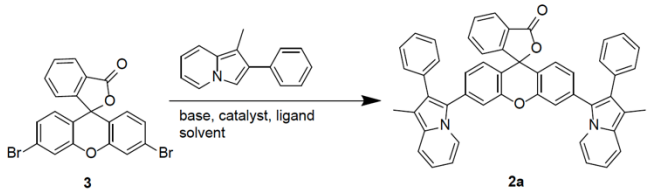

3 **2a**

Entry	Catalyst (equiv)	Ligand (equiv)	Base (equiv)	Additive (equiv)	Solvent	Temp (°C)	Time (h)	Yield (%)
1	$PdCl_2(PPh_3)_2$ (0.1)	None	NaO^tBu (5.2)	None	NMP	80	18	0
2	$Pd(OAc)_2$ (0.05)	$(^tBu)_2PMeHBF_4$ (0.1)	K_2CO_3 (1.5)	PivOH (0.3)	DMA	100	18	0
3	$Pd(OAc)_2$ (0.1)	XPhos (0.2)	KOAc (3.0)	None	DMF	100	18	trace

Unless otherwise specified, the reaction was carried out in a sealed tube under nitrogen atmosphere in the presence of **3** (0.11 mmol) and 1-methyl-2-phenylindolizine (0.24 mmol), solvent (0.34 – 2 mL), catalyst (5 – 10 mol %), base, and additives (PivOH) for 18 – 24 h at 80 – 150 °C. Isolated yields (%) were reported for **2a**.

Unless otherwise specified, the reaction was carried out in a sealed tube under nitrogen atmosphere in the presence of **3** (0.11 mmol) and 1-methyl-2-phenylindolizine (0.24 mmol), solvent (0.34 – 2 mL), catalyst (5 – 10 mol %), base, and additives (PivOH) for 18 – 24 h at 80 – 150 °C. Isolated yields (%) were reported for **2a**.

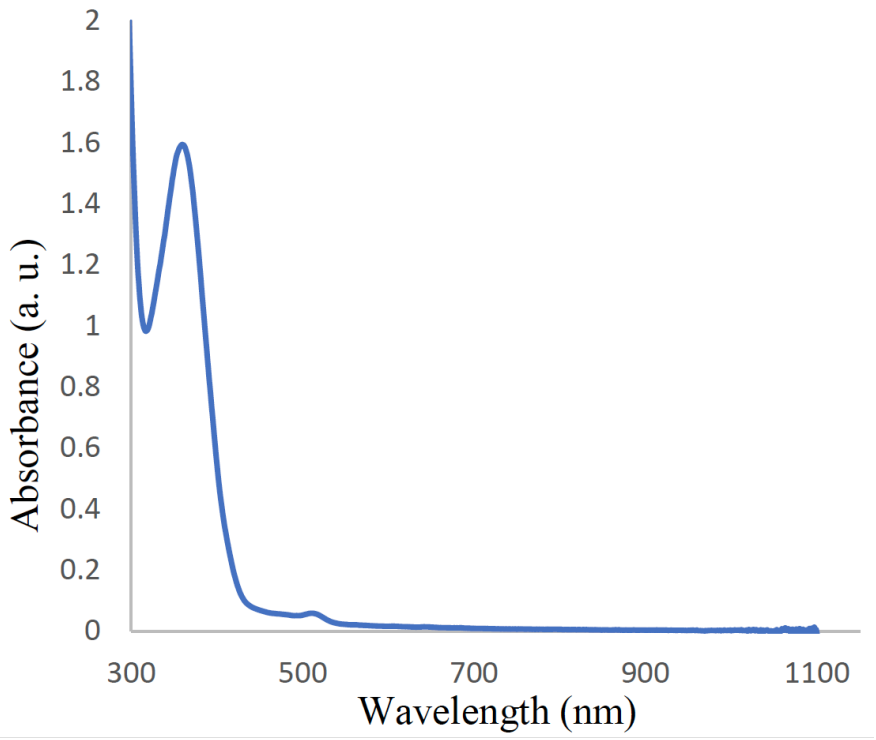

Figure S1. UV absorption of Rhodoindolizine Lactone (**2a**)

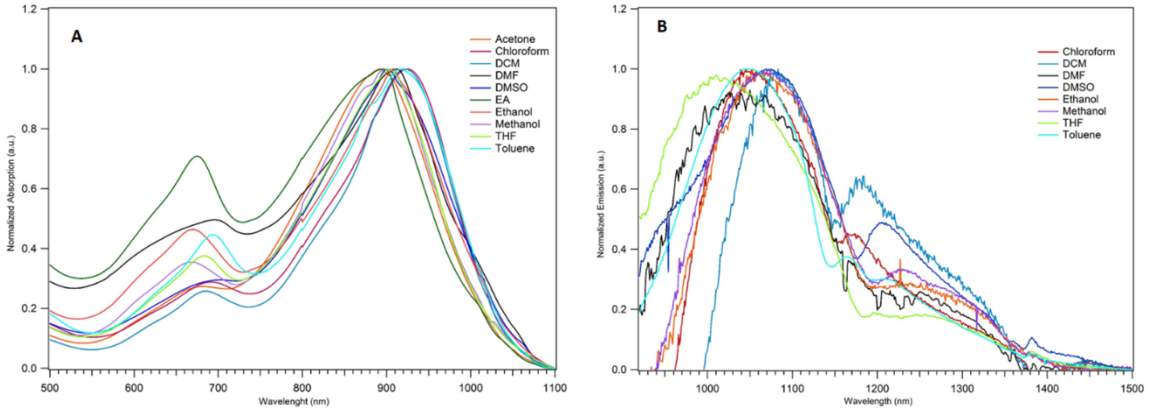

Figure S2.Absorption (A) and Emission (B) spectra for the solvatochromic effects of RhIndz ethyl ester (**10**)

Table S3. Solvent effects on the photophysical properties of RhIndz ethyl ester (**10**)

Solvent	Dielectric Constant	Dipole (D)	Abs Max (nm)	Abs Max (eV)	Emission Max (nm)	Emission Max (eV)
Acetone	21	2.88	893	1.388	***	***
Chloroform	4.8	1.04	925	1.340	1051	1.179
DCM	9.1	1.60	921	1.346	1086	1.142
DMF	38	3.82	912	1.359	1041	1.191
DMSO	46.7	3.96	901	1.376	1075	1.153
Ethyl Acetate	6.0	1.78	896	1.384	***	***
Ethanol	24.6	1.69	908	1.365	1071	1.158
Methanol	33	1.70	900	1.378	1073	1.155
THF	7.5	1.75	903	1.373	1014	1.223
Toluene	2.4	0.36	917	1.352	1057	1.173

*** no appreciable emission in these solvents

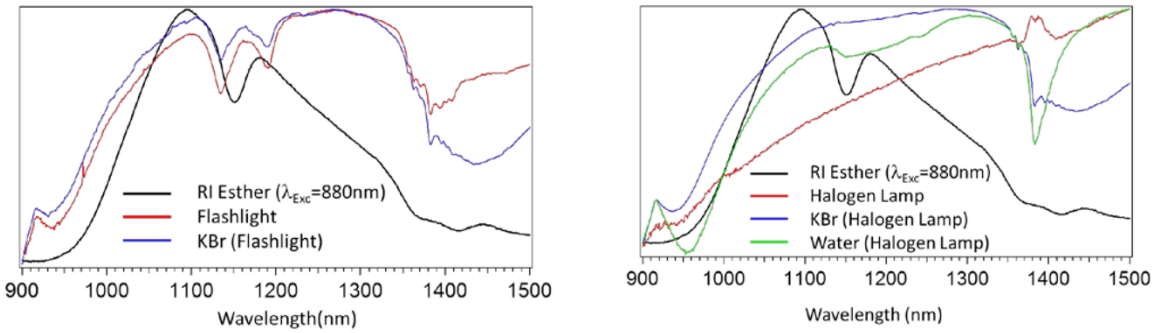

Figure S3. Spectra showing the artifact in the emission spectrum with different light sources

Figure S4. ^{1}H and ^{13}C NMR Data ($CDCl_3$, CD_2Cl_2 and $(CD_3)_2CO$) Grease and residual NMP can be seen in some spectra.

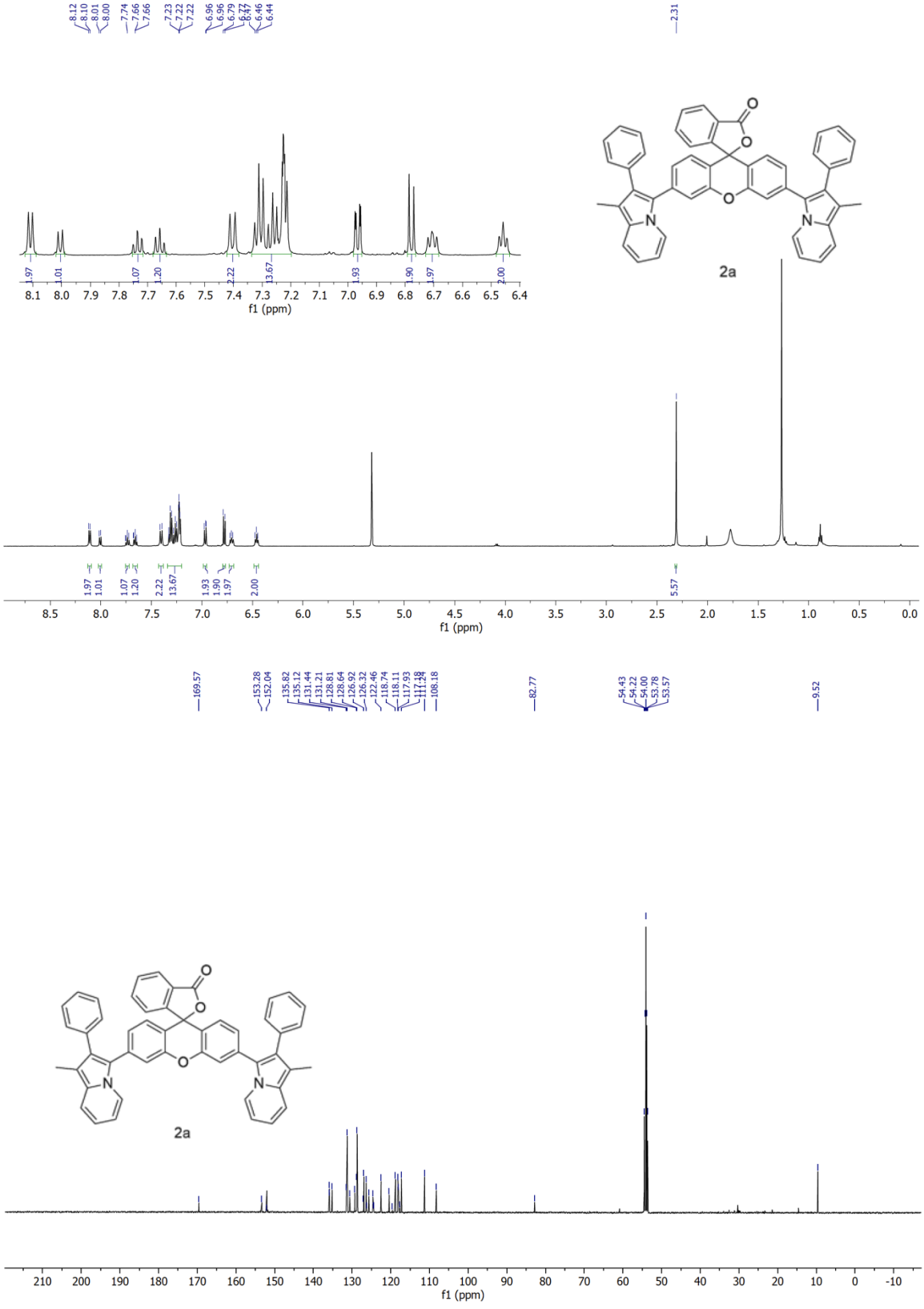

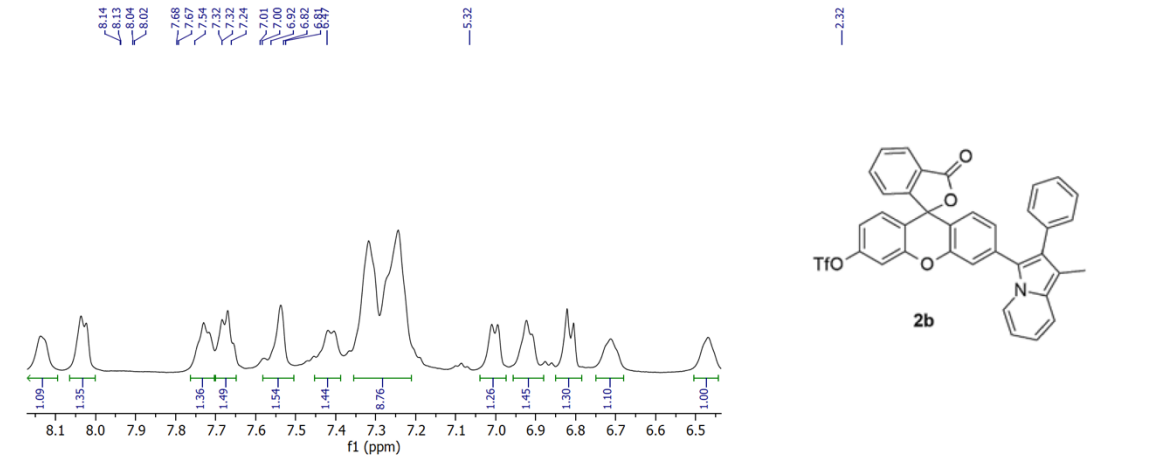
8.14
8.13
8.04
8.02
7.68
7.67
7.54
7.32
7.32
7.24
7.01
7.00
6.92
6.82
6.81
6.47
5.32
2.32
TfO
O
O
O
N
2b
1.09
1.35
1.36
1.49
1.54
1.44
8.76
1.26
1.45
1.30
1.10
1.00
f1 (ppm)

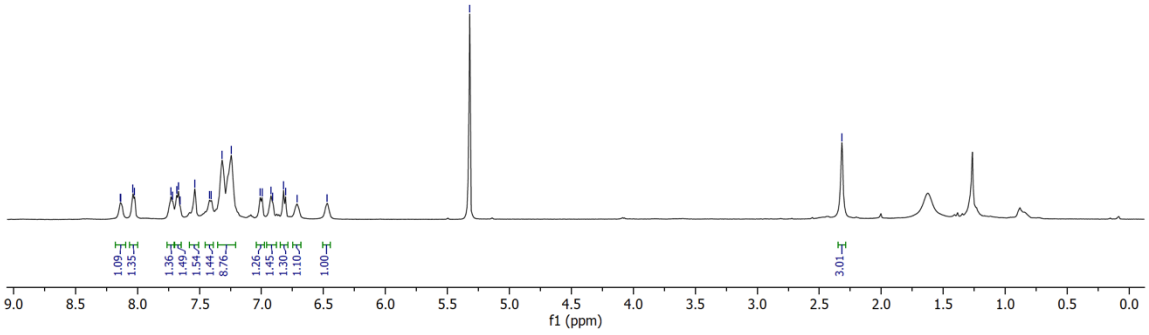
1.09
1.35
1.36
1.49
1.54
1.44
8.76
1.26
1.45
1.30
1.10
1.00
3.01
f1 (ppm)

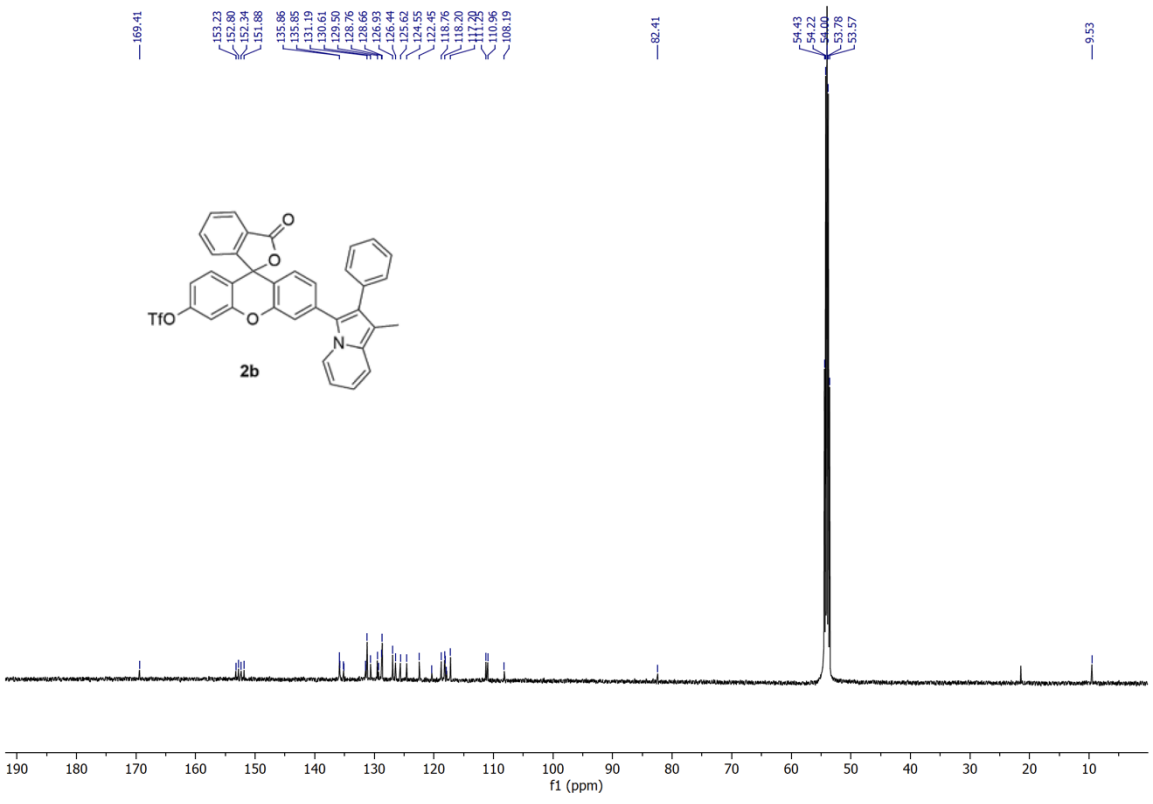
169.41
153.23
152.80
152.34
151.88
135.86
135.85
131.19
130.61
129.50
128.76
128.66
126.93
126.44
125.62
124.55
122.45
118.76
118.20
110.96
108.19
82.41
54.43
54.22
54.00
53.78
53.57
9.53
TfO
O
O
O
N
2b
f1 (ppm)

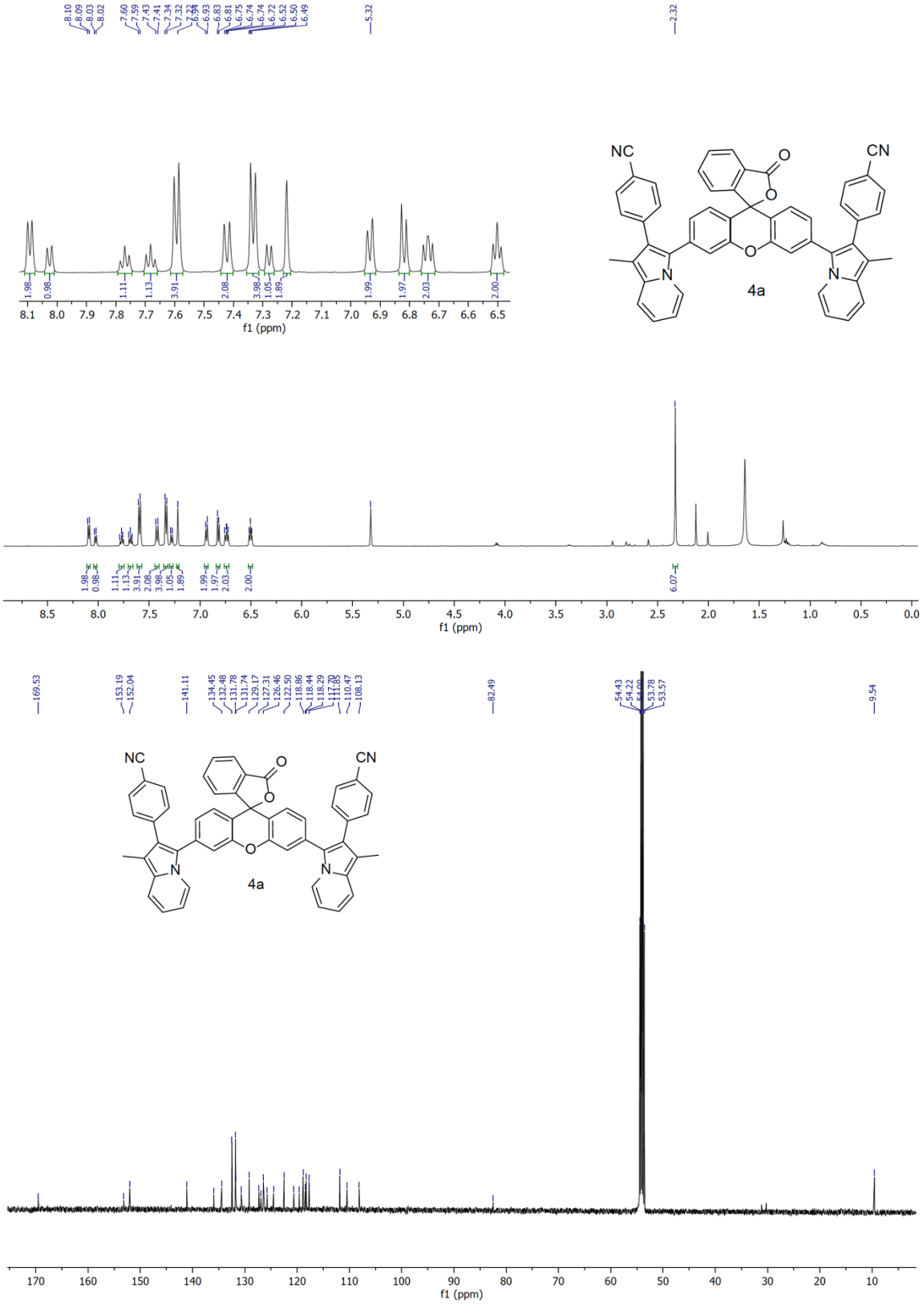
8.10
8.09
8.03
8.02
7.60
7.59
7.43
7.41
7.34
7.32
6.93
6.83
6.81
6.75
6.74
6.74
6.72
6.52
6.50
6.49
5.32
2.32
1.98
0.98
1.11
1.13
3.91
2.08
3.98
1.05
1.89
1.99
1.97
2.03
2.00
8.1 8.0 7.9 7.8 7.7 7.6 7.5 7.4 7.3 7.2 7.1 7.0 6.9 6.8 6.7 6.6 6.5
f1 (ppm)
NC
CN
O
O
N
N
4a
6.07
8.5 8.0 7.5 7.0 6.5 6.0 5.5 5.0 4.5 4.0 3.5 3.0 2.5 2.0 1.5 1.0 0.5 0.0
f1 (ppm)
169.53
153.19
152.04
141.11
134.45
132.48
131.78
131.74
129.17
127.31
126.46
122.50
118.86
118.44
118.29
110.47
108.13
82.49
54.43
54.22
53.78
53.57
9.54
NC
CN
O
O
N
N
4a
170 160 150 140 130 120 110 100 90 80 70 60 50 40 30 20 10
f1 (ppm)

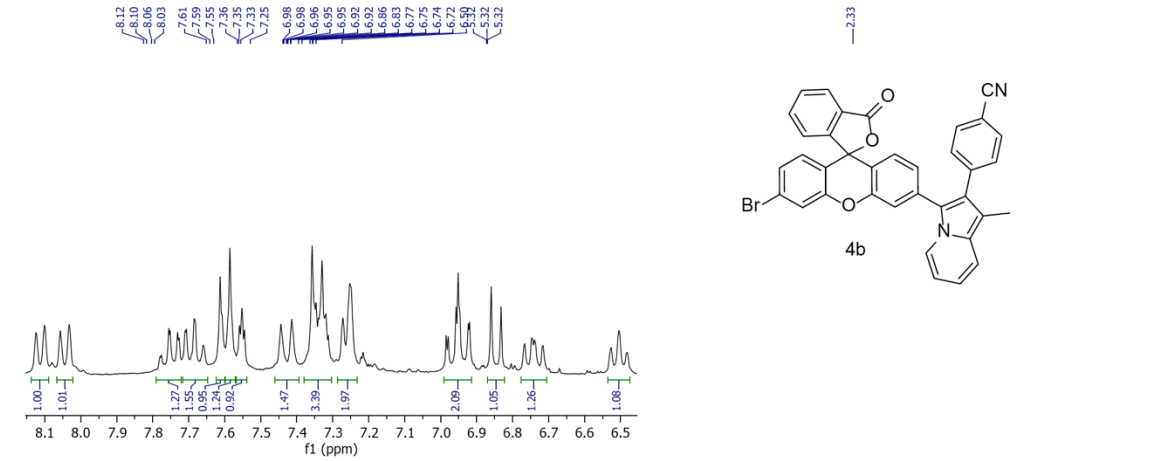
8.12
8.10
8.06
8.03
7.61
7.59
7.55
7.36
7.35
7.33
7.25
6.98
6.98
6.96
6.95
6.92
6.86
6.83
6.77
6.75
6.74
6.72
6.50
5.32
5.32
2.33
O
O
CN
Br
O
N
4b
1.00
1.01
1.27
1.55
0.95
1.24
0.92
1.47
3.39
1.97
2.09
1.05
1.26
1.08
8.1 8.0 7.9 7.8 7.7 7.6 7.5 7.4 7.3 7.2 7.1 7.0 6.9 6.8 6.7 6.6 6.5
f1 (ppm)

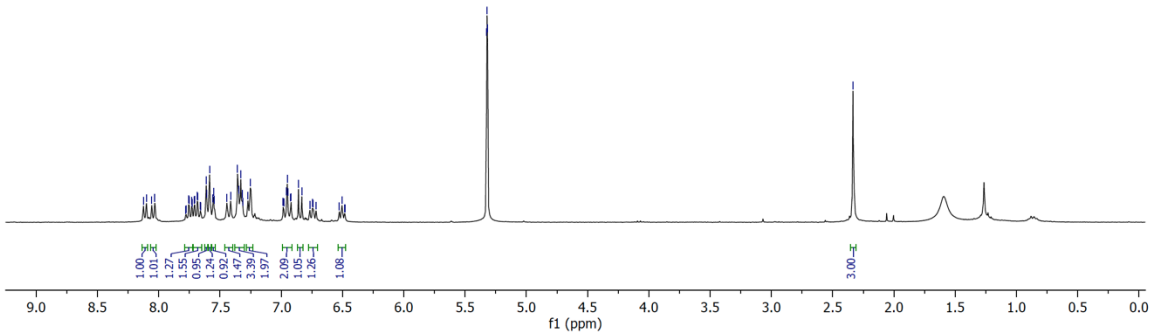
1.00
1.01
1.27
1.55
0.95
1.24
0.92
1.47
3.39
1.97
2.09
1.05
1.26
1.08
3.00
9.0 8.5 8.0 7.5 7.0 6.5 6.0 5.5 5.0 4.5 4.0 3.5 3.0 2.5 2.0 1.5 1.0 0.5 0.0
f1 (ppm)

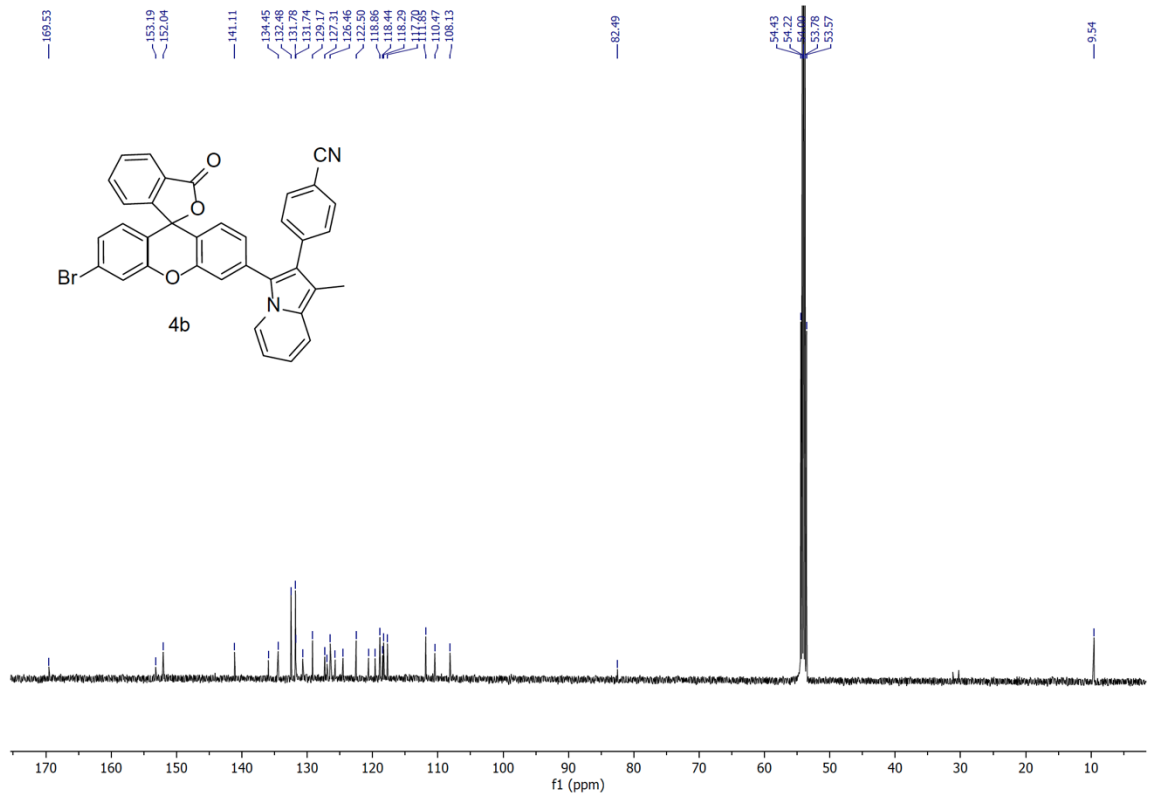
169.53
153.19
152.04
141.11
134.45
132.48
131.78
131.74
129.17
127.31
126.46
122.50
118.86
118.44
118.29
111.80
110.47
108.13
82.49
54.43
54.22
54.00
53.78
53.57
9.54
O
O
CN
Br
O
N
4b
170 160 150 140 130 120 110 100 90 80 70 60 50 40 30 20 10
f1 (ppm)

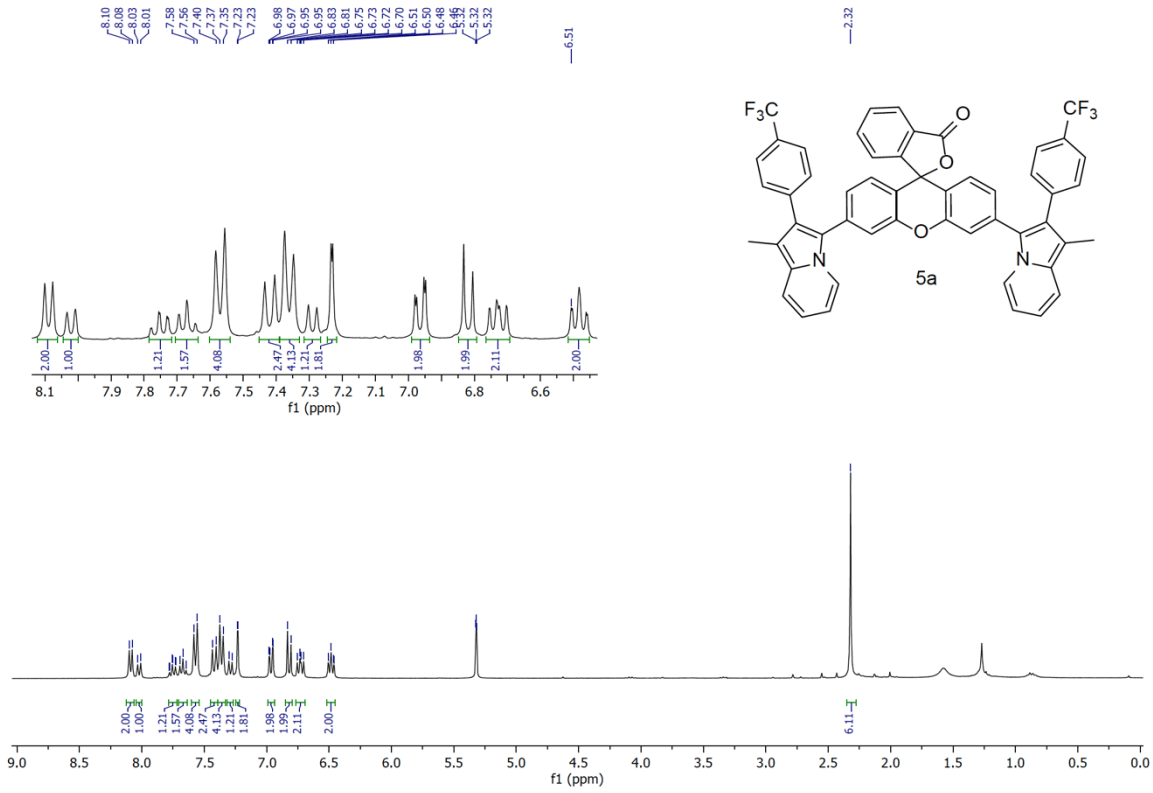
8.10
8.08
8.03
8.01
7.58
7.56
7.40
7.37
7.35
7.23
7.23
6.98
6.97
6.95
6.95
6.83
6.81
6.75
6.73
6.72
6.70
6.51
6.50
6.48
5.32
5.32
6.51
2.32
F3C
CF3
O
O
O
N
N
5a
2.00
1.00
1.21
1.57
4.08
2.47
4.13
1.21
1.81
1.98
1.99
2.11
2.00
6.11
8.1
7.9
7.8
7.7
7.6
7.5
7.4
7.3
7.2
7.1
7.0
6.8
6.6
f1 (ppm)
9.0
8.5
8.0
7.5
7.0
6.5
6.0
5.5
5.0
4.5
4.0
3.5
3.0
2.5
2.0
1.5
1.0
0.5
0.0
f1 (ppm)

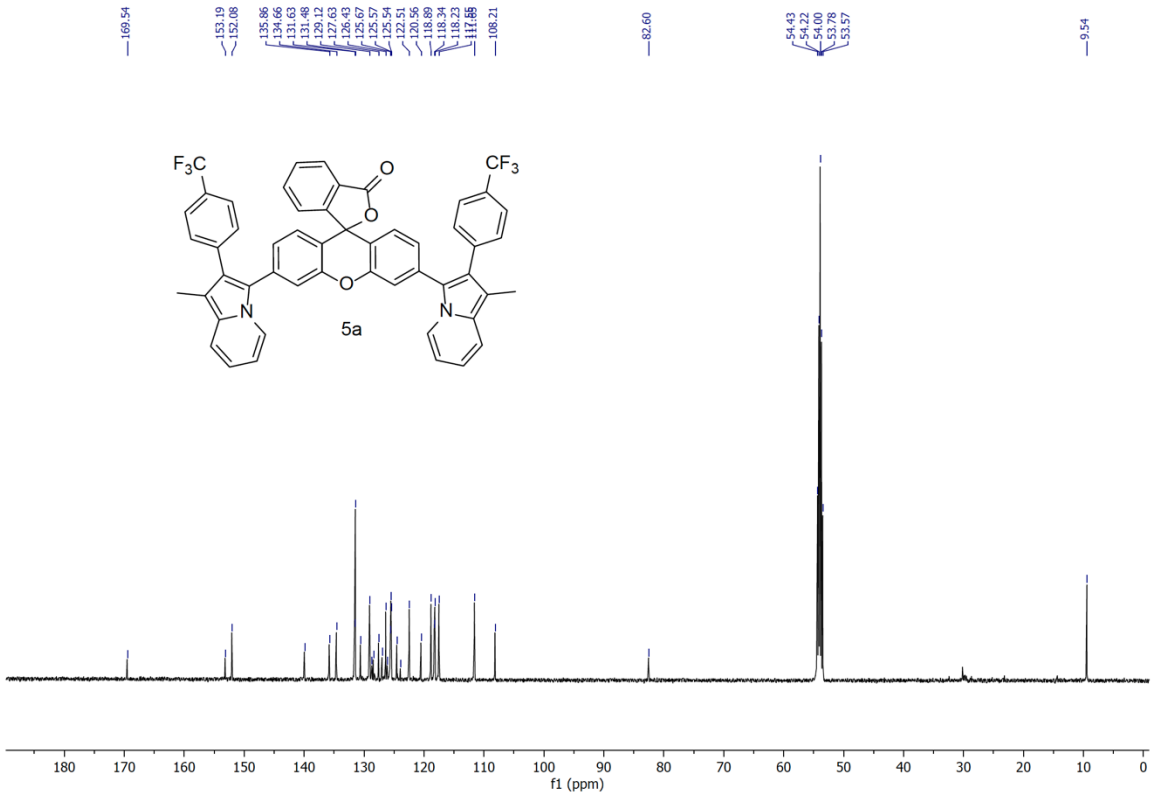
169.54
153.19
152.08
135.86
134.66
131.63
131.48
129.12
127.63
126.43
125.67
125.57
125.54
122.51
120.56
118.89
118.34
118.23
108.21
82.60
54.43
54.22
54.00
53.78
53.57
9.54
F3C
CF3
O
O
O
N
N
5a
180
170
160
150
140
130
120
110
100
90
80
70
60
50
40
30
20
10
0
f1 (ppm)

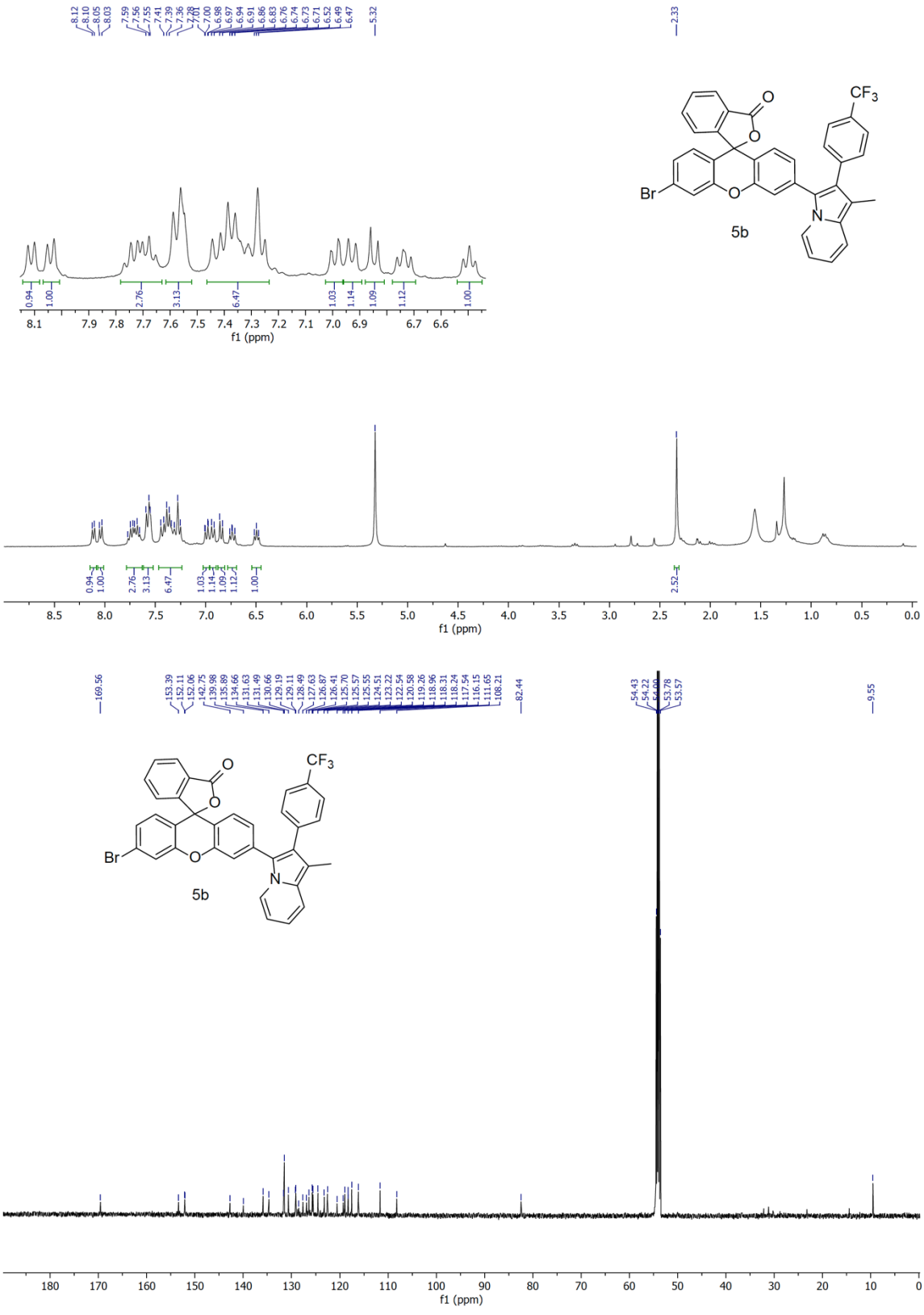
8.12
8.10
8.05
8.03
7.59
7.56
7.55
7.41
7.39
7.36
7.28
7.01
7.00
6.98
6.97
6.94
6.91
6.86
6.83
6.76
6.74
6.73
6.71
6.52
6.49
6.47
5.32
2.33
O
O
CF3
Br
O
N
5b
0.94
1.00
2.76
3.13
6.47
1.03
1.14
1.09
1.12
1.00
8.1
7.9
7.8
7.7
7.6
7.5
7.4
7.3
7.2
7.1
7.0
6.9
6.7
6.6
f1 (ppm)
0.94
1.00
2.76
3.13
6.47
1.03
1.14
1.09
1.12
1.00
2.52
8.5
8.0
7.5
7.0
6.5
6.0
5.5
5.0
4.5
4.0
3.5
3.0
2.5
2.0
1.5
1.0
0.5
0.0
f1 (ppm)
169.56
153.39
152.11
152.06
142.75
139.98
135.89
134.66
131.63
131.49
130.66
129.19
129.11
128.49
127.63
126.87
126.41
125.70
125.57
125.55
124.51
123.22
122.54
120.58
119.26
118.96
118.31
118.24
117.54
116.15
116.05
108.21
82.44
54.43
54.22
54.00
53.78
53.57
9.55
O
O
CF3
Br
O
N
5b
180
170
160
150
140
130
120
110
100
90
80
70
60
50
40
30
20
10
0
f1 (ppm)

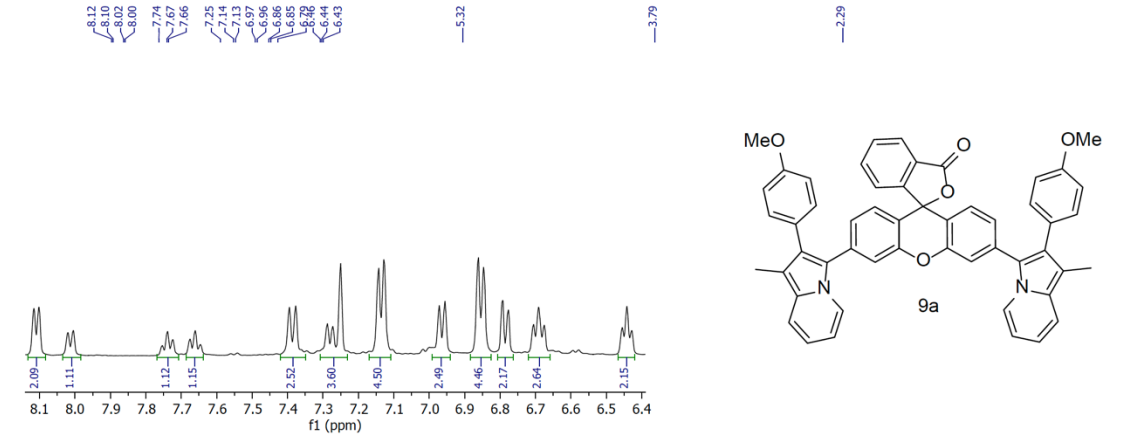
8.12
8.10
8.02
8.00
7.74
7.67
7.66
7.25
7.14
7.13
6.97
6.96
6.86
6.85
6.44
6.43
5.32
3.79
2.29
2.09
1.11
1.12
1.15
2.52
3.60
4.50
2.49
4.46
2.17
2.64
2.15
8.1 8.0 7.9 7.8 7.7 7.6 7.5 7.4 7.3 7.2 7.1 7.0 6.9 6.8 6.7 6.6 6.5 6.4
f1 (ppm)
MeO
OMe
O
O
N
N
9a

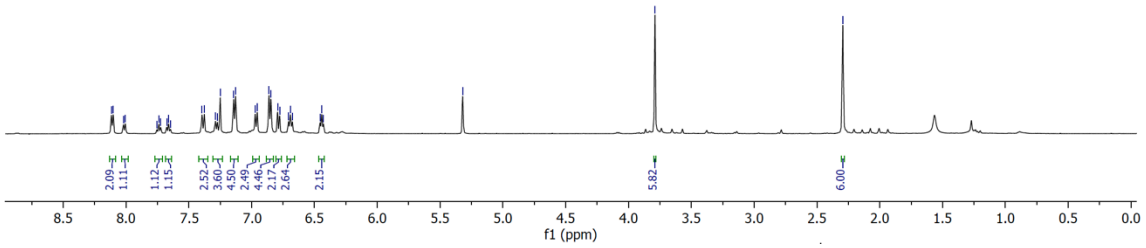
2.09
1.11
1.12
1.15
2.52
3.60
4.50
2.49
4.46
2.17
2.64
2.15
5.82
6.00
8.5 8.0 7.5 7.0 6.5 6.0 5.5 5.0 4.5 4.0 3.5 3.0 2.5 2.0 1.5 1.0 0.5 0.0
f1 (ppm)

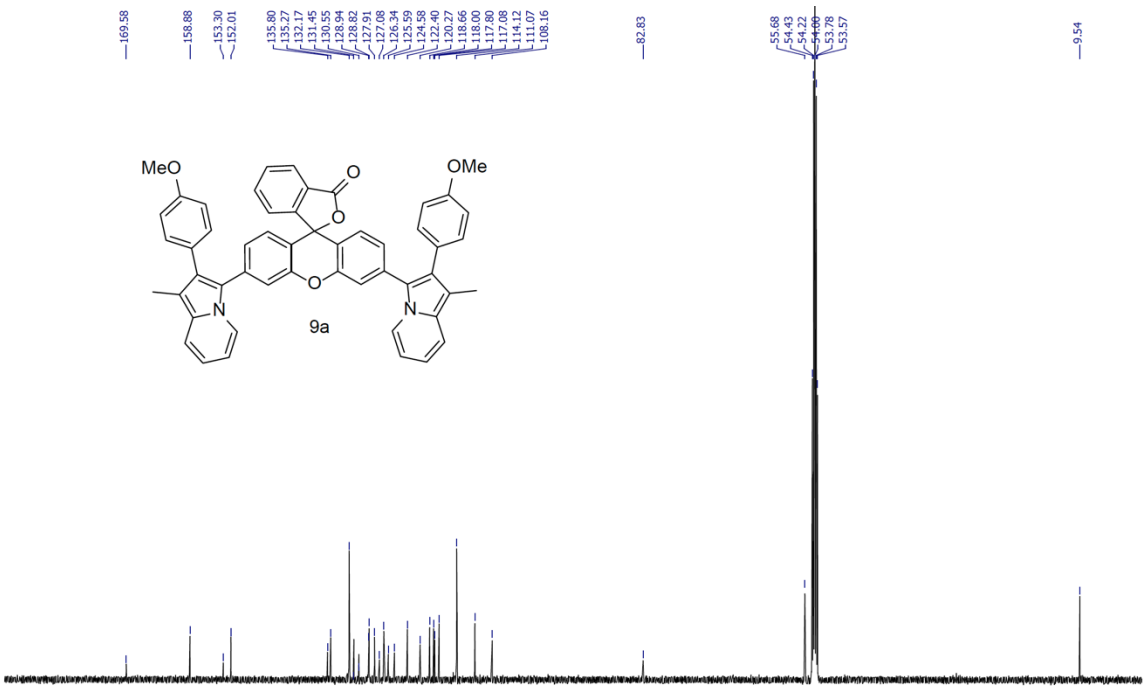
169.58
158.88
153.30
152.01
135.80
135.27
132.17
131.45
130.55
128.94
128.82
127.91
127.08
126.34
125.59
124.58
122.40
120.27
118.66
118.00
117.80
117.08
114.12
111.07
108.16
82.83
55.68
54.43
54.22
53.78
53.57
9.54
MeO
OMe
O
O
N
N
9a

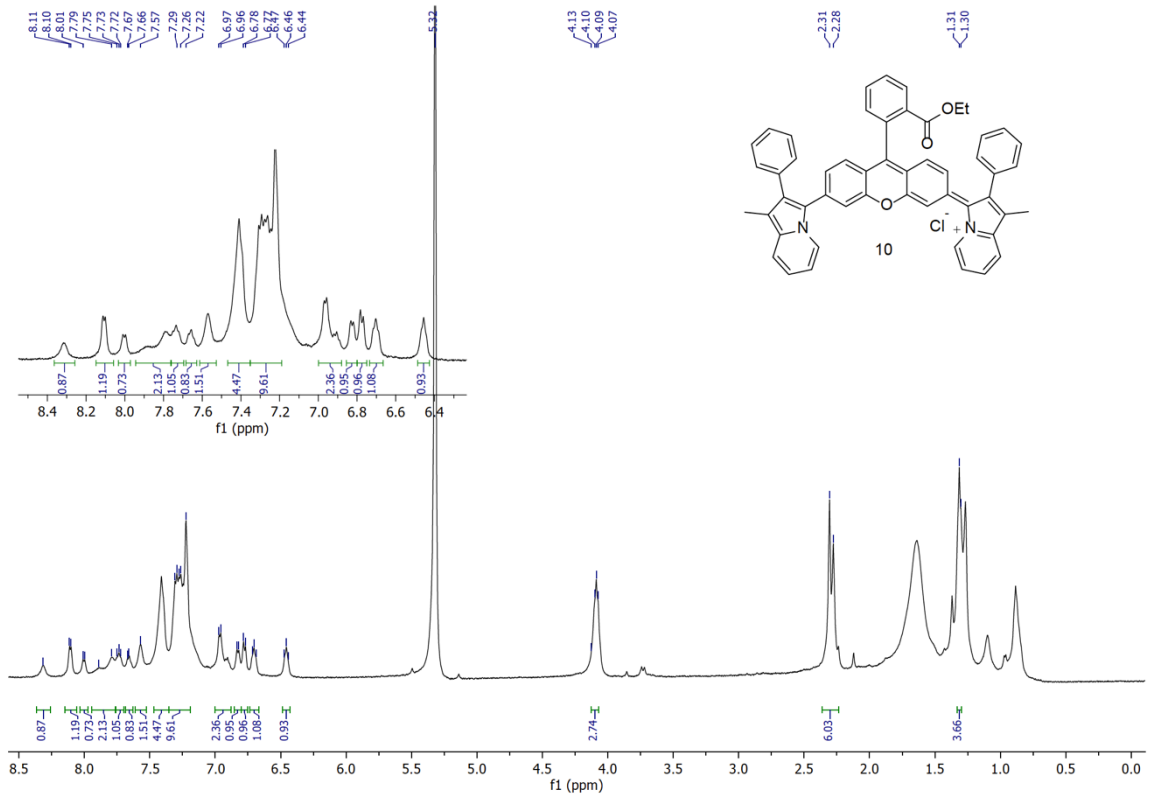
OEt
O
N
O
Cl
N
10
f1 (ppm)

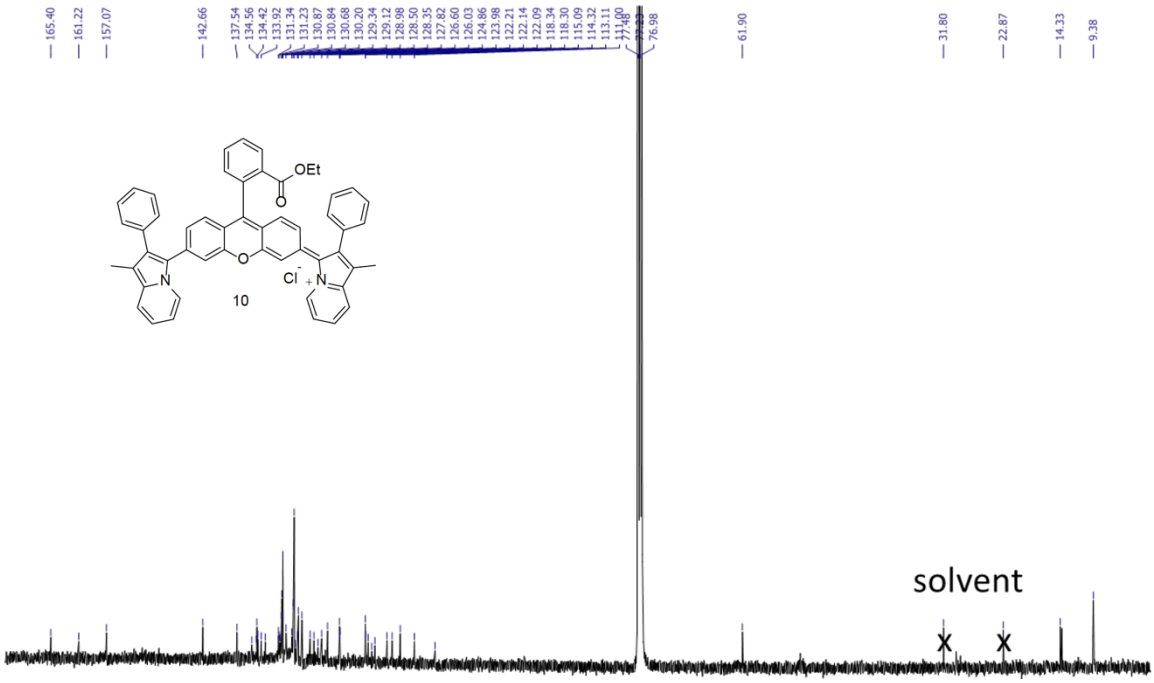
OEt
O
N
O
Cl
N
10
solvent
f1 (ppm)

Table S1. O-alkylation condition optimization.

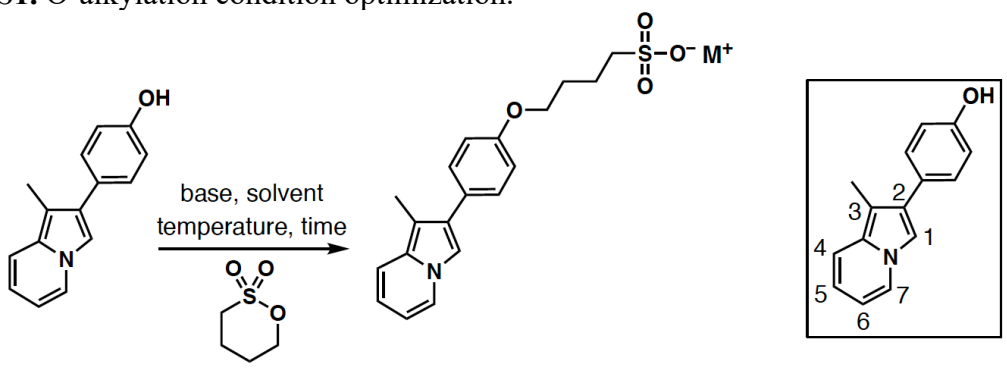

Entry	Base (equiv.)	Solvent	Temperature	Time	Result (SM:SP:P)
1	Na_2CO_3 (1.0)	isopropanol	reflux (~83 °C)	16 h	1.9:1.0:0.0
2	Na_2CO_3 (1.0)	DMF	reflux (~153 °C)	2 h	1.8:1.0:0.0
3[a]	Na_2CO_3 (2.0)	isopropanol	reflux (~83 °C)	16 h	3.2:1.0:2.9
4[b]	Cs_2CO_3 (2.5)	THF	reflux (~66 °C)	16 h	0.0:<1.0:10.0 85% product yield

SP: This product was observed by ^{1}H NMR and is consistent with C-alkyation at the C1 position as evidenced by a loss of the singlet from signal C1 with a significant shift in the signals at C7 and for the aryl ring doublet from the hydrogens closest to the indolizine (Figure S1). a 2.0 equivalents of 1,4-butanesultone was used. b 2.5 equivalents of 1,4-butanesultone was used.

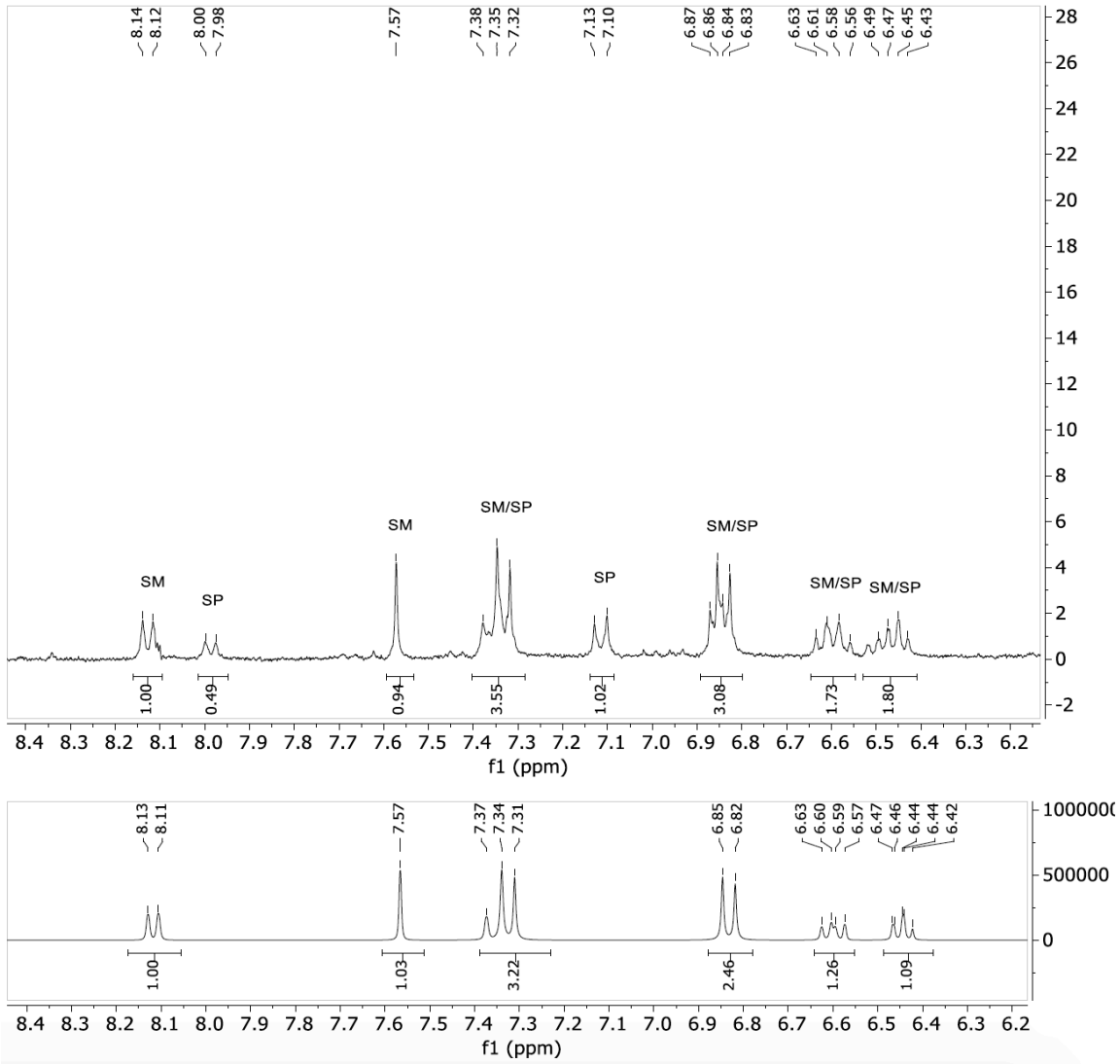

Figure S1. An example ^{1}H NMR demonstrating evidence for C1 alkylation of the phenol substituted indolizine (compound **1** in Scheme 1, see Table S1 for carbon numbering). The signal at C1 is observed for the SM at 7.57 ppm, but is not observed for the side product. The remaining proton signals from the starting material have analogues peak signals to the side product. The starting material spectrum is shown as the lower spectrum for reference. The multiplet at 7.4-7.3 ppm in the mixed sample has 3 proton signals corresponding to the starting material with 0.5 integral value remaining corresponds to 1 proton in the side product. This signal is presumably C4 rather than C1 based on C1 being a nucleophilic site on indolizine in the literature (see Cheema, H.; Baumann, A.; Loya, E. K.; Brogdon, P.; McNamara, L. E.; Carpenter, C. A.; Hammer, N. I.; Mathew, S.; Risko, C.; Delcamp, J. H. "A NIR Absorbing Indolizine-Porphyrin Push-Pull Dye for Dye-Sensitized Solar Cells" *ACS Appl. Mater. Interfaces* **2019**, 11, 16474).

Table S2. Optimization conditions for **SO_3SQ.**

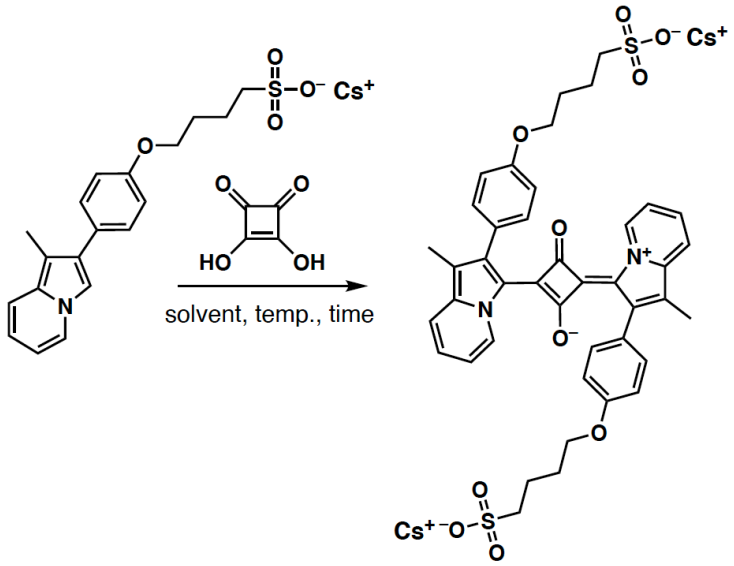

Entry	Solvent	Temperature	Condition	Time	Result
1	*n*-BuOH:Tol (1:1)	reflux (~110 °C)	N_2	6 h	SM consumed, intractable brown precipitate formation
2	*n*-BuOH:Tol (1:1)	reflux (~110 °C)	O_2	6 h	SM consumed, intractable brown precipitate formation
3	*n*-BuOH:Tol (1:1)	pressure flask 130 °C	N_2	6 h	SM consumed, intractable brown precipitate formation
4	*n*-BuOH:Tol (1:1)	reflux (~110 °C)	N_2, 2-3 drops H_2O	6 h	trace product formation, SM consumed, intractable brown precipitate formation
5	*n*-BuOH:Tol:water (1:1:1)	slow heating to 100 °C	N_2	6 h	trace product formation, SM consumed, intractable brown precipitate formation
6	*n*-BuOH:Tol:water (6:6:1)	reflux (~110 °C)	N_2	2 h	trace product formation, SM consumed, intractable brown precipitate formation
7	*n*-BuOH:Tol:water (120:120:1)	reflux (~110 °C)	N_2	2 h	SM consumed, intractable brown precipitate formation, 8% product yield
8	MeOH	pressure flask (100 °C)	N_2	6 h	SM consumed, 60% yield

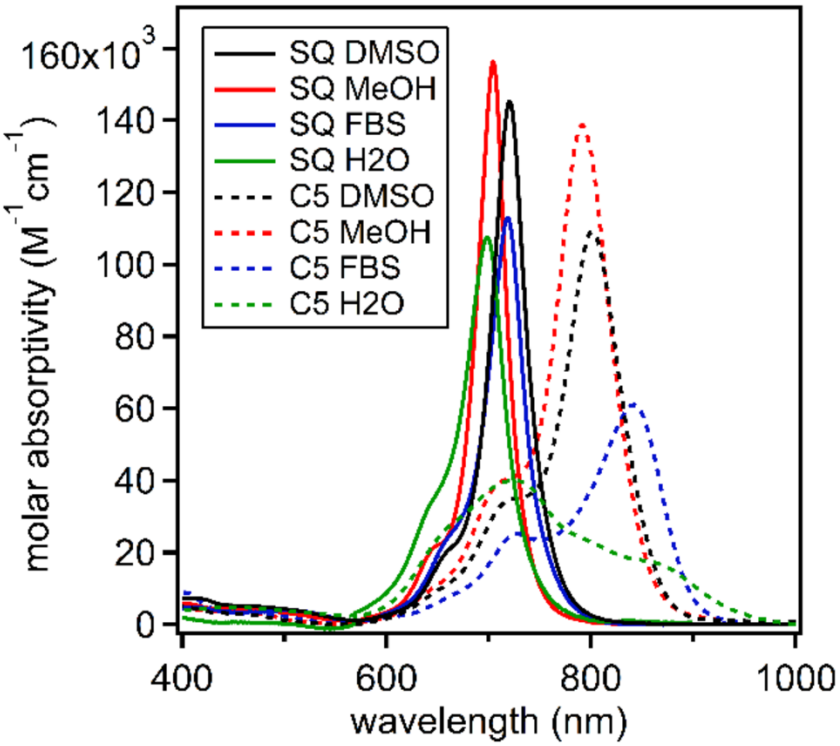

Figure S2. Vis-NIR region molar absorptivity of **SO_3SQ** and **SO_3C5** in DMSO, MeOH, H2O, and FBS.

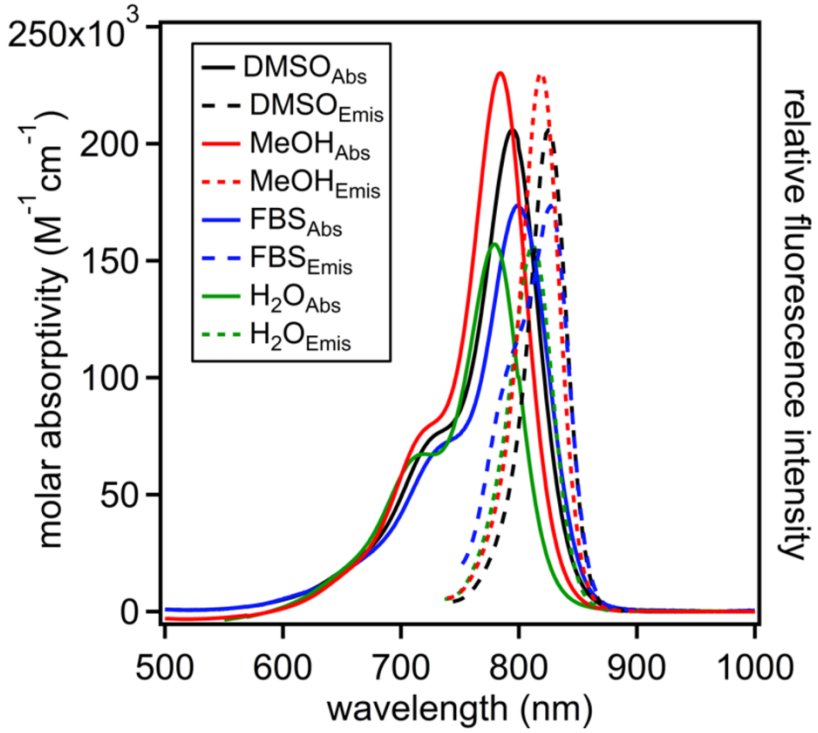

Figure S3. Vis-NIR region molar absorptivity and normalized fluorescence of **ICG** in DMSO, MeOH, H2O, and FBS

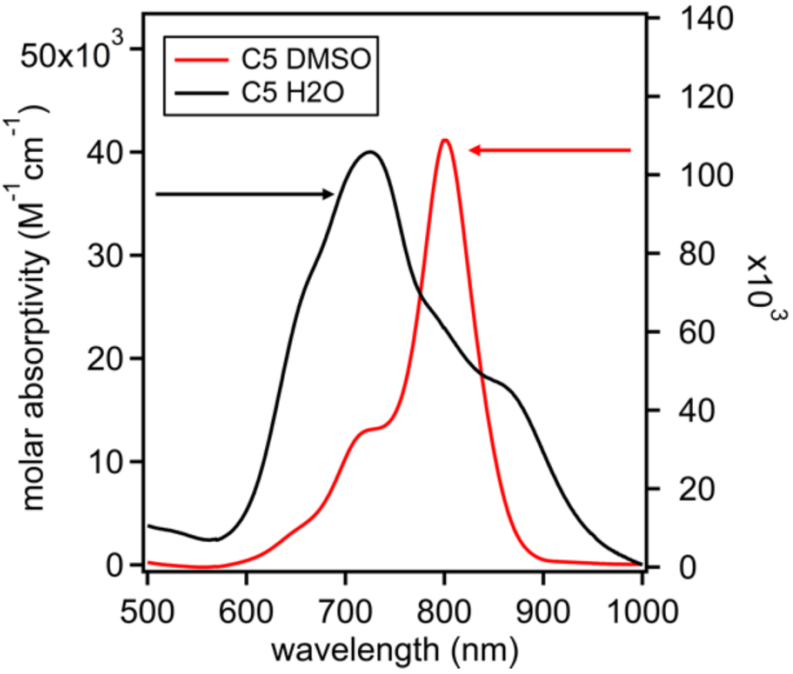

Figure S4. Vis-NIR region molar absorptivity graph of **SO_3C5** in water and DMSO demonstrating the significant aggregate absorption of **SO_3C5** in water. Two different y-axis scales are used due to large differences in molar absorptivities with the two solvents.

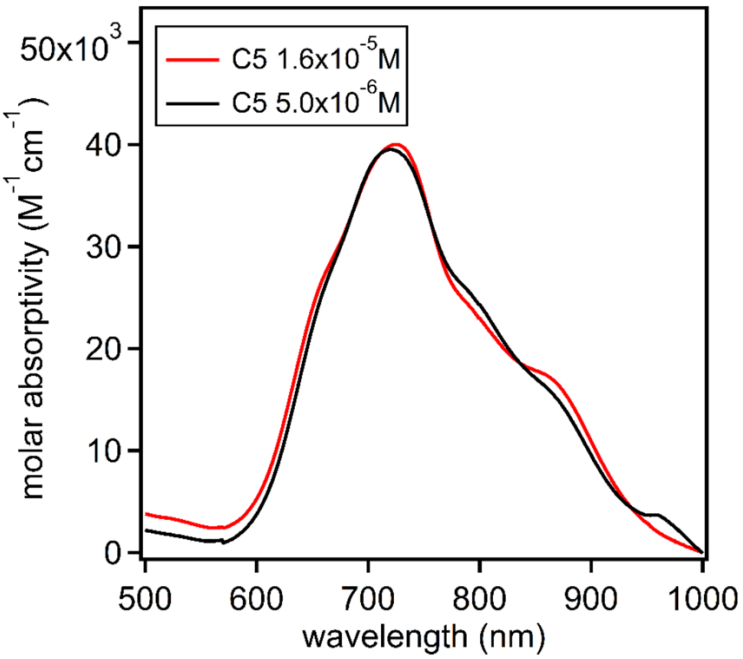

Figure S5. Vis-NIR region molar absorptivity graph of **SO_3C5** in water demonstrating no noticeable concentration dependent aggregation over a ~1 order of magnitude change in concentration.

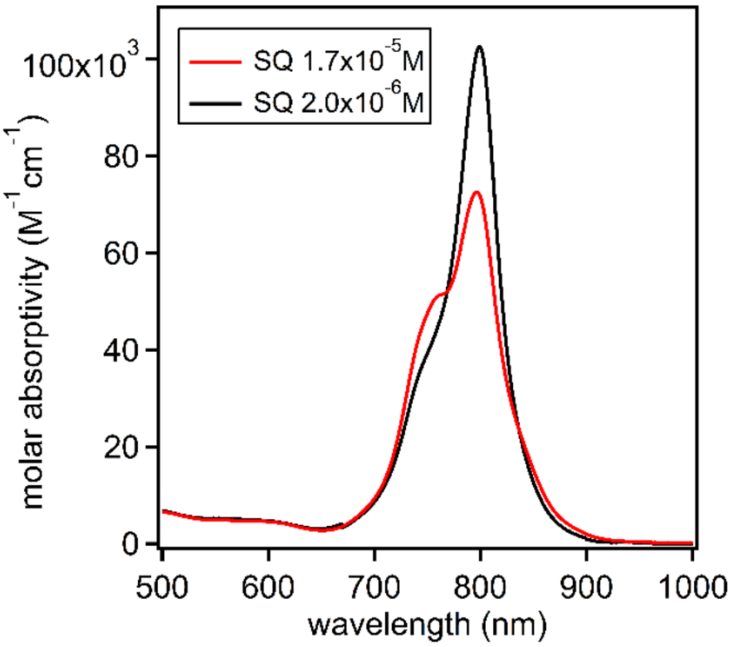

Figure S6. Vis-NIR region molar absorptivity graph of **SO_3SQ** in water demonstrating modest concentration dependent aggregation over a 1 order of magnitude change in concentration.

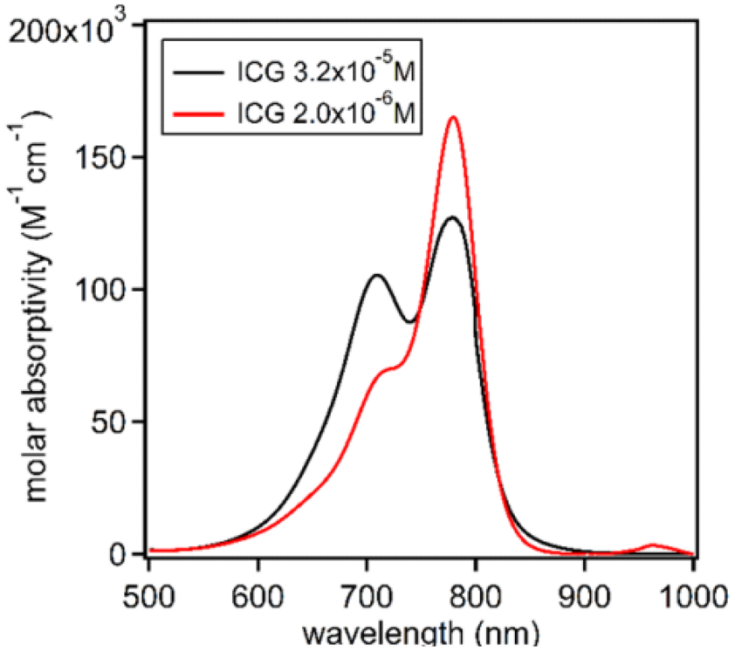

Figure S7. Vis-NIR region molar absorptivity graph of **ICG** in water demonstrating apparent concentration dependent aggregation in over a 1 order of magnitude change in concentration.

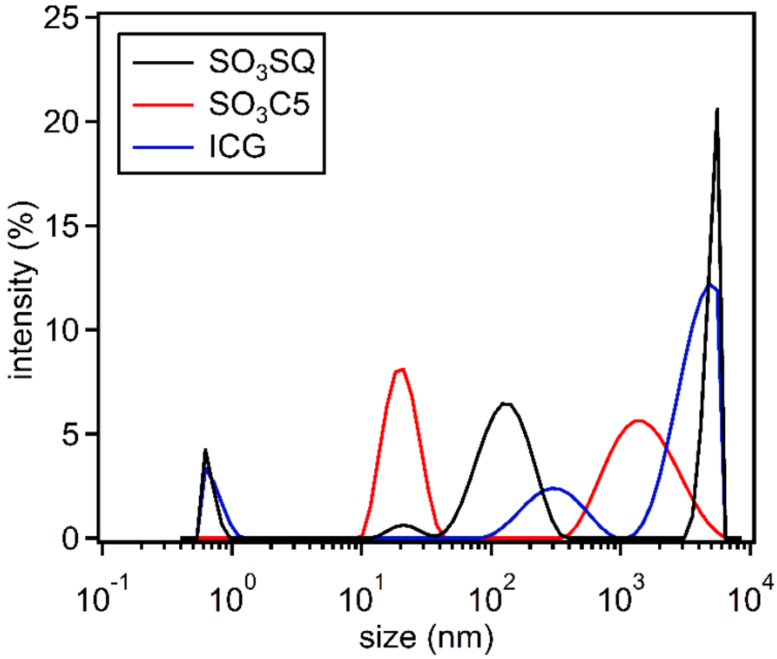

Figure S8. DLS data demonstrating aggregate size distributions for **SO_3SQ**, **SO_3C5**, and **ICG** in water at 5 x 10^{-6} M. DLS studies were also done for all three dyes in DMSO and demonstrated no aggregate formation.

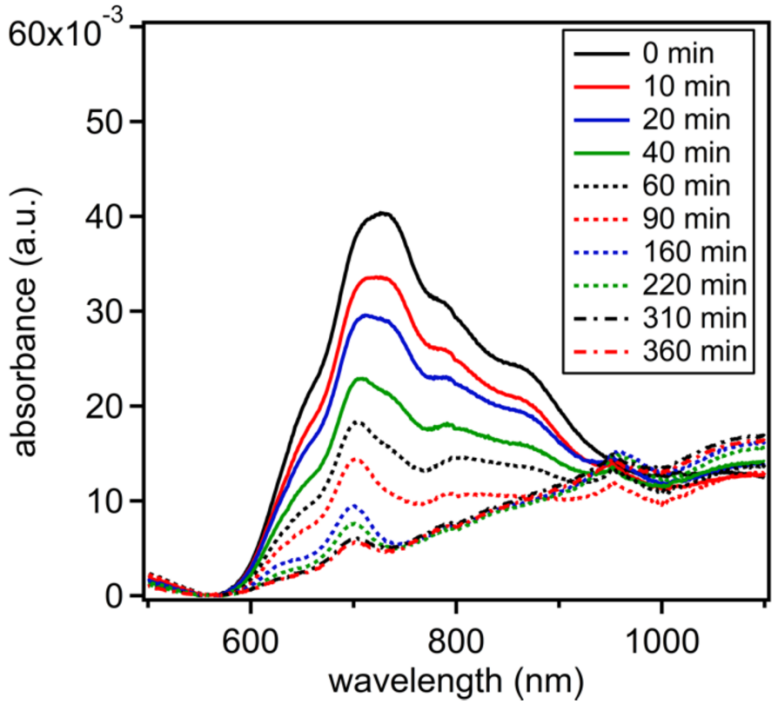

Figure S9. Photostability study with **SO_3C5** in water with continuous white light LED irradiation.

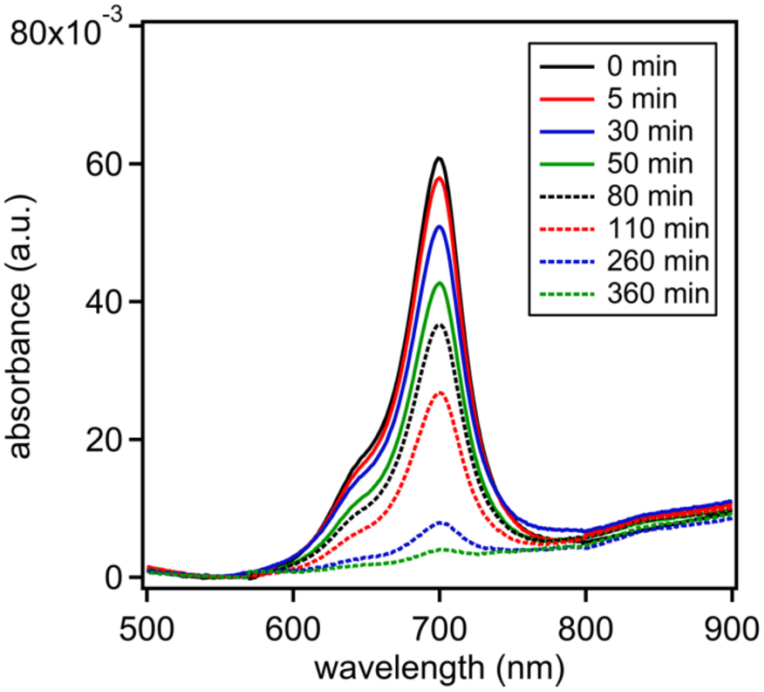

Figure S10. Photostability study with **SO_3SQ** in water with continuous white light LED irradiation.

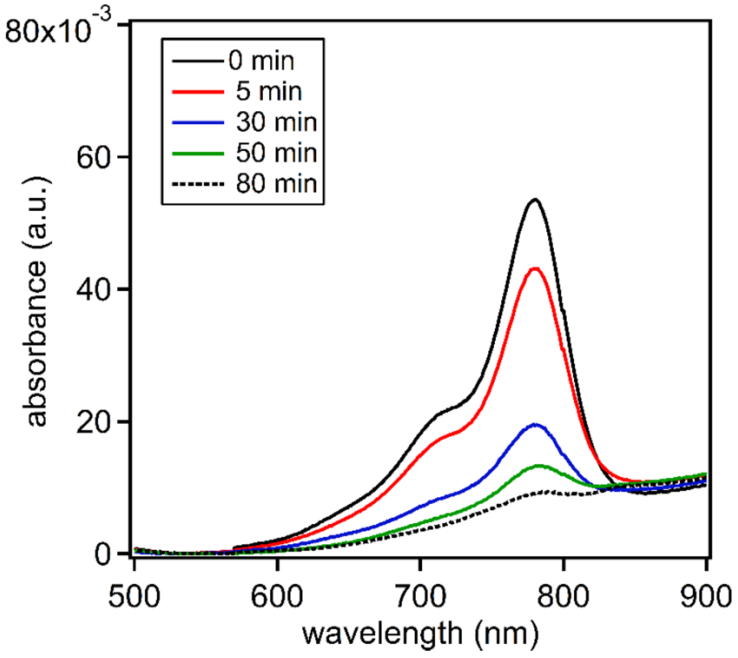

Figure S11. Photostability study with **ICG** in water with continuous white light LED irradiation.

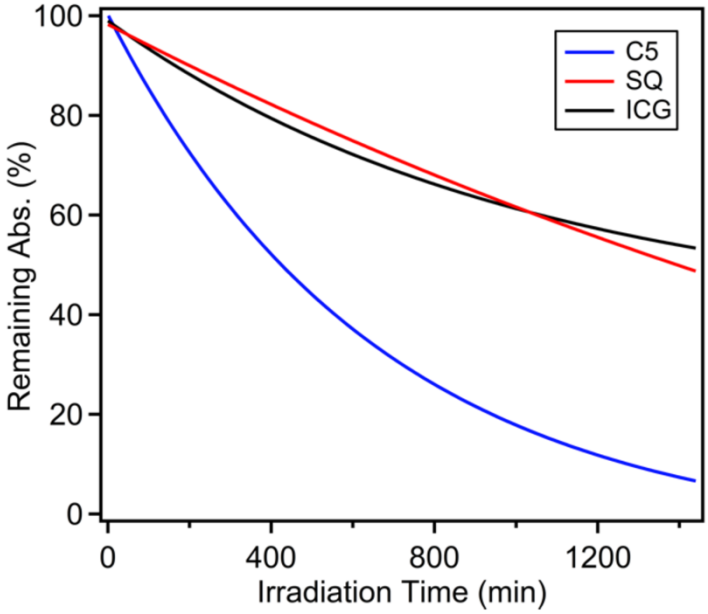

Figure S12. Photostability comparison of **SO_3C5**, **SO_3SQ**, and **ICG** in MeOH with continuous white light LED irradiation.

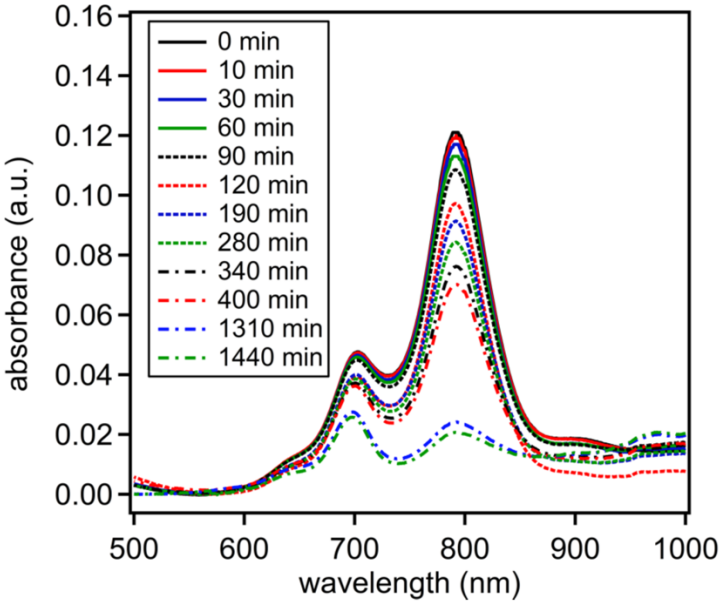

Figure S13. Photostability study with **SO_3C5** in MeOH with continuous white light LED irradiation.

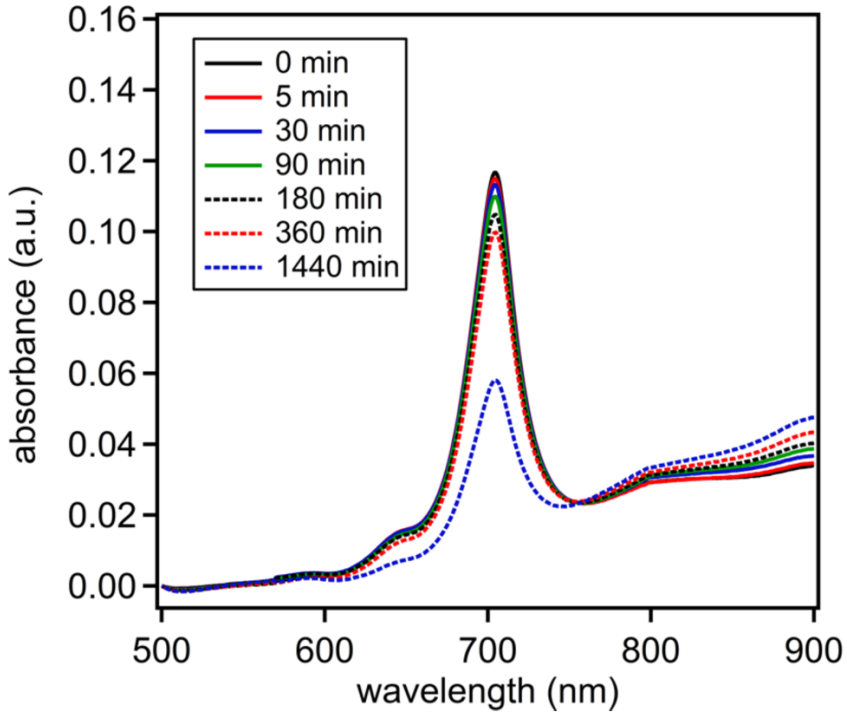

Figure S14. Photostability study with **SO_3SQ** in MeOH with continuous white light LED irradiation.

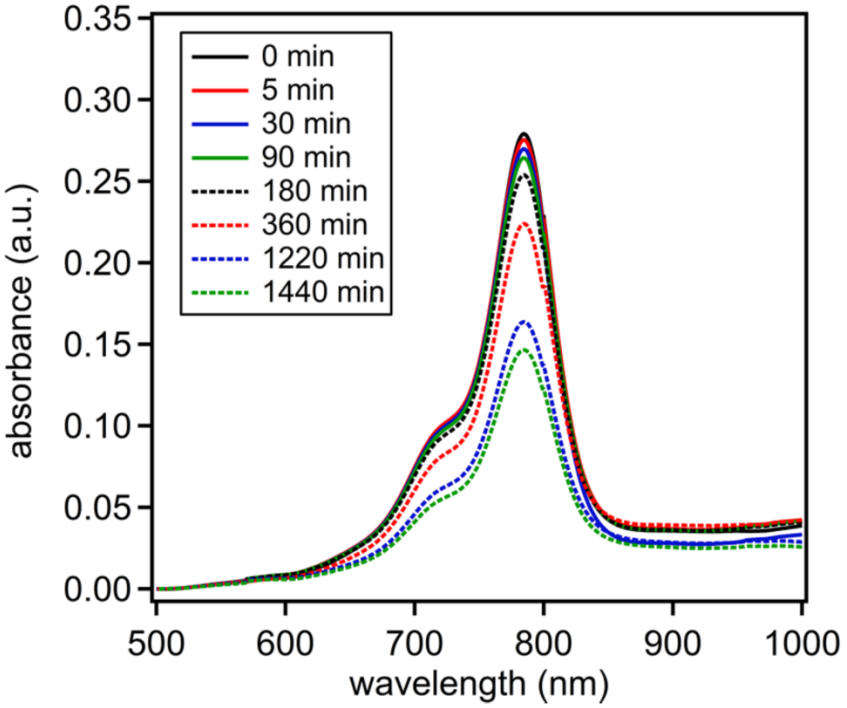

Figure S15. Photostability study of **ICG** in MeOH with continuous white light LED irradiation.

Table S3. Solubility of each dye in water, MeOH, and DMSO in mg/mL.

Dye	Water	MeOH	DMSO
SO_3C5	11.0	7.0	21.0
SO_3SQ	11.0	5.8	29.0
ICG	7.8	10.0	18.0

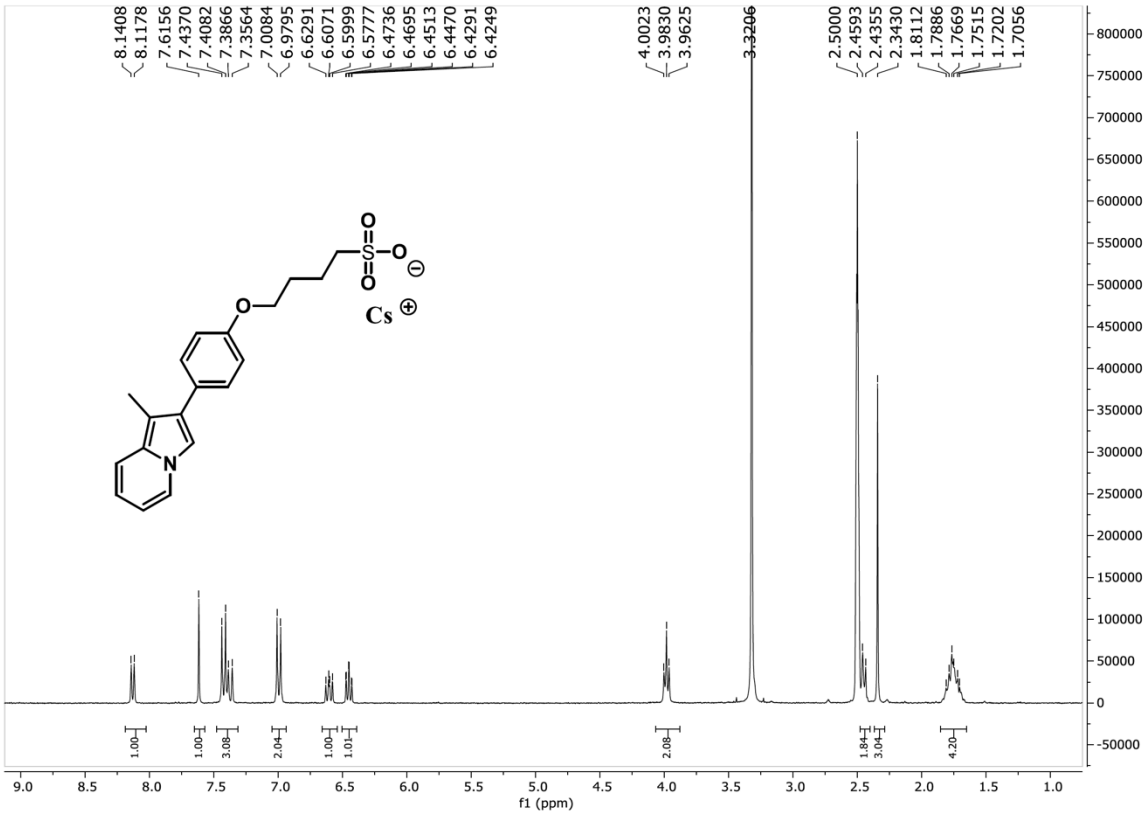

Figure S16. ^{1}H NMR (300 MHz, DMSO-d6) of **SO_3Indz**.

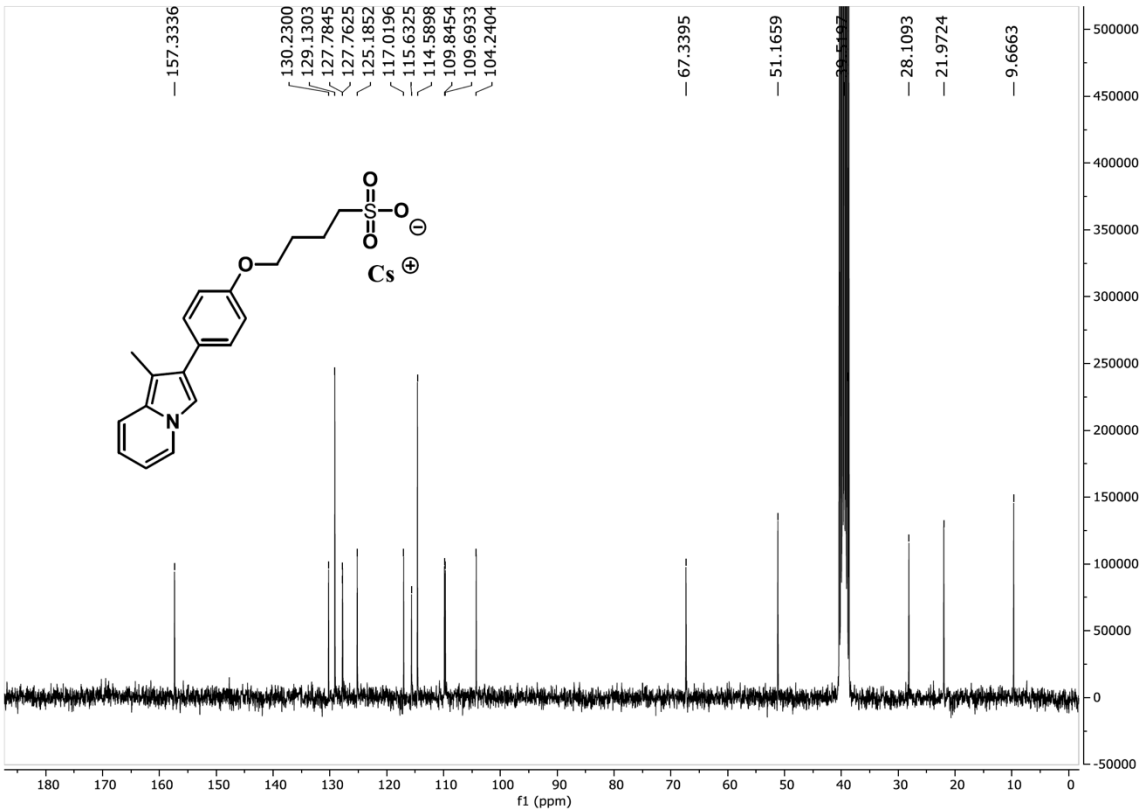

Figure S17. ^{13}C {^{1}H} NMR (300 MHz, DMSO-d6) of **SO_3Indz**.

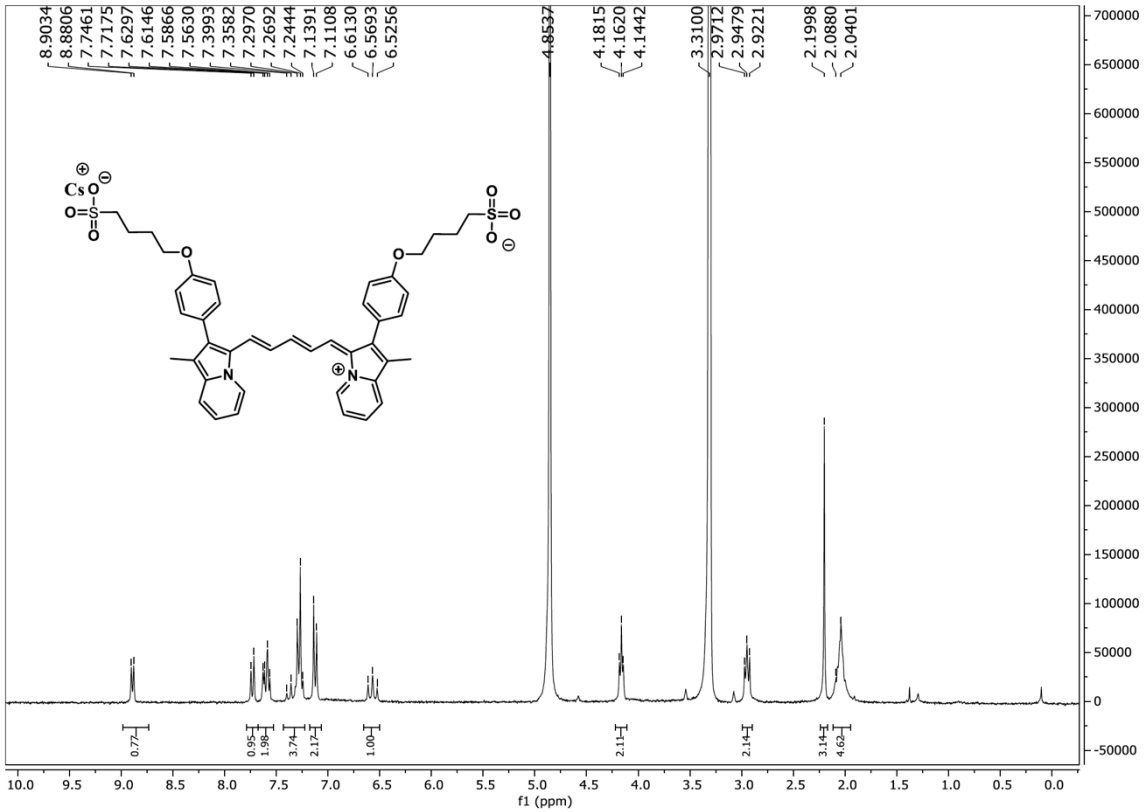

Figure S18. ^{1}H NMR (300 MHz, CD_3OD-d4) of **SO_3C5**.

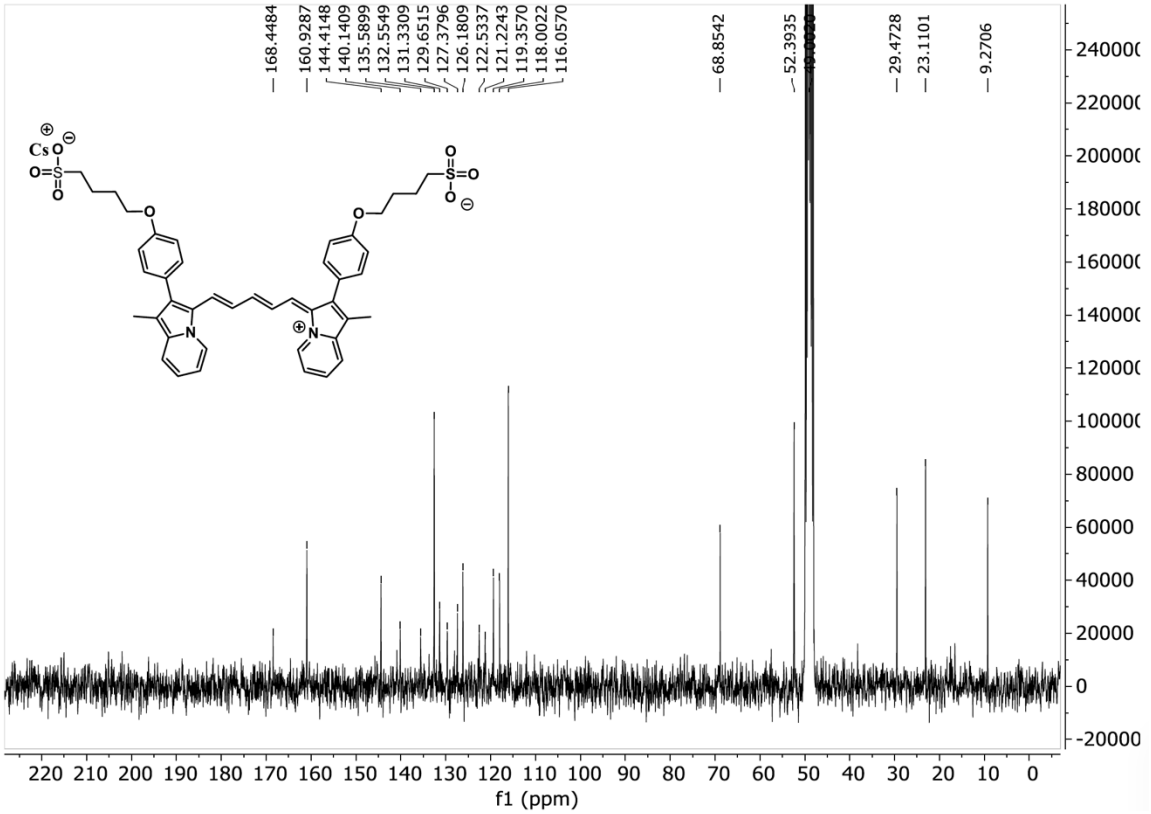

Figure S19. ^{13}C {^{1}H} NMR (300 MHz, CD_3OD-d4) of **SO_3C5**. We note that while the signal-to noise ratio is non-optimal, this spectrum was obtained after 12 hours of continuous acquisition time and the poor signal-to-noise ratio is due to a limited solubility.

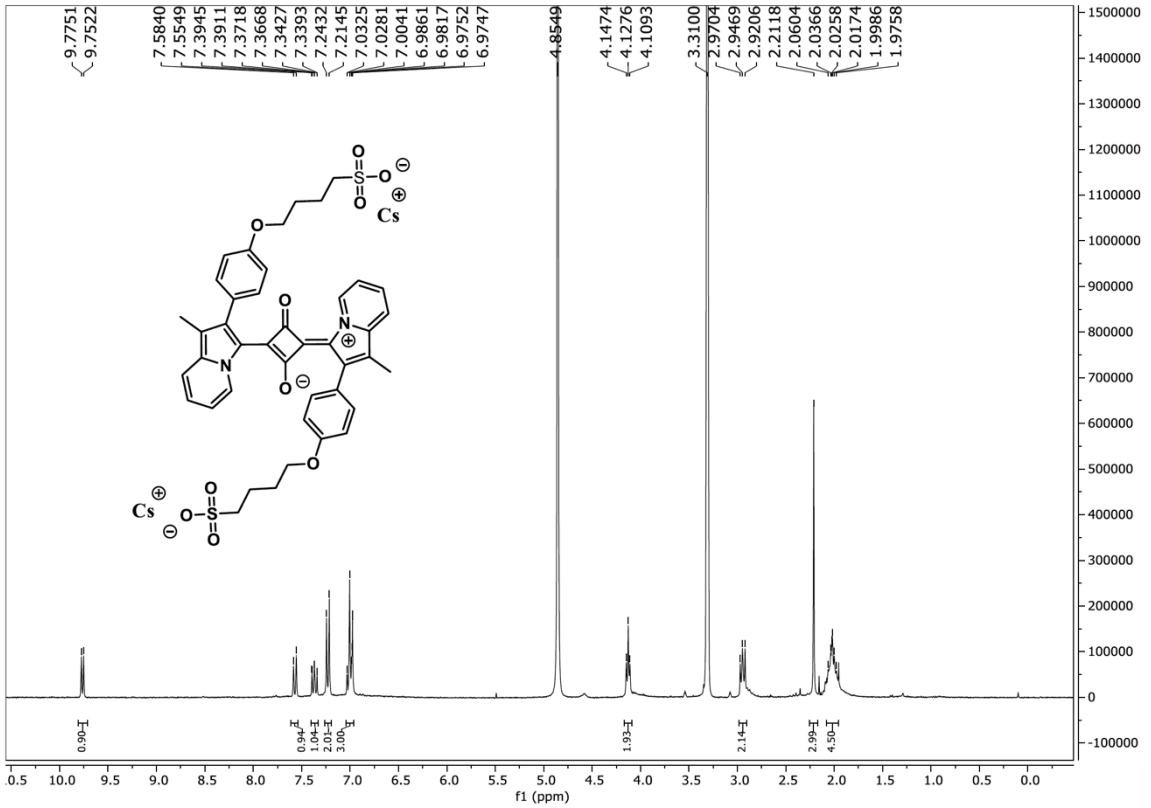

Figure S20. ^{1}H NMR (300 MHz, CD_3OD-d4) of **SO_3SQ**.

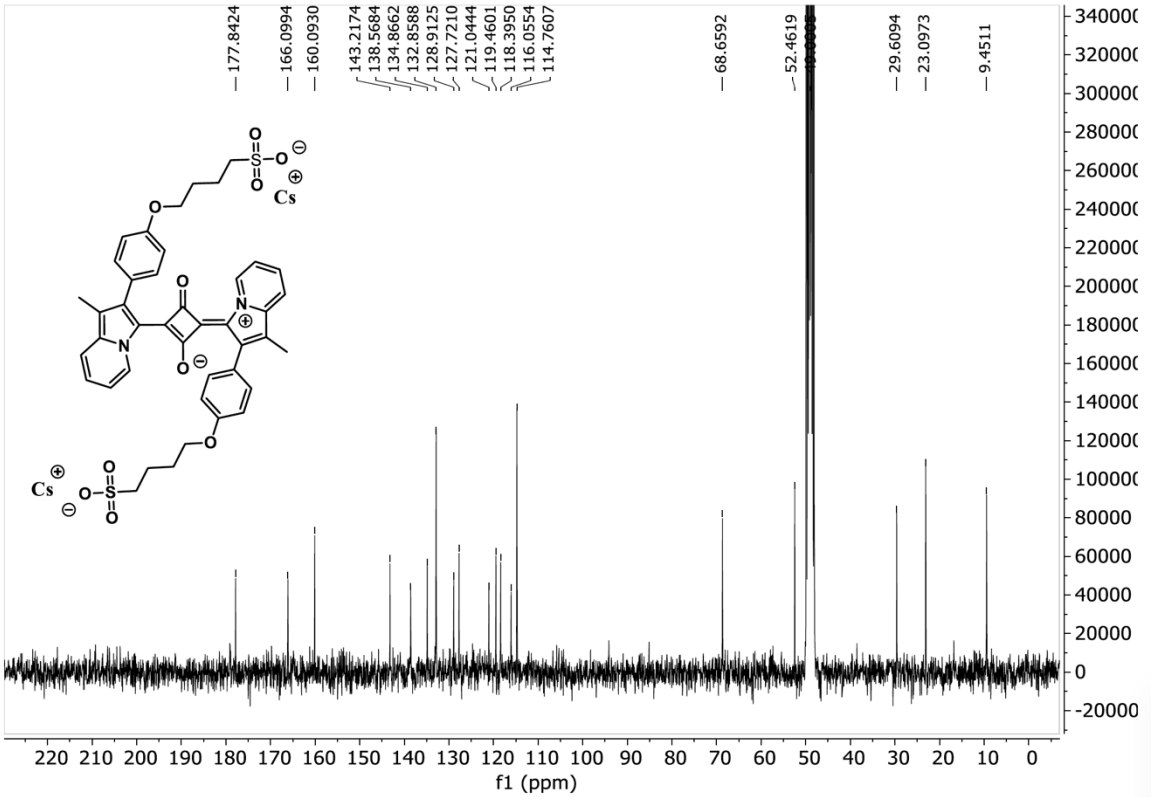

Figure S21. ^{13}C {^{1}H} NMR (300 MHz, CD_3OD-d4) of **SO_3SQ**.

APPENDIX D. JOURNAL PERMISSIONS

Journal permission for Chapter II.

12/18/2020 Rightslink® by Copyright Clearance Center

Copyright Clearance Center RightsLink®

Home | Help | Email Support | Sign in | Create Account

ACS Publications
Most Trusted. Most Cited. Most Read.

Indolizine-Cyanine Dyes: Near Infrared Emissive Cyanine Dyes with Increased Stokes Shifts

Author: Jacqueline Gayton, Shane A. Autry, William Meador, et al
Publication: The Journal of Organic Chemistry
Publisher: American Chemical Society
Date: Jan 1, 2019

Copyright © 2019, American Chemical Society

PERMISSION/LICENSE IS GRANTED FOR YOUR ORDER AT NO CHARGE

This type of permission/license, instead of the standard Terms & Conditions, is sent to you because no fee is being charged for your order. Please note the following:

- Permission is granted for your request in both print and electronic formats, and translations.
- If figures and/or tables were requested, they may be adapted or used in part.
- Please print this page for your records and send a copy of it to your publisher/graduate school.
- Appropriate credit for the requested material should be given as follows: "Reprinted (adapted) with permission from (COMPLETE REFERENCE CITATION). Copyright (YEAR) American Chemical Society." Insert appropriate information in place of the capitalized words.
- One-time permission is granted only for the use specified in your request. No additional uses are granted (such as derivative works or other editions). For any other uses, please submit a new request.

BACK CLOSE WINDOW

© 2020 Copyright - All Rights Reserved | Copyright Clearance Center, Inc. | Privacy statement | Terms and Conditions
Comments? We would like to hear from you. E-mail us at customercare@copyright.com

Journal permission for Chapter III.

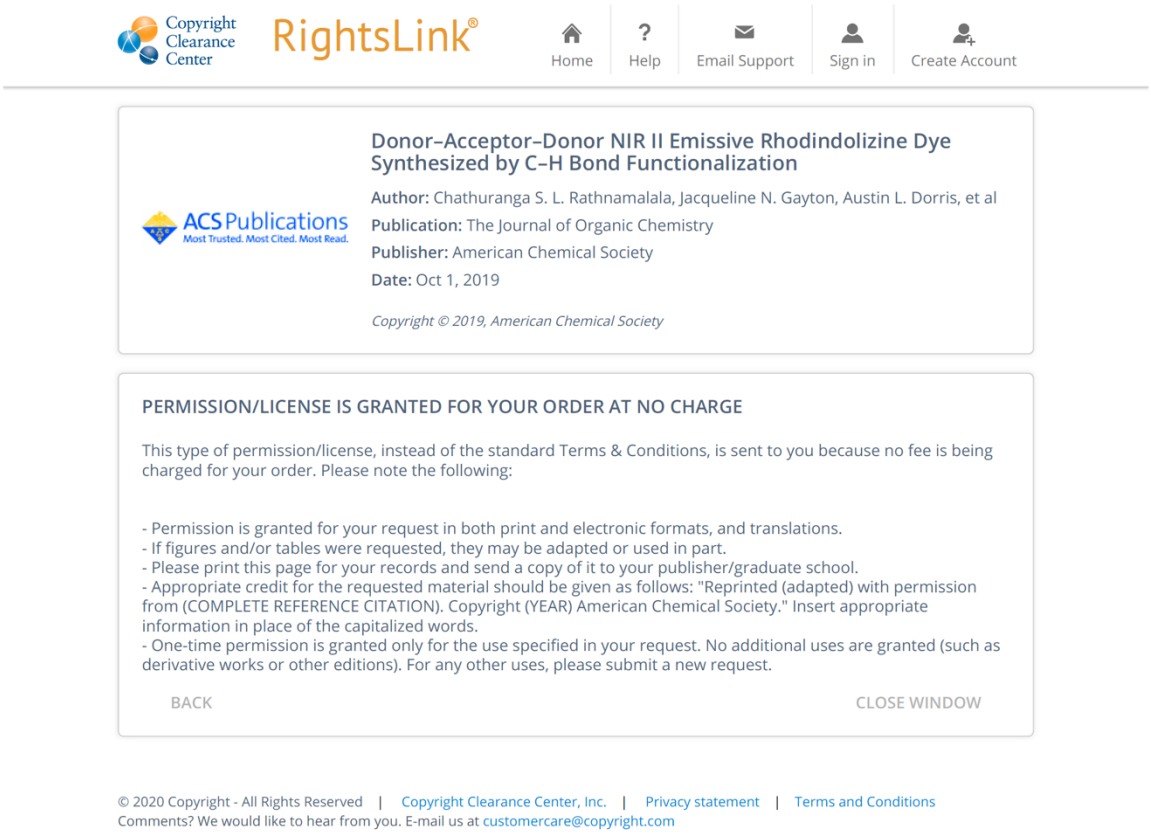

Copyright Clearance Center RightsLink®

Home | Help | Email Support | Sign in | Create Account

ACS Publications
Most Trusted. Most Cited. Most Read.

Donor–Acceptor–Donor NIR II Emissive Rhodindolizine Dye Synthesized by C–H Bond Functionalization

Author: Chathuranga S. L. Rathnamalala, Jacqueline N. Gayton, Austin L. Dorris, et al
Publication: The Journal of Organic Chemistry
Publisher: American Chemical Society
Date: Oct 1, 2019

Copyright © 2019, American Chemical Society

PERMISSION/LICENSE IS GRANTED FOR YOUR ORDER AT NO CHARGE

This type of permission/license, instead of the standard Terms & Conditions, is sent to you because no fee is being charged for your order. Please note the following:

- Permission is granted for your request in both print and electronic formats, and translations.
- If figures and/or tables were requested, they may be adapted or used in part.
- Please print this page for your records and send a copy of it to your publisher/graduate school.
- Appropriate credit for the requested material should be given as follows: "Reprinted (adapted) with permission from (COMPLETE REFERENCE CITATION). Copyright (YEAR) American Chemical Society." Insert appropriate information in place of the capitalized words.
- One-time permission is granted only for the use specified in your request. No additional uses are granted (such as derivative works or other editions). For any other uses, please submit a new request.

BACK CLOSE WINDOW

Journal permission for Chapter IV.